Montanuniversität Leoben

Characterization of the precipitation mechanism in the molybdenum based alloy MHC

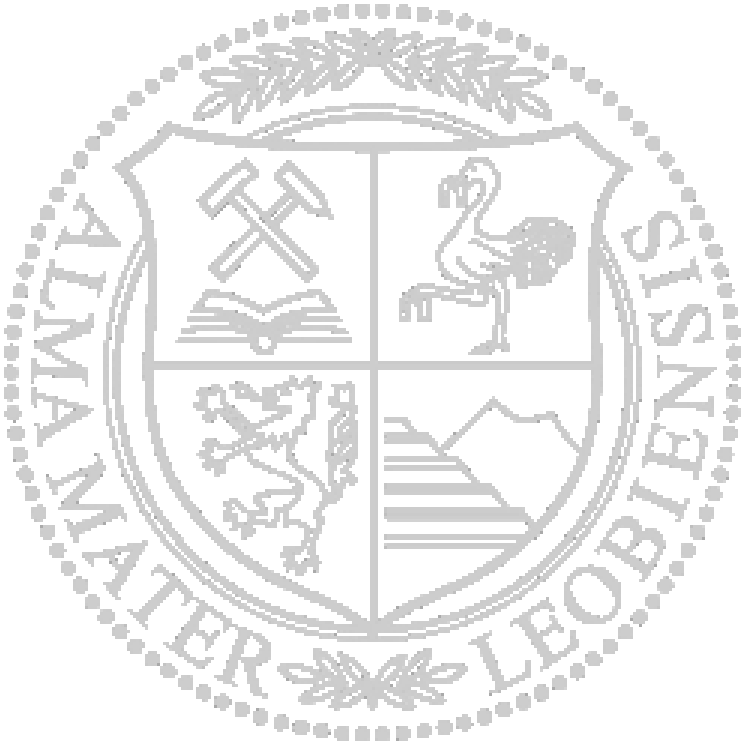

Master Thesis

by

David Lang

This work has been carried out in cooperation with Plansee SE and the Department of Physical Metallurgy and Materials Testing, University of Leoben.

Leoben, November 2012

Affidavit

I declare in lieu of oath that I wrote this thesis and performed the associated research myself, using only literature cited in this volume.

Leoben, November 2012 David Lang

Acknowledgements

First of all I want to thank Dipl. Ing. Dr. Harald Leitner for giving me the opportunity to perform this thesis at the department for Physical Metallurgy and Materials Testing as a member of the Christian Doppler Laboratory “Early Stages of Precipitation” and for giving me useful advice. Next I want to express my gratefully thanks to PhD student Dipl. Ing. Christopher Pöhl who did a major part in guiding me through this work. Thank you for all the fruitful discussions and for the productive working environment we created.

My sincerest gratitude belongs to the project team from Plansee SE, especially to Dipl. Ing. Dr. Wolfram Knabl who made this work possible and to Dipl. Ing. Dr. Jürgen Schatte who supported me with tons of information, numerous samples and his valuable advice.

Special thanks belong to Professor Roland Stickler for proofreading this thesis. Additionally I want to thank all the other members of our “Molytaskforceteam” for interesting discussions and evening activities during our workshops.

Next I want to thank all the employees from the Department of Industrial Development from Plansee SE as well as from the Department of Physical Metallurgy and Materials Testing who were involved in any kind in this work.

Most of all I want to thank my whole family, primarily my mother and father who always encouraged me and of course my brother, who reminded me nearly every day in an annoying way to hurry up and finish university. See, I finally did it! Particularly I want to thank my beloved grandma for cheering me up with the best Apple Strudel in the world when times in my studies were rough. Finally she made me her apprentice and gave me the secret recipe.

I am also thankful to have great friends with whom I shared uncountable evening and various outdoor activities during my studies, so I was able to clear my mind and to go on with new strength.

Looking back at this thesis and the past years in Leoben I can easily say that this time was a great enrichment for me. I am looking forward for the next challenges to come, involving again such great people in my life!

Thank you all!

Contents

Abbreviations and Symbols V
Abstract IX
Zusammenfassung X

1 INTRODUCTION 1

2 THEORETICAL BACKGROUND 3

2.1 Strengthening of metals 3
2.1.1 Dispersion hardening 4
2.1.2 Precipitation hardening 4
2.2 Nucleation of precipitates 6
2.3 Development of precipitates 9
2.3.1 Interfacial energy effects 9
2.3.1.1 Fully coherent precipitates 9
2.3.1.2 Partially coherent precipitates 10
2.3.1.3 Incoherent precipitates 10
2.3.1.4 Precipitates on grain boundaries 10
2.3.2 Misfit strain effects 11
2.3.2.1 Fully coherent precipitates 11
2.3.2.2 Incoherent precipitates 12
2.3.3 Precipitate growth 13
2.3.3.1 Diffusion controlled lengthening of plates and needles 13
2.3.3.2 Thickening of plate-like precipitates 14
2.4 Transformation kinetics 15
2.5 Particle coarsening 16
2.6 Diffusion– high diffusivity paths 18
2.6.1 Diffusion along grain boundaries and free surfaces 18
2.6.2 Diffusion along dislocations 18
2.7 State of the art of the precipitation behavior of Mo- Hf- C alloys 20

3 EXPERIMENTAL PROCEDURES 26

3.1 Dilatometry 26
3.2 Optical light microscopy (OLM) 28
3.3 Micro hardness testing 29
3.4 Scanning electron microscopy (SEM) 29
3.5 Transmission electron microscopy (TEM) 30

3.6 Atom probe tomography (APT) 31
3.7 X-Ray diffraction (XRD) 36
3.8 Chemical analysis 36
4 THERMO-MECHANICAL PROCESS AND SAMPLING PLAN 37
4.1 Thermo-mechanically processing of MHC samples 37
4.2 Sampling plan 38
5 RESULTS 39
5.1 Characterization of the as-sintered condition (SC) 39
5.1.1 TEM investigation of the SC 41
5.1.2 Atom probe tomography of the SC 42
5.2 Microstructure after deformation- condition f' (Cf') 44
5.2.1 TEM investigations of Cf' 44
5.2.2 Atom probe tomography of Cf' 46
5.3 Microstructure after deformation and heat treatment 49
5.3.1 SEM investigation of Cg' 49
5.3.2 TEM investigations 50
5.3.2.1 Condition g' (Cg') 50
5.3.2.2 Condition h' (Ch') 52
5.3.2.3 Condition j (Cj) 58
5.3.1 Geometry and size distribution of secondary precipitates in Ch' and Cj 62
5.3.2 Atom probe tomography 66
5.3.2.1 Condition g' (Cg') 66
5.3.2.2 Condition j (Cj) 69
5.4 Microstructure after heat treatment without deformation 70
5.4.1 OLM microstructure of SC10h1600C 70
5.4.2 TEM investigations of the SCj and SC10h1600C 71
5.4.3 Atom probe tomography 73
5.4.3.1 Sintered condition j (SCj) 73
5.4.3.2 Sintered condition tempered 10h at 1600°C (SC10h1600C) 74
5.5 X-ray diffraction (XRD) patterns of all investigated conditions 75
5.6 Microhardness testing HV0.1 77
6 DISCUSSION 78
7 CONCLUSIONS AND OUTLOOK 84
List of Figures XI
List of Tables XV
References XVI

Abbreviations and Symbols

1D	One-dimensional
2D	Two-dimensional
3D	Three-dimensional
α	Matrix
β	Precipitate
$\gamma_{\alpha\alpha}$	Interfacial energy of a grain boundary [mJ/m²]
$\gamma_{\alpha\beta}$	Interfacial energy between the matrix α and a precipitate β [mJ/m²]
γ_c	Interfacial energy for a coherent interface [mJ/m²]
γ_i	Interfacial energy for an incoherent interface [mJ/m²]
γ_{st}	Structural interfacial energy [mJ/m²]
Δ	Volume misfit [%]
δ	Grain boundary thickness [nm] or unconstrained misfit [%]
$\Delta\sigma$	Yield strength difference [MPa]
ΔG	Difference in total free energy of matrix and precipitate [J]
ΔG_d	Defect free energy [J]
ΔG_{het}	Free energy for heterogeneous nucleation [J]
ΔG^*_{het}	Critical free energy for heterogeneous nucleation [J]
ΔG^*_{hom}	Critical free energy for homogeneous nucleation [J]
ΔG_S	Misfit strain energy reduction [J]
ΔG_V	Volume free energy reduction [J]
ΔV	Volume difference [nm³]
θ	Interfacial angle between particle and matrix [°]
ϑ	Lengthening or thickening rate of particle [nm/h]
λ	Ledge spacing [nm]
μ	Statistical value which indicates clustering [-]
φ	Logarithmic deformation degree $\varphi=\ln(h_x/h_0)$ [-]
$\dot{\varphi}$	Deformation rate [s^{-1}]
χ^2	Chi-square test, statistical function
ω	Numerical factor including vibration frequency of atoms [-]
A	Area [m²]
a	Length of a plate-like precipitate [nm] or lattice parameter [Å]
a_α	Lattice parameter of the matrix [Å]
a_β	Lattice parameter of a precipitate [Å]
APT	Atom probe tomography

b	Burgers vector [Å] or width of a plate-like precipitate [nm]
bcc	Body centered cubic
c	Thickness of a plate-like precipitate [nm]
C1	Concentration of heterogeneous nucleation sites per unit volume [n/m³]
CA	Combustion analysis
CGHE	Carrier gas hot extraction
D	Diffusion coefficient [cm²/s]
d	Grain size [µm]
D1	Diffusion coefficient of the defect free lattice [cm²/s]
D_{app}	Apparent diffusion coefficient regarding high diffusivity paths [cm²/s]
DBFIB	Dual beam focused ion beam
D_p	Diffusion coefficient for pipe diffusion [cm²/s]
d_s	Fixed distance for connecting solute atoms [nm]
$D_{s,b}$	Diffusion coefficient for a grain boundary or the surface [cm²/s]
$D_{s,b0}$	Frequency factor [cm²/s]
EBSD	Electron backscatter diffraction
EDS	Energy dispersive spectroscopy
e(n)	Number of blocks containing n solute atoms measured experimentally [-]
ESOP	Early stages of precipitation
F	Force [N]
f	Volume fraction [%]
f(c/a)	Function for the particle shape [-]
fcc	Face centered cubic
FEG	Field emission gun
FFT	Fast Fourier transformation
FIB	Focused ion beam
f(n)	Binomial distribution of number n of solute atoms
G	Shear modulus [GPa]
g	Cross sectional area of pipes per unit volume area of matrix [N/m³]
G*	Heterogeneous or homogeneous critical free energy for nucleation [J]
h	Height of a ledge [nm]
HRTEM	High resolution transmission electron microscope
HV	Vickers hardness
h_x	Sample height after deformation [mm]
h_0	Sample height before deformation[mm]

ICP-OS	Inductively coupled plasma optical spectroscopy
J	Diffusion flux [mol/(m²·s)]
k	Numerical factor [-] or Bolzmann constant [J/s]
L	Distance parameter for cluster algorithm [nm]
l	Interparticle distance [nm]
MHC	Molybdenum based alloy containing 1.20 wt.% Hf and 0.1 wt.% C
N	Number of discrete rectangular blocks [-]
n	Number of solute atoms [-]
n_b	Bin size, number of atoms in a discrete rectangular block [-]
N_{het}	Heterogeneous nucleation sites [nuclei/(m³·s)]
OLM	Optical light microscopy
$Q_{s,b}$	Activation energy of surface or grain boundary diffusion [J]
R	Gas constant [J/(mol·K)]
r	Nuclei or particle radius [nm]
r_0	Mean diameter at time= 0 s [nm]
$r^{\#}$	Optimal particle radius for maximum particle strengthening [nm]
r^{*}	Critical radius for nucleation [nm]
$\bar{r}$	Mean radius [nm]
ROI	Region of interest
S	Factor which is proportional to $D \cdot \gamma_{\alpha\beta} \cdot X_e$
SEM	Scanning electron microscopy
S(θ)	Shape factor dependent of angle θ
T	Temperature [°C]
T_B	Temperature at section B of the TMP [°C]
T_d	Deformation temperature at point d of the TMP [°C]
T_E	Temperature at section E of the TMP [°C]
TEM	Transmission electron microscopy
T_G	Temperature at section G of the TMP [°C]
T_m	Homologous melting point [K]
TMP	Thermo-mechanical process
T_R	Room temperature [°C]
TTT	Time- temperature- transformation diagram (c-curve)
TZM	Molybdenum based alloy containing 0.50 wt.% Ti, 0.08 wt.% Zr and 0.01- 0.04 wt.% C
V	Volume [nm³]
V^*_{het}	Critical Volume for heterogeneous nucleation [nm³]
V^*_{hom}	Critical Volume for homogeneous nucleation [nm³]

X0	Alloy concentration X0 [at.%]
X_α	Concentration of matrix α [at.%]
X_β	Concentration of precipitate β [at.%]
Xe	Equilibrium composition [at.%]
Xr	Increased equilibrium composition [at.%]
XRD	X-ray diffraction
z	Numerical factor [-]

Table 1.1: Used abbreviations

Abstract

In the course of this thesis the precipitation behavior of Hf- carbide (HfC) in the molybdenum based alloy MHC was analyzed after thermo-mechanical treatment. The material of interest was a powder metallurgically processed molybdenum based alloy with 0.65 at.% Hf and 0.65 at.% C. The aim of this thesis was to reveal the mechanism of secondary HfC precipitation. The gained knowledge will serve as a basis for further improvements of the high temperature strength of this alloy. The experiments were carried out with atom probe tomography (APT) and transmission electron microscopy (TEM). The microstructure of the sintered material consisted of primary Hf- carbides and oxides within the grain and intergranular molybdenum carbide. APT measurements of the as-sintered condition showed a residual dissolved content of 0.12 at.% Hf, but no C. After deformation and subsequent aging in a deformation dilatometer, TEM studies revealed fine precipitates in a range of 10 to 100 nm preferentially at dislocations or dislocation networks. This indicates heterogeneous nucleation on dislocations which is assisted by pipe diffusion as mechanism for the secondary HfC precipitation in MHC. The C for this reaction is delivered by the intergranular molybdenum carbide which dissolves partially during aging. This had been elucidated with X-ray diffraction and optical light microscopy.

Keywords: molybdenum- hafnium- carbon alloy (MHC); precipitation hardening; precipitation mechanism; transmission electron microscopy; atom probe tomography; x-ray diffraction

Zusammenfassung

Im Zuge dieser Arbeit wurde das Ausscheidungsverhalten von Hafniumkarbid (HfC) in der Molybdänbasislegierung MHC nach vorangegangener thermomechanischer Behandlung analysiert. Bei dem untersuchten Werkstoff handelt es sich um eine pulvermetallurgisch hergestellte Molybdänbasislegierung mit 0,65 at.% Hf und 0,65 at.% C. Das Ziel war es, den Mechanismus der sekundären Ausscheidungsbildung von HfC zu klären, um gezielt Informationen zur Festigkeitssteigerung dieses Hochtemperaturwerkstoffes zu gewinnen. Die Untersuchungen hierfür wurden mittels Atomsondentomographie (APT) und Transmissionselektronenmikroskopie (TEM) durchgeführt. Das Gefüge des gesinterten Materials bestand aus primären Hafniumkarbiden und -oxiden in der Matrix sowie Molybdänkarbidsäumen an den Korngrenzen. Mittels APT wurde nach dem Sintern ein Hf Gehalt von 0,12 at.% festgestellt, es ist jedoch kein C gelöst. Nach Deformation und anschließender Auslagerung des Sinterzustandes in einem Umformdilatometer konnten mittels TEM feinste sekundäre Ausscheidungen, bevorzugt an Versetzungen und Versetzungsnetzwerken in der Größenordnung von 10 bis 100 nm festgestellt werden. Diese Kenntnisse weisen auf eine heterogene Keimbildung an Versetzungen und eine vermutlich erhöhte Kinetik durch Diffusion an Versetzungen als Mechanismus der sekundären Ausscheidungsbildung von HfC in MHC hin. Den C für diese Ausscheidungsreaktion liefert das Molybdänkarbid an den Korngrenzen, welches sich im Zuge der Auslagerungszeit teilweise auflöst. Dies konnte durch Röntgenbeugung und Lichtmikroskopie nachgewiesen werden.

Schlagwörter: Molybdän- Hafnium- Kohlenstofflegierung (MHC); Ausscheidungshärtung; Ausscheidungsmechanismus; Transmissionselektronenmikroskopie; Atomsondentomographie; Röntgendiffraktometrie

1 INTRODUCTION

In the 1960s and 1970s the development of ductile, high strength alloys of molybdenum and tungsten was of considerable interest for space and nuclear applications. These alloys have a high melting point and high young's modulus which makes them attractive for operation at elevated temperatures [1].

Especially the development of the alloy TZM (Ti- Zr- Mo) has shown the usefulness of group IVa carbides of titanium and zirconium in providing high strength at high temperatures. The potential of greater stability of HfC precipitates led to investigations of various molybdenum based alloys containing Hf and C. Outstanding mechanical properties, particularly for thermo-mechanically processed materials, were reported [2–4].

Due to the mechanism of precipitation hardening the creep resistance as well as the high temperature strength of the molybdenum based alloy MHC has been enhanced significantly. This allows operating temperatures up to 1550°C which exceeds TZM about 150°C. MHC meets the requirements for several practical applications e.g. forging dies for isothermal forging of super alloys, extrusion tools for copper alloys or X-ray rotating anodes for medical applications [5].

Generally, the strength of metals can be increased by the effects of work hardening, grain refinement, solid solution hardening and particle hardening. The raise of strength is mostly a combination of the above mentioned mechanisms. Unlike for TZM these different strengthening contributions are not very well investigated for MHC, especially the precipitation behavior, and thus possible operation limits and the maximum strengthening potential are not known yet.

Literature reports for TZM or Nb- TZM a mechanism where precipitates nucleate preferred on dislocations and that Mo_2C provides the C for this reaction by dissolving. For MHC no such mechanism is mentioned. A reason for that might be that all these studies refer to arc melted material which was solution annealed. In this case the precipitates formed during aging of the supersaturated solid solution [3-4].

Motivated to gain more expertise in modifying MHC, a PhD project was created to understand the individual influences on the total strength by Plansee SE and the Christian Doppler Laboratory for Early Stages of Precipitation (ESOP) which is located at the department of Physical Metallurgy and Materials Testing at the Montanuniversität Leoben.

This thesis is part of the above mentioned PhD project and has the overall aim to clarify the precipitation mechanism of secondary HfC in the MHC alloy during thermo-mechanical processing. The gained knowledge should provide data for the future quantification of the contribution of precipitation hardening on the strength of MHC and should serve as a basic work for further improvements of this alloy.

2 THEORETICAL BACKGROUND

2.1 Strengthening of metals

The strength of metals can be increased by the effects of work hardening, grain refinement, solid solution hardening and particle hardening. This thesis deals mainly with the hardening effect via particles. This can be achieved due to fine dispersions or by precipitation reactions. The optimal particle radius $r^{\#}$ for a maximum particle strengthening effect for coherent spherical particles is given by Equation 2.1 where G is the shear modulus, b is the Burgers vector and $\gamma_{\alpha\beta}$ is the interfacial energy between the matrix α and the particle β. This equation also shows that the desired critical particle radius does not depend on the volume fraction of the precipitated phase. Figure 2.1 illustrates the development of $\Delta\sigma$ with an increasing particle radius *r*. Only coherent interfaces can be cut by dislocations. With a certain particle size it is energetically favorable to change the dislocation/particle interaction mechanism from cutting to bowing. At this particle radius the Orowan stress for bowing is equal to the cutting stress. Dispersion and precipitation hardening are described in section 2.1.1 and 2.1.2 in detail [6].

$$r^{\#} = \frac{G \cdot b^2}{\gamma_{\alpha\beta}} \sqrt[3]{3} \qquad 2.1$$

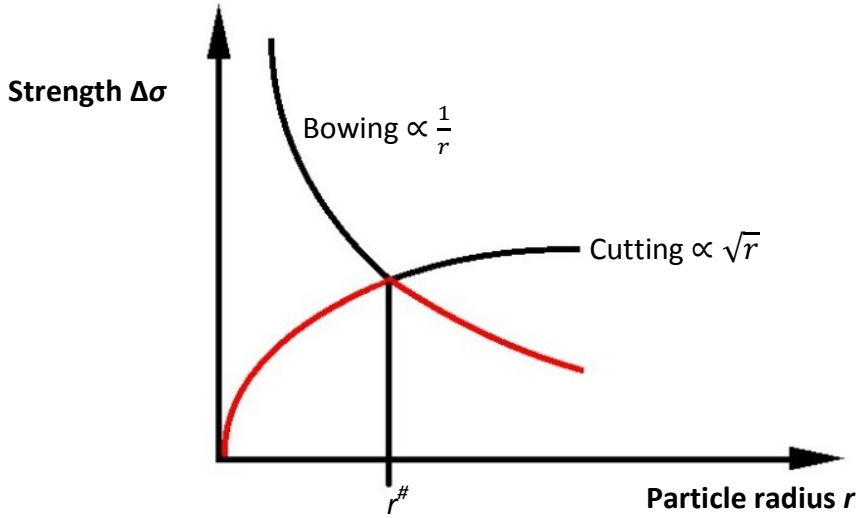

Figure 2.1: Development of yield strength with increasing particle radius *r* for spherical coherent particles [6].

2.1.1 Dispersion hardening

Non-metallic inclusions such as oxides, carbides, nitrides and borides can enhance the strength of metals due to hindering the movement of dislocations. Dislocations cannot cut the incoherent particles. They need to bypass this barrier with the Orowan mechanism which is illustrated in Figure 2.2. While bowing the curvature of the dislocation gets bigger until anti-parallel parts reconnect behind the particle and the dislocation gets released from it, however, a dislocation loop remains around the particle. The critical shear stress for this event increases with decreasing particle interdistance *l*. The increase of yield strength for dispersion hardened alloys is shown in Equation 2.2 and depends on the dispersion degree *f/r*, where *f* is the volume fraction of the particles and *k* is a numerical constant. The effect decreases at a constant volume fraction with *1/r* [6].

$$\Delta\sigma = k \cdot G \cdot b \cdot \frac{\sqrt{f}}{r} \qquad 2.2$$

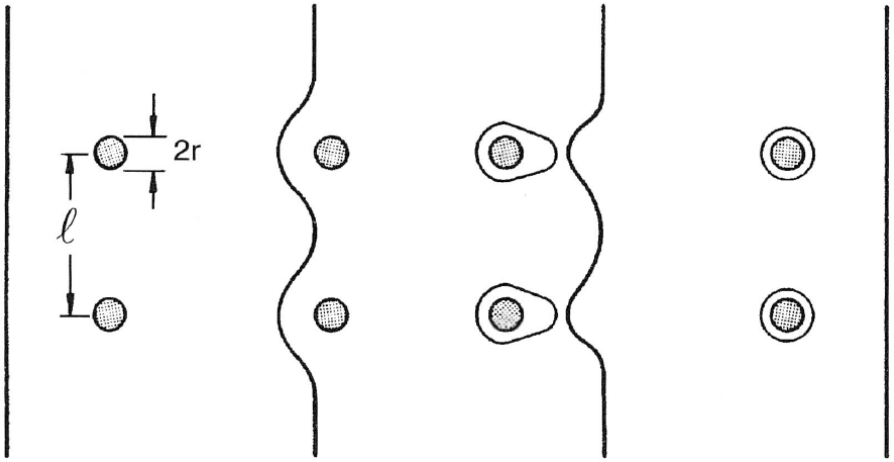

Figure 2.2: Successive stages of the Orowan mechanism of a dislocation to bypass a particle [6].

2.1.2 Precipitation hardening

Precipitates can form while cooling a solid solution from a single phase region to a multiple phase region. There are three different possible interphases which can develop (1) incoherent, (2) semicoherent and (3) coherent. Incoherent interfaces act like grain boundaries as barriers for dislocations which are difficult to overcome. In this case dislocations use the Orowan mechanism to bypass the incoherent precipitates. Dislocations are able to cut precipitates with a semicoherent or coherent interface due to equal crystallographic planes and directions. For this cutting process, which is illustrated in Figure

2.3, the dislocation needs to raise (1) the energy for the para- and dielastic interactions like in solid solution hardening, (2) the energy for additional interfaces caused by cutting and (3) if the particle is an ordered phase also the antiphase boundary energy γ_{APB}. The raise of yield strength caused by this cutting process is shown by Equation 2.3, where z is a numerical constant. The effect grows with $\sqrt{r_p}$ and following dislocations can pass easier through the precipitate due to a decreasing number of atomic bonds [6].

$$\Delta\sigma = \frac{z}{G \cdot b^2} \cdot \gamma_{\alpha\beta}^{\frac{3}{2}} \cdot \sqrt{f \cdot r} \qquad 2.3$$

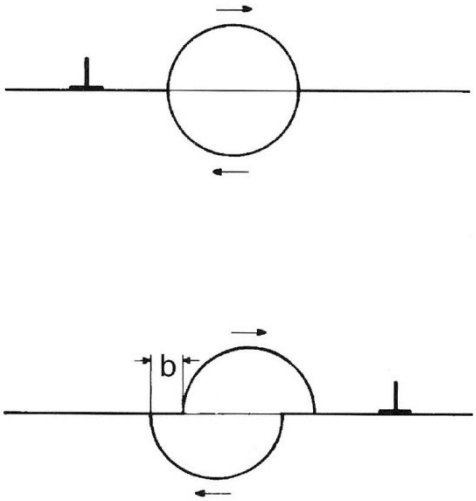

Figure 2.3: Cutting process of a (semi-)coherent precipitate [6].

2.2 Nucleation of precipitates

Nucleation of precipitates can occur either homogeneously or heterogeneously. Contrary to heterogeneous nucleation, which is a technologically more important subject and hence will be discussed in this thesis, homogeneous nucleation occurs without benefit of pre-existing heterogeneities such as dislocations, vacancies, grain boundaries, grain edges, grain corners, stacking faults or the surface of impurities. Such areas are regions of higher free energy and when a nucleus forms it replaces part of a boundary area or dislocation line which results in the destruction of the defect. Due to this destruction free energy ΔG_d will be released and it reduces, or even removes, the activation energy barrier [7-8]. The free energy for heterogeneous nucleation ΔG_{het} can be described as

$$\Delta G_{het} = -V \cdot (\Delta G_V - \Delta G_S) + A \cdot \gamma_{\alpha\beta} - \Delta G_d \tag{2.4}$$

where

- $V \cdot \Delta G_V$ is the term for volume free energy reduction due to creation of a volume V of β-phase
- $V \cdot \Delta G_S$ is the term for misfit strain energy per unit volume of β-phase
- $A \cdot \gamma_{\alpha\beta}$ is the interfacial free energy increase by creation of an area A
- ΔG_d is the defect free energy which will be released during destruction of a defect

Ignoring any misfit strain energy, the optimum nuclei shape for an incoherent grain-boundary nucleus is a shape which minimizes the total interfacial free energy like two abutted spherical caps (Figure 2.4 (a)). This grain boundary nucleation is analogous to solidification on a substrate. The critical radius of the nuclei, r^*, can be expressed with Equation 2.5 [7].

$$r^* = \frac{2 \cdot \gamma_{\alpha\beta}}{\Delta G_V - \Delta G_d} \tag{2.5}$$

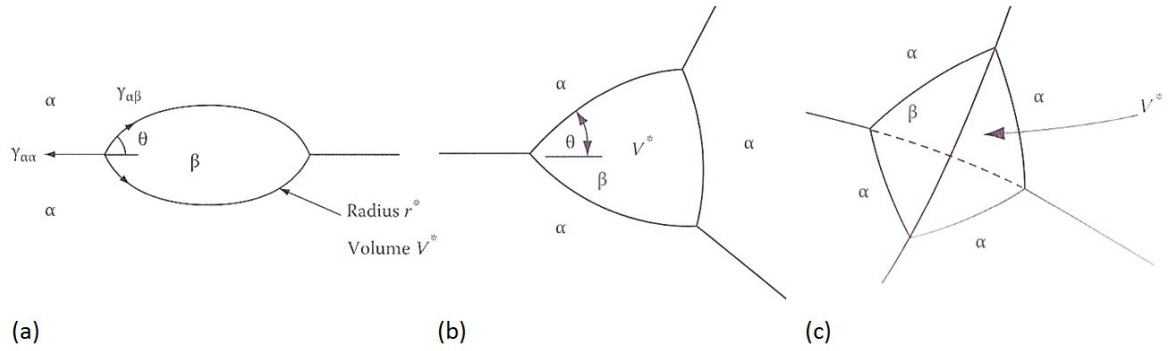

Figure 2.4: Critical nucleus shape for nucleation on (a) a grain boundary, (b) a grain edge or (c) a grain corner [7].

The ratio of the critical heterogeneous to the critical homogeneous nucleation energy or volume will be given by

$$\frac{\Delta G^*_{het}}{\Delta G^*_{hom}} = \frac{V^*_{het}}{V^*_{hom}} = S(\theta) \tag{2.6}$$

where $S(\theta)$ is a shape factor given by

$$S(\theta) = \frac{1}{2}(2 + cos\theta)^2(1 - cos\theta)^2 \tag{2.7}$$

The reduction of ΔG^*_{het} and the increase of the effectiveness of a grain boundary as a nucleation site depends on $cos\theta$, i.e., on the ratio $\gamma_{\alpha\alpha}/2\gamma_{\alpha\beta}$. It can be further reduced by nucleation on a grain edge or a grain corner which are illustrated in Figure 2.4 (b) and Figure 2.4 (c). Figure 2.5 shows how $\Delta G^*_{het}/\Delta G^*_{hom}$ depends on $cos\theta$ for various grain-boundary nucleation sites. Another reduction of ΔG^*_{het} can be achieved if the matrix and the precipitate are sufficient compatible with each other. In this case the precipitate will have an orientation relationship with one of the participating grains. Other planar defects such as interfaces of inclusions to the matrix, stacking faults and free surfaces can behave in similar ways as grain boundaries in reducing ΔG^* [7].

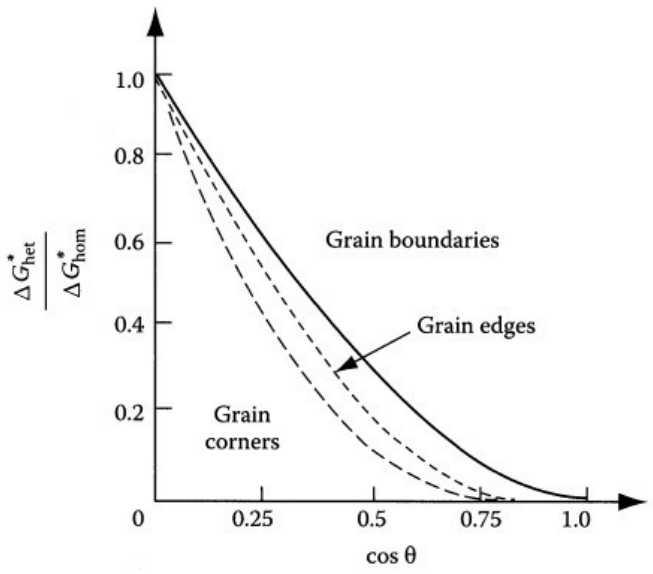

Figure 2.5: Effect of θ on the activation energy for grain boundary nucleation relative to homogeneous nucleation [7]**.**

The lattice distortion in the vicinity of a dislocation can assist nucleation in several ways. The main effect of dislocations is to reduce the total strain energy contribution of the embryonic

nuclei to ΔG^*. A coherent nucleus with a negative misfit, i.e., a smaller lattice spacing than the matrix, can reduce its ΔG^* by forming in the region of compressive strain above an edge dislocation. For a positive misfit it is energetically favorable the other way round [7].

Dislocations can also assist in growth of a nuclei beyond the critical size by providing pipe diffusion, i.e., in these regions exists a lower activation barrier for atomic migration [7]. This can be seen schematically for an incoherent nucleus in Figure 2.6 according to the theory of Cahn in 1957. He derived an expression for the catalytic power of a dislocation and shows that the activation barrier for nucleation becomes zero when the value of catalytic power reaches equilibrium [8-9].

Dislocations are not very effective for reducing the interfacial free energy contribution of ΔG^*. This means that nucleation on dislocations usually requires a good matching between precipitates and matrix on at least one plane, so that low-energy coherent or semicoherent interfaces can form. When the precipitate and matrix have different crystal structures the critical nucleus should therefore be disk- or needle-like [7].

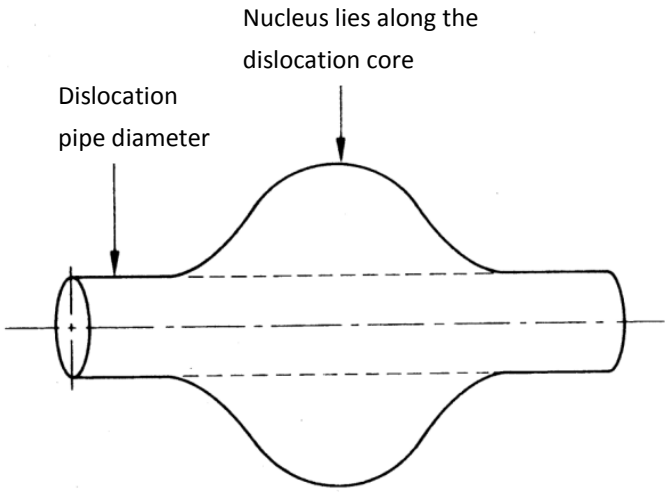

Figure 2.6: Cahn theory of nucleation on dislocations [8-9].

During the quench of age-hardening alloys from high temperatures excess vacancies form and remain in the material. These vacancies can assist nucleation by increasing diffusion rates, or by relieving misfit strain energies. They influence nucleation individually or collectively by grouping into small clusters but ΔG_d is relatively small for vacancies. This sort of nucleation will take place only when the combination of fully coherent nuclei, small

volume strain energy, and high driving force is given. These are basically the same conditions as required for homogeneous nucleation [7].

2.3 Development of precipitates

The equilibrium morphology of a coherent precipitate with a misfit is dictated by both the interfacial free energy and the elastic strain energy [10]. The Wulff theorem is used to determine the shape of a precipitate with a simple geometric construction that minimizes the total surface energy of a particle with a fixed volume. These energies can be visualized with a γ-plot. When elastic stress is present, the construction of an equilibrium shape is a complex task, involving the minimization of the sum of the interfacial and elastic energies. The resulting equilibrium shapes are often not simple geometric shapes (like a sphere or a spheroid), and thus predicting such shapes relies on numerical approaches. In addition, while the equilibrium shape of a stress-free particle is independent of the particle size, this is not the case when misfit stress is present (as in solid two-phase coherent alloys). Since the relative importance of elastic energy to interfacial energy increases with particle size, the equilibrium shape must be determined as a function of the particle size, or alternatively, of the relative importance of these two energies [11].

2.3.1 Interfacial energy effects

The system matrix α to precipitate β will have a minimum free energy when the shape of the precipitate and its orientation relationship to the matrix are optimized to give the lowest total interfacial free energy ($\Sigma A \cdot \gamma_{\alpha\beta}$), assuming that the matrix to precipitate interface is strain free [7].

2.3.1.1 Fully coherent precipitates

If the precipitate *β* has the same crystal structure and a similar lattice parameter to the matrix α, the two phases can form low-energy coherent interfaces on all sides. A γ-plot of the *α/β* interfacial energy would be largely spherical and, ignoring coherency strains, the equilibrium shape of the precipitate should be a sphere. If the atomic diameters of the involved atomic species differ not much, coherency strain will be a negligible contribution to the total free energy of the alloy. When the atomic size difference is much larger, strain energy is found to be more important than interfacial energy in determining the equilibrium shape of the precipitate [7].

2.3.1.2 Partially coherent precipitates

From an interfacial energy point of view it is favorable for a precipitate to be surrounded by low-energy coherent interfaces. But if the precipitate and the matrix have different crystal structures it is difficult to find a lattice plane that is common in both phases. For certain phase combinations there may be one plane that is more or less identical in each crystal, and by choosing the correct orientation relationship it is then possible for a low-energy coherent or semicoherent interface to be formed. Usually there are no other planes of good matching and the precipitate must consequently also be bounded by high-energy incoherent interfaces. Figure 2.7 shows a γ-plot (described in section 2.3) of the interfacial energy. In this case the equilibrium shape would be a disk with a thickness/diameter ratio of γ_c/γ_i, where γ_c and γ_i are the energies of the (semi-)coherent and incoherent interfaces. Triangular, square or hexagonal plate shapes would be predicted if the γ-plot also contains smaller cusps at symmetrically disposed positions in the plane of the plate [7].

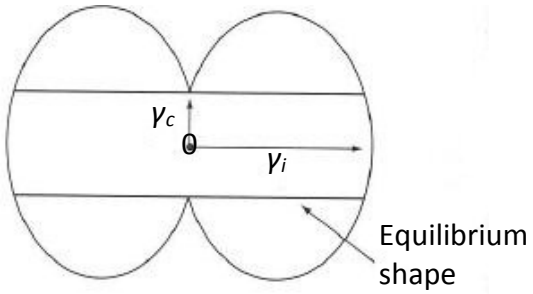

Figure 2.7: A section through a γ-plot for a precipitate showing one semi- or coherent interface, together with the equilibrium shape (a disk) [7].

2.3.1.3 Incoherent precipitates

When two phases have different crystal structures it is unlikely that any coherent or semicoherent interfaces form. Then the precipitate will be incoherent. The interfacial energy should be high for all interfacial planes, the γ-plot and the equilibrium inclusion shape will be roughly spherical. Under certain circumstances polyhedral shapes are also possible [7].

2.3.1.4 Precipitates on grain boundaries

In this special situation the precipitate can have (1) an incoherent interface to the adjacent grains, (2) a coherent or semicoherent interface with one grain or (3) a coherent or semicoherent interface with both grains. The first two cases are commonly encountered, but

due to very restrictive crystallographic conditions imposed by coherency with one grain, it is very unlikely that the precipitate will be coherent with the second grain [7].

2.3.2 Misfit strain effects

2.3.2.1 Fully coherent precipitates

The equilibrium shape of a coherent precipitate or zone can only be predicted by the γ-plot when the misfit between the precipitate and matrix is small. When misfit is present, the formation of coherent interfaces raises the free energy of the system on account of the elastic strain fields that arise. The condition for the equilibrium of this case is shown with Equation 2.8 [7].

$$\Sigma A_i \cdot \gamma_i + \Delta G_s = minimum \tag{2.8}$$

In order to compensate the strain caused by misfit and to produce fully coherent precipitates, the matrix and inclusion must be strained by equal and opposite forces. The unconstrained misfit δ can be calculated with Equation 2.9 where a_β and a_α are the lattice parameters for the unstrained precipitate and matrix [7].

$$\delta = \frac{a_\beta - a_\alpha}{a_\alpha} \tag{2.9}$$

When the precipitate is a thin disk, the misfit is no longer equal in all directions, but instead it is large perpendicular to the disk and almost zero in the plane of the broad faces, as shown in Figure 2.8. In general the elastic energy depends on the shape and elastic properties of both matrix and inclusion. The shape with minimum strain energy under these conditions is a disk parallel to {100} since most of the misfit is then accommodated in the soft lattice directions perpendicular to the disc [7].

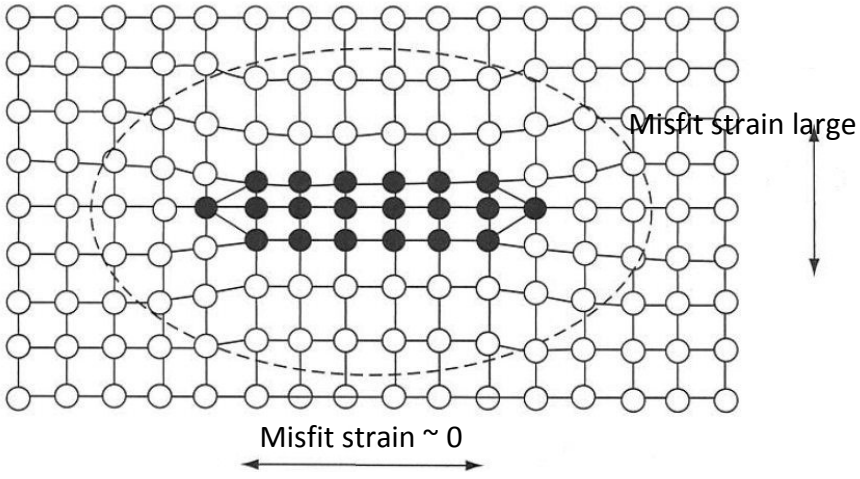

Figure 2.8: Influence of the lattice misfit on a fully coherent precipitate [7].

2.3.2.2 Incoherent precipitates

Since the lattice from an inclusion has no matching to the lattice of the matrix, there are no coherency strains. Misfit strains, however, still arise if the inclusion is the wrong size for the hole it is located in. Instead of the lattice misfit δ it has more significance to consider the volume misfit Δ which is described in Equation 2.10 where V is the Volume for an unconstrained hole and ΔV is the difference between a constrained and an unconstrained hole [7].

$$\Delta = \frac{\Delta V}{V} \tag{2.10}$$

The elastic strain energy ΔG_s for a homogeneous incompressible inclusion in an isotropic matrix is given by Equation 2.11 where G is the shear modulus of the matrix, Δ^2 is the square of the volume misfit which is proportional to the elastic strain energy and $f(c/a)$ is a factor that takes into account the shape effects as shown in Figure 2.9. For a given volume e.g. a sphere $f(c/a)$=1 which would mean it has the highest strain energy while a disk has very low strain energy. When Δ is small, the interfacial energy effects should dominate and the inclusion should be a sphere, otherwise it will be an oblate spheroid [7].

$$\Delta G_s = \frac{2}{3} \cdot G \cdot \Delta^2 \cdot V \cdot f(c/a) \tag{2.11}$$

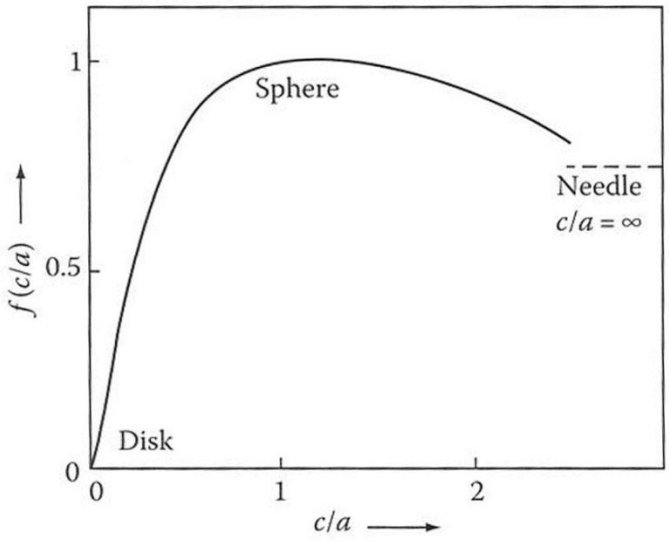

Figure 2.9: The variation of misfit strain energy with ellipsoid shape, $f(c/a)$ [7].

2.3.3 Precipitate growth

Nuclei with the lowest total interfacial free energy barrier have the smallest critical volume and thus these nuclei are usually bounded by a combination of coherent or semicoherent facets and smoothly curved incoherent interfaces, shown in Figure 2.10. (Semi-)coherent interfaces are forced to grow by a slower ledge mechanism where incoherent interfaces are highly mobile.

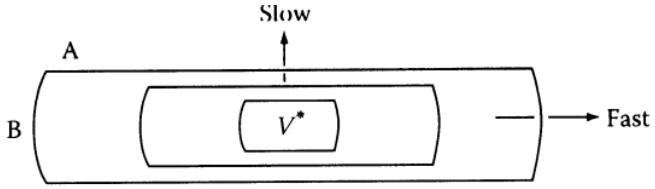

Figure 2.10: Effect of interface type on the morphology of a growing precipitate: A, low mobility (semi-)coherent interfaces; B, high-mobility incoherent interfaces [7].

Consequently, these precipitates will develop the shape of a disk or a plate [7]. These two different growth mechanisms which determine the shape of the precipitate will be discussed in detail in section 2.3.3.1and 2.3.3.2.

2.3.3.1 Diffusion controlled lengthening of plates and needles

The diffusion controlled lengthening rate ϑ of plates and needles can be described with Equation 2.8 where D is the interdiffusion coefficient, k is a numerical constant. ΔX_0 is the difference between the matrix concentration X_0 and the equilibrium concentration X_e, r^* is the critical nucleus radius that is required to reduce ΔX which is the difference between the matrix concentration X_0 and the increased equilibrium concentration X_r and X_β is the composition of the precipitate. Due to the Gibbs-Thomson effect, the equilibrium composition in the matrix adjacent to the edge of the precipitate will be increased to X_r, which can be seen in Figure 2.11 (a) and Figure 2.11 (b). The composition to drive the diffusion will depend on the tip radius of the plate-like precipitate. Equation 2.12 will apply as long as there is no decrease of supersaturation far from the interface due to other precipitates [7].

$$\vartheta = \frac{D \cdot \Delta X_0}{2(X_\beta - X_r)} \cdot \frac{1}{r}\left(1 - \frac{r^*}{r}\right) \tag{2.12}$$

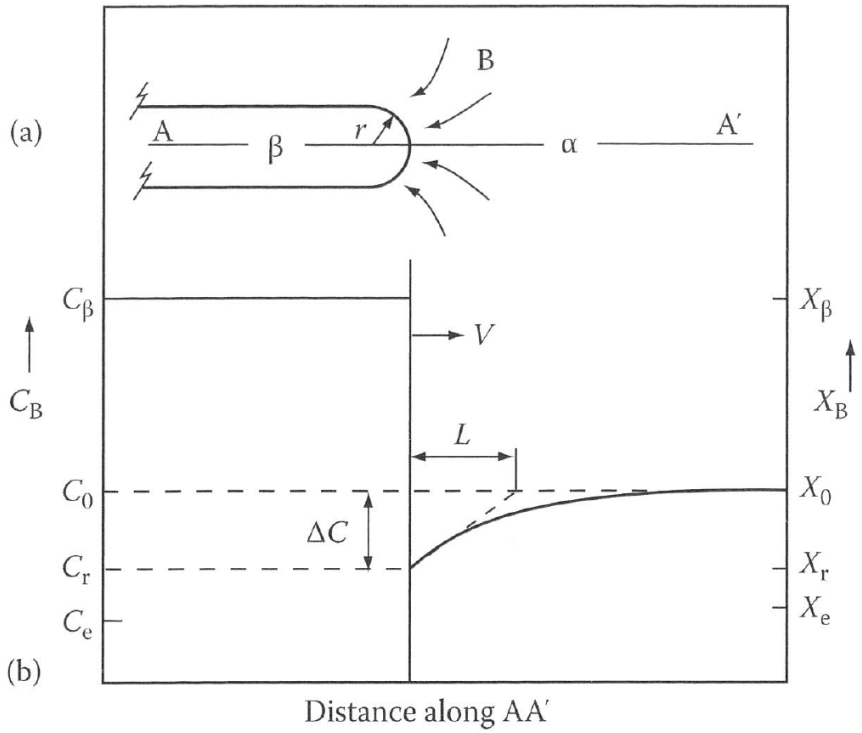

Figure 2.11: (a) Edge of a plate-like precipitate. (b) Concentration profile along AA' in (a) [7].

2.3.3.2 Thickening of plate-like precipitates

(Semi-)coherent faces of plate-like precipitates *θ* are restricted to migrate by the lateral movement of linear ledges of the spacing *λ* and height *h* which can be seen in Figure 2.12. This movement is caused by alignment of B atoms from the matrix α at the ledges of the precipitate β. The necessary composition changes required for precipitate growth must be achieved by long range diffusion similar to plate lengthening. In this case there is no Gibbs-Thomson effect existing and with $h \approx r$ follows that $X_e = X_r$. Equation 2.13 shows that the thickening rate ϑ is independent of h but inversely proportional to interledge spacing *λ*. This rate is not constant implying that ledge nucleation is rate controlling. Measurements in different systems indicate that even within the same system the thickness to time relationship can vary greatly from plate to plate [7].

$$\vartheta = \frac{D\Delta X_0}{k(X_\beta - X_e)\lambda} \tag{2.13}$$

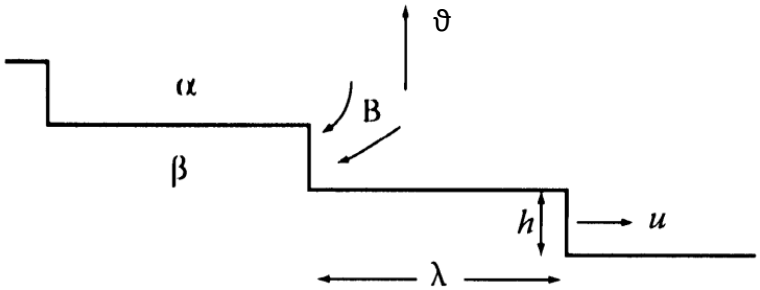

Figure 2.12: Thickening of plate-like precipitates by ledge mechanism [7].

2.4 Transformation kinetics

The progress of an isothermal phase transformation can be represented by plotting the transformed fraction as a function of time and temperature as shown as an example in Figure 2.13 (a) and Figure 2.13 (b). The volume fraction *f* can be defined as the volume of precipitates β at a certain time divided by the final volume of *β*. Among the factors that determine *f(t, T)* are the nucleation rate, the growth rate, the density and distribution of nucleation sites, the overlap of diffusion fields and the impingement from adjacent transformed volumes. After quenching to the transformation temperature the metastable *α*-phase will contain many nucleation sites and there can be three possible sequences [7]:

1. Nuclei form throughout the whole transformation process so that a wide range of particle sizes exists at any time. *f* will depend on the nucleation and growth rate.
2. If all potential nucleation sites are consumed in the process this is known as site saturation. *f* will only depend on the number of nucleation sites and the growth rate.
3. All the parent phase is consumed by the transformation product e.g. the formation of Pearlite. In this case the transformation terminates by the impingement of adjacent cells growing with a constant velocity.

At Temperatures close to T_e the driving force for transformation is very small so that both nucleation and subsequent growth rates are slow and long time is required for the transformation. When ΔT is very large slow diffusion rates limit the rate of transformation. A maximum rate is obtained at intermediate temperature differences. The transformed fraction *f* can be expressed with Equation 2.14 where *N* is the nucleation rate, ϑ is the growth rate and t is the time [7].

$$f = 1 - exp(-\frac{\pi}{3} N \cdot \vartheta^3 \cdot t^4) \qquad 2.14$$

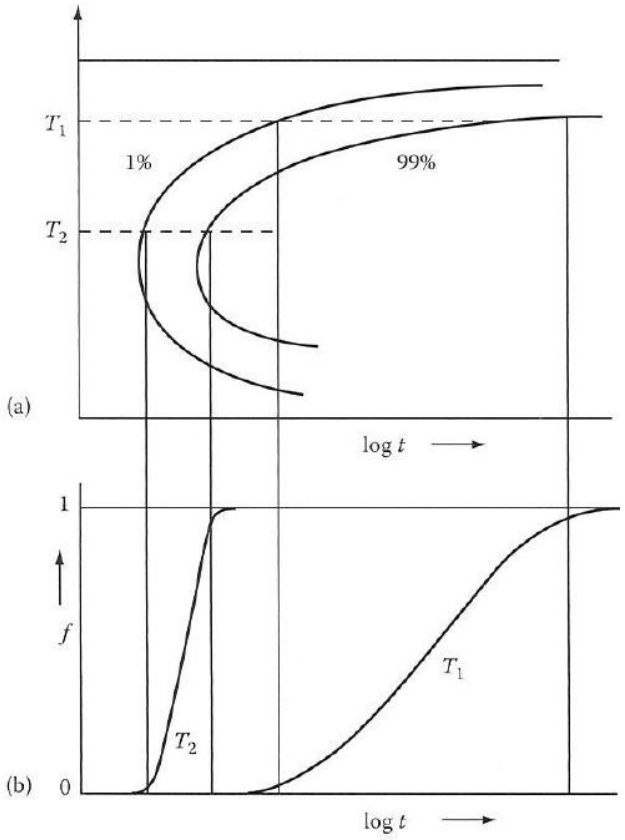

Figure 2.13: C-Curve. Percentage of transformation versus time for different transformation temperatures [7].

2.5 Particle coarsening

Ostwald ripening is the physical mechanism by which the microstructure is able to release excess surface energy caused by increased solubility of small particles. Due to the Gibbs-Thomson effect, the solute concentration in the matrix adjacent to a particle will increase as the radius of curvature decreases, which is illustrated in Figure 2.14 (a) and Figure 2.14 (b). This causes concentration gradients in the matrix and solute will diffuse in direction of the largest particles away from the smallest, so that these small particles shrink and finally disappear. Such coarsening processes often produce an undesirable degradation of properties such as loss of strength or disappearance of grain-boundary pinning effects. The overall result is that the number of particles decreases and the mean diameter $\bar{r}$ increases with time which can be expressed by Equation 2.15, assuming volume diffusion is the rate controlling factor, where r_0 is the mean diameter at t=0 and the factor S is proportional to D the diffusion coefficient, $\gamma_{\alpha\beta}$ the interfacial energy and X_e the equilibrium solubility of very large particles [7-8].

$$(\bar{r})^3 - r_0^3 = S \cdot t \qquad S \propto D \cdot \gamma_{\alpha\beta} \cdot X_e \tag{2.15}$$

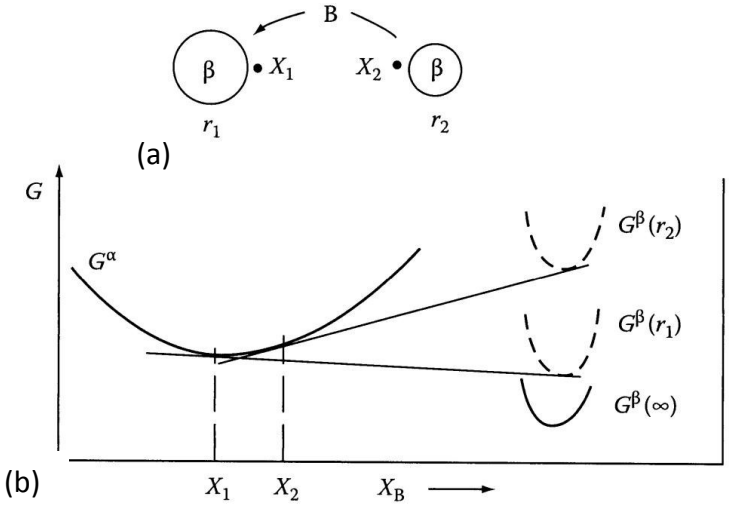

Figure 2.14: Origin of particle coarsening. β with small radius of curvature (r_2) has a higher molar free energy than β with a large radius of curvature (r_1). The concentration of solute is therefore highest outside the smallest particles [7].

High-temperature alloys whose strength depends on fine particles must have a low value at least at one of $\gamma_{\alpha\beta}$ (fully coherent), X_e (insoluble dispersions) or D (lower rates of coarsening e.g. with substitutional alloying elements) [7].

The rate controlling process of the coarsening behavior of precipitates on low angle subboundaries is pipe diffusion along the dislocations. In this case a r^4 relationship, as found for the geometrically similar grain boundary process, was established in 1972 [8].

2.6 Diffusion– high diffusivity paths

Defects like grain boundaries or dislocations are associated with a more open structure and it has been shown experimentally that the jump frequency for atoms migrating along these defects is higher than that for diffusion in the lattice. It will become apparent that under certain circumstances diffusion along these defects can be the dominant diffusion paths [7].

2.6.1 Diffusion along grain boundaries and free surfaces

Diffusion along grain boundaries and free surfaces can be described by Equation 2.16 where $D_{b,s}$ is the grain boundary or surface diffusivity, $D_{b,s0}$ is the frequency factor and $Q_{b,s}$ is the experimentally determined value for the activation energy for boundary or surface diffusion [7].

$$D_{b,s} = D_{b,s0} \cdot \exp(\frac{-Qb,s}{RT}) \tag{2.16}$$

In general is $D_s > D_b > D_1$ where D_1 is the defect-free lattice diffusivity parameter. The contribution of grain boundary diffusion to the total flux, e.g. of a sheet, will depend on the relative cross-sectional areas through which the solute is conducted. For simplification it is assumed in this example that the grain boundaries are perpendicular to the sheet and the concentration gradients in the lattice and boundary are identical. If the grain boundary has an effective thickness δ and the grain size is d the total flux will be given by Equation 2.17. The apparent diffusion coefficient D_{app} for this case is given in Equation 2.18 [7].

$$J = \frac{J_b\delta + J_1 d}{d} = -(\frac{D_b\delta + D_1 d}{d})\frac{dC}{dx} \tag{2.17}$$

$$\frac{D_{app}}{D_1} = 1 + \frac{D_b\delta}{D_1 d} \tag{2.18}$$

The relative lattice to grain boundary diffusion depends on the ratio $D_b \cdot \delta / D_1 \cdot d$. When $D_b \cdot \delta \gg D_1 \cdot d$ diffusion through the lattice can be ignored in comparison to grain boundary diffusion which then is a significant contribution to the total flux. In general, it is found that grain boundary diffusion becomes important below $0{,}75– 0{,}8 \cdot T_m$ [7].

2.6.2 Diffusion along dislocations

In this special kind of diffusion the dislocations can act as high diffusivity paths (“pipes”) and the total contribution to the flux will depend on the relative cross-sectional areas of pipe and matrix. Using the simple model illustrated in Figure 2.15 it can be shown with Equation 2.19 that the apparent diffusivity D_{app} through a single crystal containing dislocations is related to the lattice diffusion coefficient. g is the cross-sectional area of pipes per unit area of matrix and D_p is the diffusivity coefficient for pipe diffusion [7].

$$\frac{D_{app}}{D_1} = 1 + g \cdot \frac{D_p}{D_1} \tag{2.19}$$

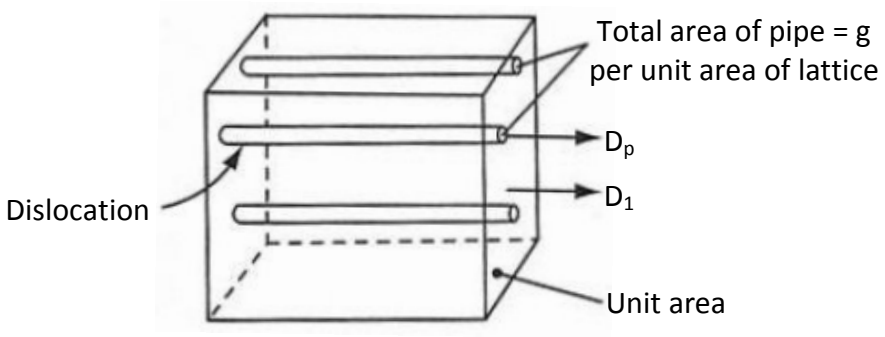

Figure 2.15: Dislocations act as high conductivity path through the lattice [7].

Measurements of the diffusion coefficient of small angle boundaries in Ag bicrystals, which are built up with edge dislocations, showed increasing diffusion coefficients with increasing boundary angle θ. Up to an angle of 16 degrees are the diffusion coefficients parallel in the Arrhenius plot due to unchanged activation enthalpy [12].

2.7 State of the art of the precipitation behavior of Mo- Hf- C alloys

Hf- carbide (HfC) has of all group IVa carbides the highest free energy of formation, thus it was expected to be the most stable precipitated phase in refractory metals at high temperatures. The high temperature stability of HfC precipitates in tungsten alloys suggested that similar molybdenum based alloys might also have attractive strength properties. Therefore, different arc melted Mo- Hf- C alloys with varying contents of Hf and C had been studied in different thermo-mechanically processed conditions by Raffo [3-4]. In order to prevent decarburization, Raffo conducted all annealing heat treatments in an atmosphere of argon with 0.3 % methane. The furnace was equipped to quench the specimens in helium after the heat treatment. The typical C containing phases in a Mo- Hf- C alloy are intergranular molybdenum carbide and HfC precipitates within the Mo grains. Raffo observed that for dilute alloys the major carbide phase was molybdenum carbide rather than Hf- carbide [4]. Malashenko reports that the formation of Mo_2C phase at grain boundaries is prevented or decreased with increasing Hf contents [13].

Outstanding mechanical properties had been reported for a thermo-mechanically processed alloy containing 0.6 at.% Hf and 0.5 at.% C. This metastable alloy had been solution treated and precipitation occurred during deformation. Transmission electron microscope (TEM) investigations confirmed plate-like HfC precipitates in the size ~100 nm and less. Figure 2.16 illustrates e.g. the tensile strength of the above mentioned alloy in comparison to Mo- Nb-TZM, Mo- TZC and other differently processed Mo- Hf- C alloys [3].

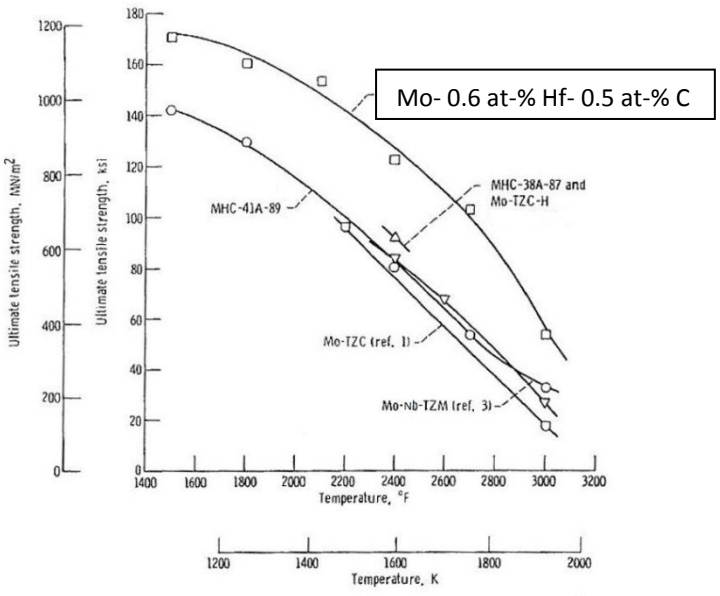

Figure 2.16: Ultimate tensile strength as a function of temperature for different wrought molybdenum alloys [3].

The strength of the aged alloys Mo- Nb- TZM and Mo- TZC is based on a solution heat treatment and an aging step was conducted prior to the final strain hardening. Such a process does not produce optimum mechanical behavior for Mo- Hf- C alloys. The reason for this is considered to be in the differences in the precipitation process for the two types of alloys. It was discovered by Ryan that the precipitation in Mo- TZC and Mo- Nb- TZM occurs via conversion of Mo_2C to a mixed titanium- zirconium monocarbide or in the other case in a NbC [14]. In contrast Raffo and Ryan had a solution annealed and quenched (supersaturated) alloy of Mo- Hf- C and consequently there was no Mo_2C present and HfC precipitation developed directly from solid solution during aging [3,14]. Ryan mentioned that Zr compounds appear to precipitate preferentially on matrix dislocations, whereas the Hf compounds are widely distributed [14].

Ryan focused in his studies on the formation and stability of group IVa carbides and nitrides, which all have a fcc NaCl structure with similar lattice parameters (*a* is within a 10% range) in molybdenum i.e. also Hf- carbides. He investigated the orientation relationship between the matrix and the precipitates in detail and reported that Hf- carbides as well as nitrides exhibit a cubic {100} habit plane which is different for TiC and TiN. The orientation relationship between Hf- carbides and nitrides with the matrix has been described as follows [15]:

$$\{100\}_{Mo} \,//\, \{100\}_{ppt}$$

$$<100>_{Mo} \,//\, <110>_{ppt}$$

$$<110>_{Mo} \,//\, <100>_{ppt}$$

Figure 2.17 shows a 3D model of the orientation relationship between a bcc molybdenum lattice (yellow) and the lattice of HfC (Hf red, C white) with a sodium chloride structure.

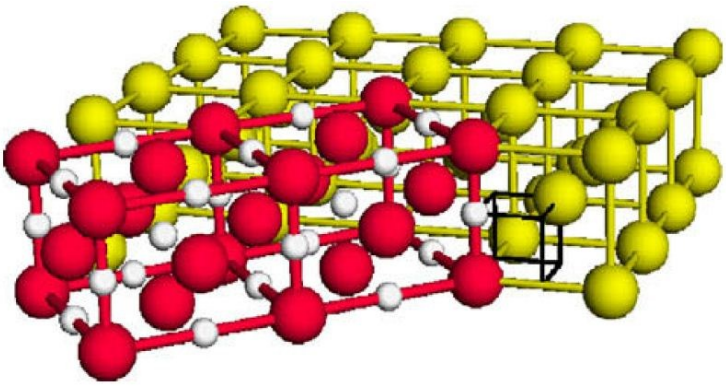

Figure 2.17: Lattice model for the orientation relationship between a bcc molybdenum lattice (yellow) and the constrained structure of HfC (red). The C spheres are white [16].

Ryan also observed contrast effects in the TEM images in the early stages of aging. He interpreted these effects as fully coherent precipitates of the above mentioned carbides and nitrides. With further aging the precipitates displayed a characteristic plate-like morphology. Strain energy in precipitation processes in solid state is considered to arise essentially from two sources, (1) the dilatational effects associated with a difference in specific volume of parent and product phases, and (2) elastic strain energy associated in establishing a good "fit" across a low-energy coherent interface. This orientation relationship is dictated by minimizing of dilatational and elastic strain energies, which is low for a coherent (semicoherent) interface. The mismatch between the precipitate and matrix is therefore a major factor for the formation of a particular morphology. An atomic model for the matching of fcc precipitates in a bcc matrix is shown in Figure 2.18. The match especially between HfC precipitates and matrix along nominated directions is illustrated in Table 2.1. These values are represented again for HfC in Figure 2.19, where the mismatch values between the Mo matrix and ZrC, ZrN, HfC and HfN precipitates are printed in a diagram [15].

Table 2.1: Misfit between HfC precipitate and matrix along nominated directions [15].

Molybdenum bcc 3.147 [Å]		HfC fcc 4.646 [Å]		Misfit [%]
Direction	Spacing [Å]	Direction	Spacing [Å]	
<111>	2.725	<110>	3.284	20.50
<100>	3.147	<110>	3.284	4.30
<110>	4.449	<100>	4.646	4.40
<311>	5.217	<211>	5.691	9.10
<331>	6.813	<310>	7.345	7.80
<210>	7.037	<310>	7.345	4.40
<210>	7.037	<111>	8.047	14.30
<211>	7.709	<321>	8.693	12.70
<221>	9.440	<210>	10.39	10.00
<310>	9.950	<210>	10.39	4.40
<310>	9.950	<332>	10.89	9.40
<332>	14.76	<320>	16.75	13.50

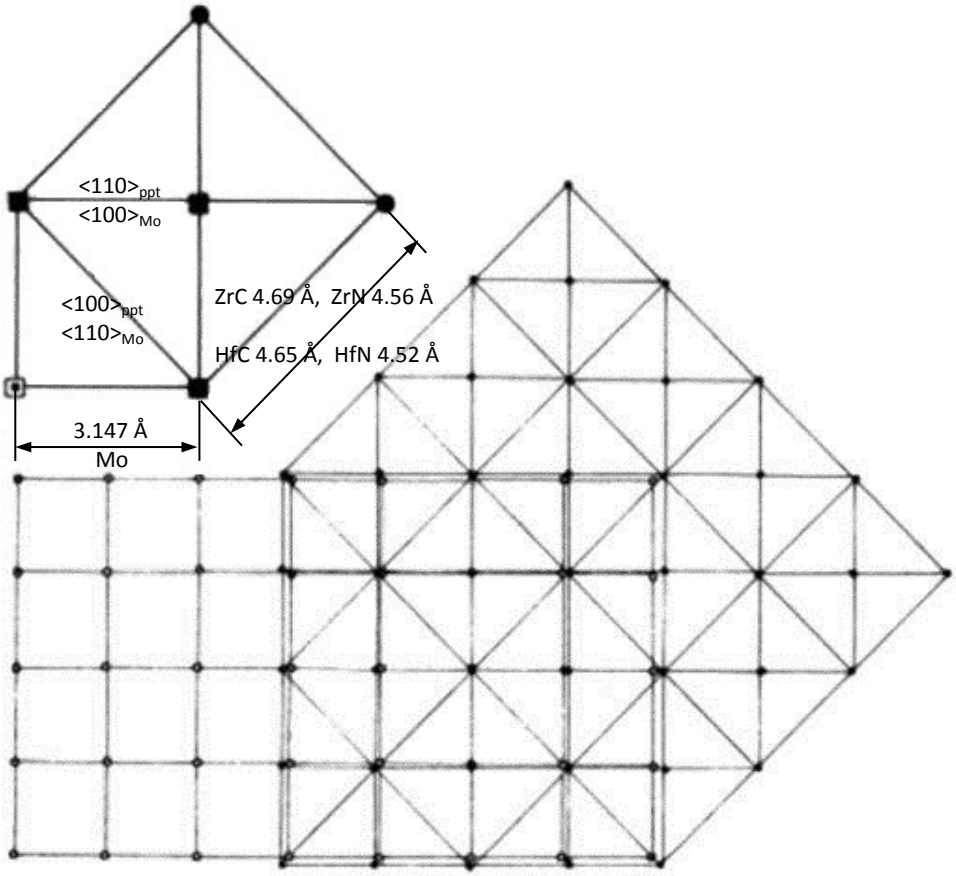

Figure 2.18: Interfacial matching of Mo bcc and precipitate fcc lattices (ZrC, ZrN, HfC & HfN) across $\{100\}_{Mo}$ // $\{100\}_{ppt}$ [15].

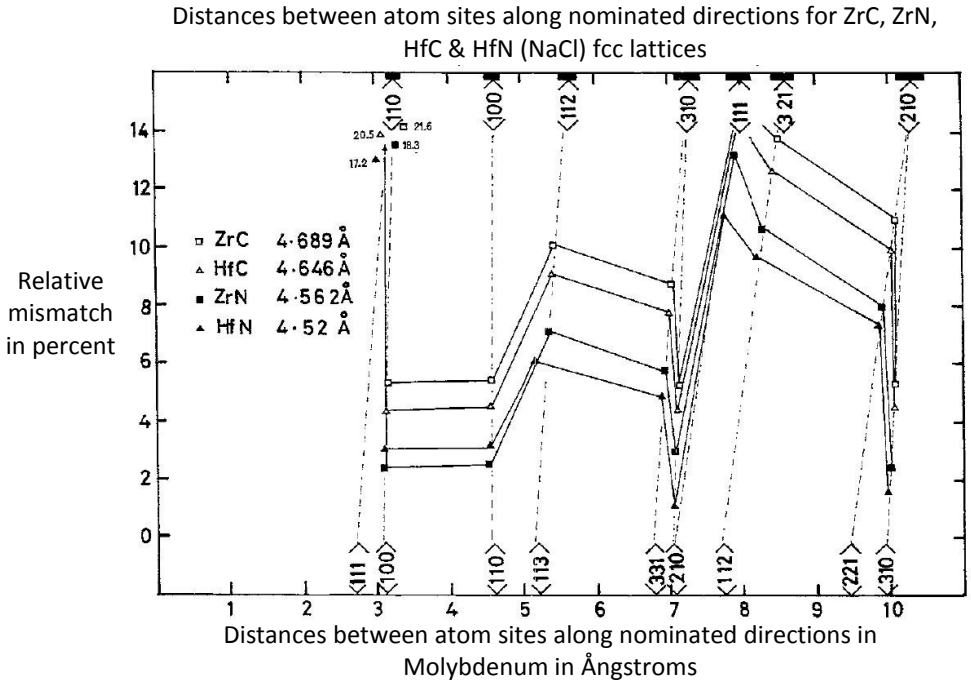

Figure 2.19: Graphical representation of mismatch data along various nominated directions in Mo- ZrC, ZrN, HfC, HfN [15].

Optical light microscopy (OLM) investigations revealed a microstructure of the as-sintered condition with primary Hf- carbides, Hf- oxide particles and intergranular molybdenum carbide. The samples were etched according to Hasson. The primary HfC precipitates were located within the matrix and had a length of ~1 µm. Hf- oxide particles were either inside the grain or at grain boundaries were it was usually in combination with the intergranular Mo_2C. X-Ray diffraction patterns revealed that the measured peaks for primary HfC in MHC are shifted to higher diffraction angles 2θ, compared to the HfC peak positions from diffraction data in literature. That deviation might be due to a different Hf/C ratio or rather due to a substitution of Hf by elements with a smaller atomic radius (e.g. Mo). The peaks for Mo_2C and HfO_2 were at the expected positions. Therefore it was assumed that these phases have a stoichiometric composition. The chemistry of the HfC phase was also analyzed at a carbide which was etched free from the matrix using TEM and electron diffraction spectroscopy (EDS). These measurements revealed that the primary carbide contained Hf, C, Mo and traces of Zr. Thus it was assumed that a fraction of the Hf atoms in the HfC was displaced by Mo atoms with a smaller atomic radius. This substitution led to a smaller lattice spacing of the fcc structure and consequently to a peak shift in the XRD patterns to higher 2θ angles. Consequently primary precipitates in MHC are Hf- rich carbides ((Hf,Mo)C) [17].

Hf- carbide is a very stable carbide, which is, like all carbides and nitrides, extremely hard, refractory and has a high resistance to wear, corrosion and heat [18]. Figure 2.20 shows the sodium chloride structure of Hf- carbide. In Table 2.2 are some physical parameters of this carbide listed.

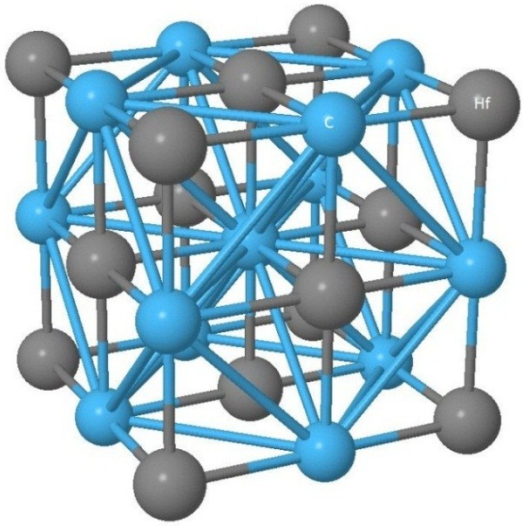

Figure 2.20: Fcc sodium chloride structure of Hf- carbide, blue C atoms, grey Hf atoms [19].

Table 2.2: Physical data of HfC [19-20].

Properties	***Value***
Color	Dark Grey
Molar weight	190.50 g/mol
Density ρ	12.20 g/cm³
Crystal structure	Fcc, Sodium chloride structure
Melting Point T_m	3890°C
Energy of Formation ΔHf_0	-244 kJ/mol at 298K
Lattice parameter a	4.6379 Å
Electrical resistivity ρ	$3.30 \cdot 10^{-7}$ Ω·m at 300K $1.59 \cdot 10^{-7}$ Ω·m at 0K
Electrical conductivity σ	$1.4 \cdot 10^{-6}$ $1/\Omega^{-1} \cdot m^{-1}$ at 298K
Thermal conductivity λ_{th}	20 $W/m^{-1} \cdot K^{-1}$ at 323K
Stiffness parameter, calculated values	C_{11}=554 GPa T<80K C_{12}=132 GPa T<80K C_{44}=228 GPa T<80K
Thermal expansion a	$7.54 \cdot 10^{-6}$ K^{-1}
Superconducting transition temperature T_C	0.04 K

3 EXPERIMENTAL PROCEDURES

3.1 Dilatometry

The compressive deformation experiments of the sintered samples with a length of 10 mm and a diameter of 5 mm were carried out with a deformation dilatometer DIL805 A/D from Bähr Thermoanalyse GmbH. The inductive heating principle requires electrically conductivity of the sample material. The deformation punches were made of Si_3N_4 and the pushrods for the dilatation measurement of alumina. The temperature was measured with type B thermocouples (positive pole Pt30Rh and negative pole Pt6Rh) according to DIN EN 60584-1:1996. High cooling rates were realized with gaseous nitrogen. A deformation speed of $\dot{\varphi}$=10 s^{-1} was chosen for all experiments in order to simulate the manufacturing conditions.

Heat treatments of the sintered samples without deformation were carried out with a quenching dilatometer DIL805 A from Bähr Thermoanalyse GmbH. This dilatometer has the same configurations as described above, except there is no deformation unit existing. The samples are kept in place directly by the dilatation measurement system instead of the deformation punches.

All experiments, whether in the deformation or quenching dilatometer, were carried out in a in a vacuum of < $5 \cdot 10^{-4}$ mbar. The details regarding deformation and heat treatment experiments are described in the thermo-mechanical process (TMP) in section 4.1 and in the sampling plan in section 4.2.

Due to friction phenomena deformation inhomogeneities, shown in Figure 3.1, are arising within the sample when deforming cylindrically samples [21]. Therefore, the specimen material for the conducted investigations was only taken from the center of the deformed samples.

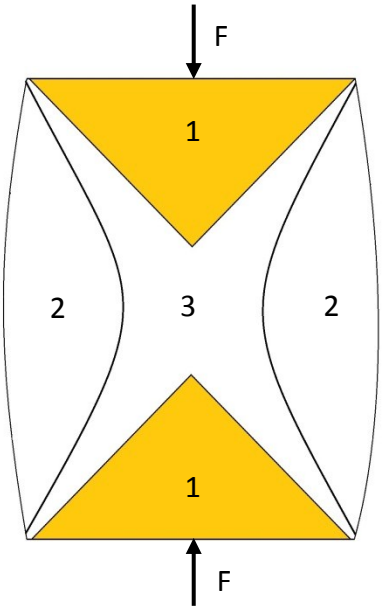

Figure 3.1: Deformation inhomogeneities in a deformed dilatometer sample. Number 1 marks the “dead” zone, number 2 the buckling area and number 3 the area with the most deformation [21].

3.2 Optical light microscopy (OLM)

The investigation of the microstructure was carried out with a Polyvar Met light microscope from Reichert, equipped with a Color View Soft Imaging System in combination with the Software analySIS from Olympus.

The samples for the OLM investigations were cut, according to Figure 3.2, along the colored areas with a Struers Accutom-5 precision cutter using an alumina cutting wheel. The blue and red areas were taken for further sample preparation for OLM investigations. These areas were embedded face-on in Polyfast resin with a Cito Press-20 both from Struers. OLM micrographs from the red region were only taken from center near areas due to deformation inhomogeneities in the deformed samples (Figure 3.1).

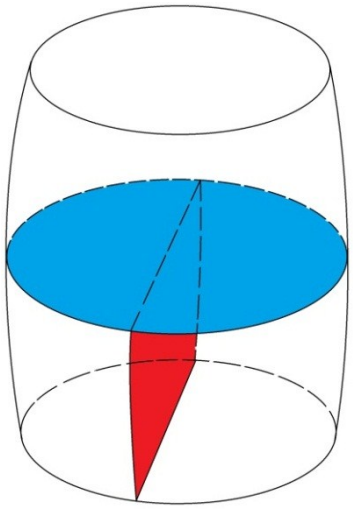

Figure 3.2: Cutting sequence (red and blue area) for OLM specimens from MHC samples.

To investigate the microstructure of the MHC alloy, the following preparation sequence was carried out. At first the specimen was ground using silicon carbide paper with a grit size of 320 and 500 for less than two minutes with a force of 25 N per specimen. The subsequent polishing steps were done with 9 µm and 3 µm diamond suspension by using the polishing cloths “Struers MD-Allegro and MD-Mol” for 8 minutes each with the same force as during grinding. The last polishing step was carried out with 0.04 µm silica oxide particle suspension (OP-S) on a “Struers MD-Chem” polishing cloth for at least 12 minutes with a force of 25 N per specimen. After the grinding and polishing the samples were color etched with Hasson etchant [17,22].

3.3 Micro hardness testing

The HV0.1 micro hardness testing was carried out according to DIN EN ISO 6507-1 at the polished and etched OLM samples with a Micro-DUROMAT 4000 from Reichert Jung which is connected to the PolyvarMet OLM.

3.4 Scanning electron microscopy (SEM)

SEM examinations were done with a Zeiss Evo 50 equipped with an Oxford EDS system and with a FEI Quanta 200 FEG. In order to detect the subgrain structure of MHC, the samples were prepared the same way like described in section 3.2, but the last polishing step with OP-S was not carried out. Instead of that, the samples were electro-polished with a Lectro Pol-5 using a proprietary A3 electrolyte from Struers. The applied voltage was 28 V, further parameters were room temperature (RT), a flow rate of 10, 8 s polishing time and a mask of 0.5 cm^2. This polishing step was done twice with one minute interruption time in order to cool the specimens [23].

3.5 Transmission electron microscopy (TEM)

TEM experiments were conducted with a PHILIPS TEM CM12 with a camera constant of 680 Å·cm at a length of 680 mm and an operation voltage of 120 kV. For the element quantification an EDS System from EDAX was used. Investigations of particle to matrix interfaces were carried out with a FEI TECNAI F20 which is also equipped with an EDS System from EDAX. The operation voltage of this HRTEM was 200 kV. The TEM images were analyzed with the software DigitalMicrograph^{TM} version 3.7.1 by Gatan Incorporation.

Thin discs with 0.3 mm thickness were cut out from the cross section of the different samples. Form deformed samples, shown in Figure 3.3, only two specimens were taken from the center in order to avoid specimen preparation from undeformed areas which (shown in Figure 3.1). This was carried out with a Struers Accutom-5 precision cutter using an alumina wheel. From these discs smaller discs with 3 mm in diameter were punched out with a hole-puncher. Afterwards the 3 mm diameter discs were ground down to approximately 0.1 mm thickness using a self-made sample holder and silicon carbide papers with a grit size of 1200, 2400 as well as 4000. Finally, the ground specimens were electro-polished with a Tenu Pol-5 from Struers using 12.5% sulphuric acid-ethanol solution [24]. This was carried out at 18V sample voltage and a pump flow rate of 13. The electrolyte was cooled in the freezer prior to usage and used at approximately -5 to 0°C.

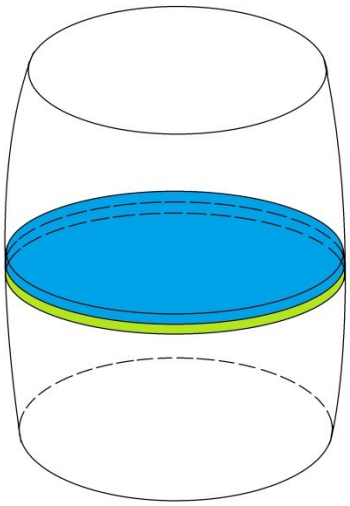

Figure 3.3: Cutting sequence for TEM thin foil preparation from deformed samples.

3.6 Atom probe tomography (APT)

Atom probe experiments were done with a LEAP 3000X HR from IMAGO SIENTIFIC INSTRUMENTS. The specimen temperatures were 60 and 90 K (see sampling plan in section 4.2). The pulse fraction was in all experiments 15 % of the basic voltage and the evaporation rate was 1 %. The atom probe worked with a frequency of 200 kHz and a vacuum of $8 \cdot 10^{-11}$ mbar. The mode of operation as well as the limitations of a 3D atom probe can be deduced from literature [25–29].

The starting shape of an atom probe specimen is a rod with a cross section of approximately ~0.3x0.3 mm^2 which is shown in Figure 3.4. The cutting was performed longitudinal at the (un-)deformed samples with an Accutom-5 precision cutter from Struers. Only two rods from the center of each deformed sample were taken in order to avoid sample preparation from undeformed areas which is shown in Figure 3.1.

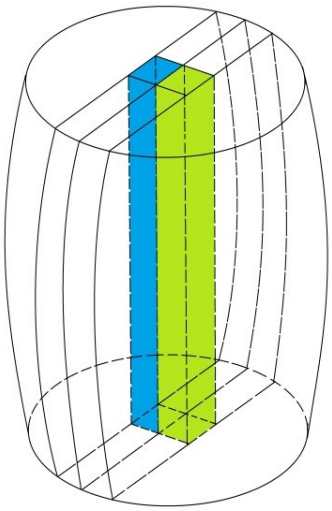

Figure 3.4: Cutting sequence for atom probe specimen preparation.

The electro-polishing steps for the APT specimens were carried out with 12 Volt DC. Due to pores in the matrix and the existence of primary carbides, a successful preparation of atom probe tips with a two stage process, shown in Figure 3.5 (a), was rather difficult. Tip material was removed preferentially at the interface carbide/matrix and at the neck of pores which resulted in blunt tips. Consequently, the sequence of the preparation was changed. The first stage was carried out with the same configurations. When the neck was already very thin a lower voltage level was introduced for finer polishing conditions and two tips were produced. Afterwards, micro-looping, shown in Figure 3.5 (b), was conducted with the

intention to have better control in sharpening the specimens. Even with these variations in the process, the result was that the prepared specimen didn't even start to work in the atom probe due to blunt tips or they broke within insufficient time of measurement at the neck of pores. SEM pictures of electro-polished MHC specimens, which illustrate the problem of existing pores and massive carbides in the specimen preparation, are shown in Figure 3.6 (a) and Figure 3.6 (b).

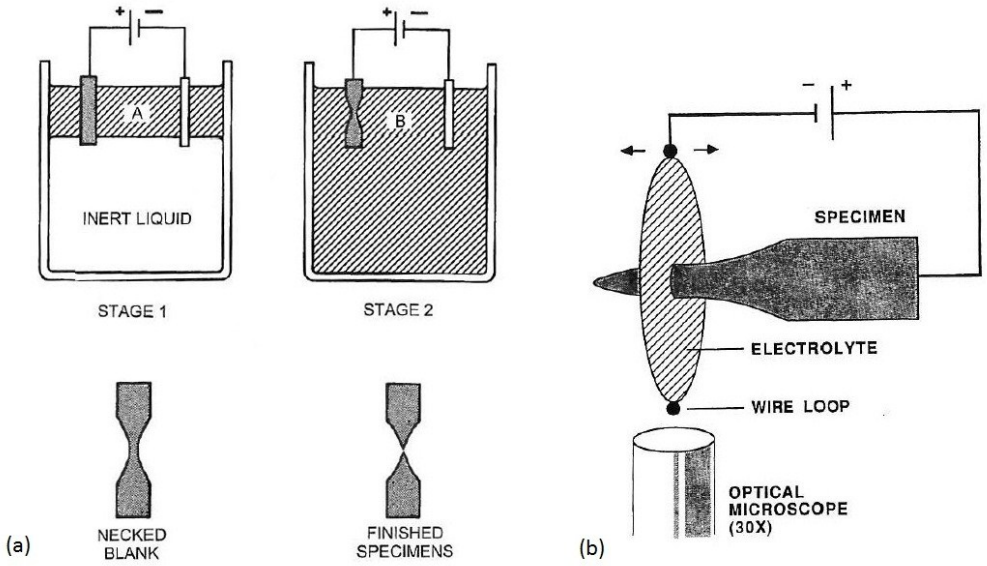

Figure 3.5: Electro-chemical preparation of atom probe specimens. (a) A typical two-stage electro-polishing process in order to gain atom probe tips. (b) Sharpening of a ruptured or blunt atom probe tips with a microloop [30].

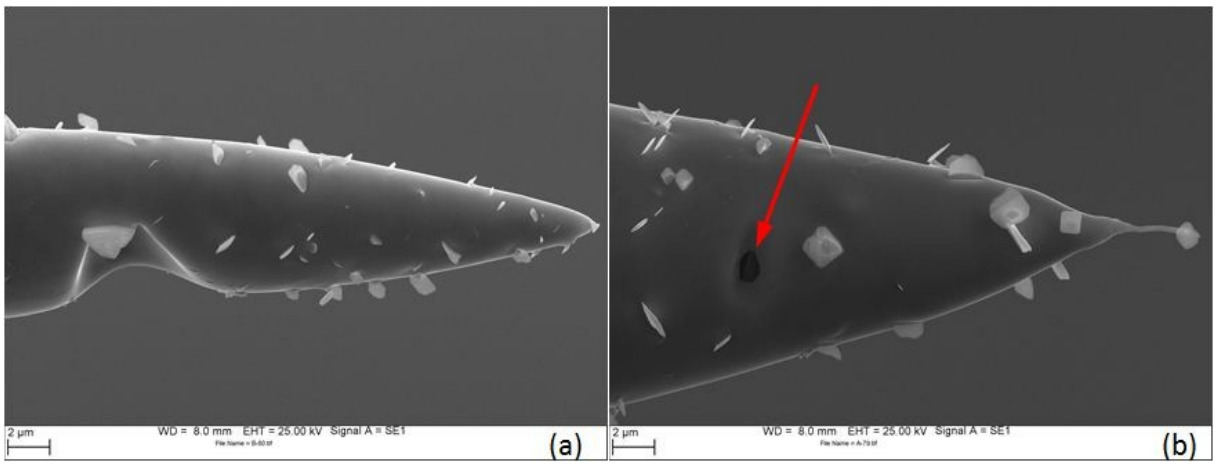

Figure 3.6: SEM images of electro-polished atom probe tips produced with modified stage 1 and micro loop. (a) Blunt tip with primary plate-like (Hf,Mo)C carbides and a massive pore. (b) Specimen with a (Hf,Mo)C carbide directly at the point of the tip and a hidden pore (marked with a red arrow).

Finally, the electro-polished tips were re-sharpened with focused ion beam (FIB) annular milling. At the beginning of this thesis this was done with a FEI Quanta 200 3D DBFIB. The preparation was carried out according to a preparation method for a Si wafer. First, the tip was annular milled with 30kV and then cleaned up with either 5kV or 2kV to minimize the penetration depth of the Ga^+ [31]. The size of the annular milling pattern depends on the size of the tip to be sharpened. The tips for the last APT experiments were produced with a FEI VERSA 3D Dual Beam SEM/FIB. The same parameters were used, but instead of one cleaning step both steps at 5 kV and 2 kV were done. In Figure 3.7 illustrates a tip of the as-sintered condition (SC) with two hidden pores, which were exposed during re-sharpening. Figure 3.8 shows a well prepared MHC atom probe specimen from the sintered condition at point j (SCj, see section 4.2) without any potential failure sources.

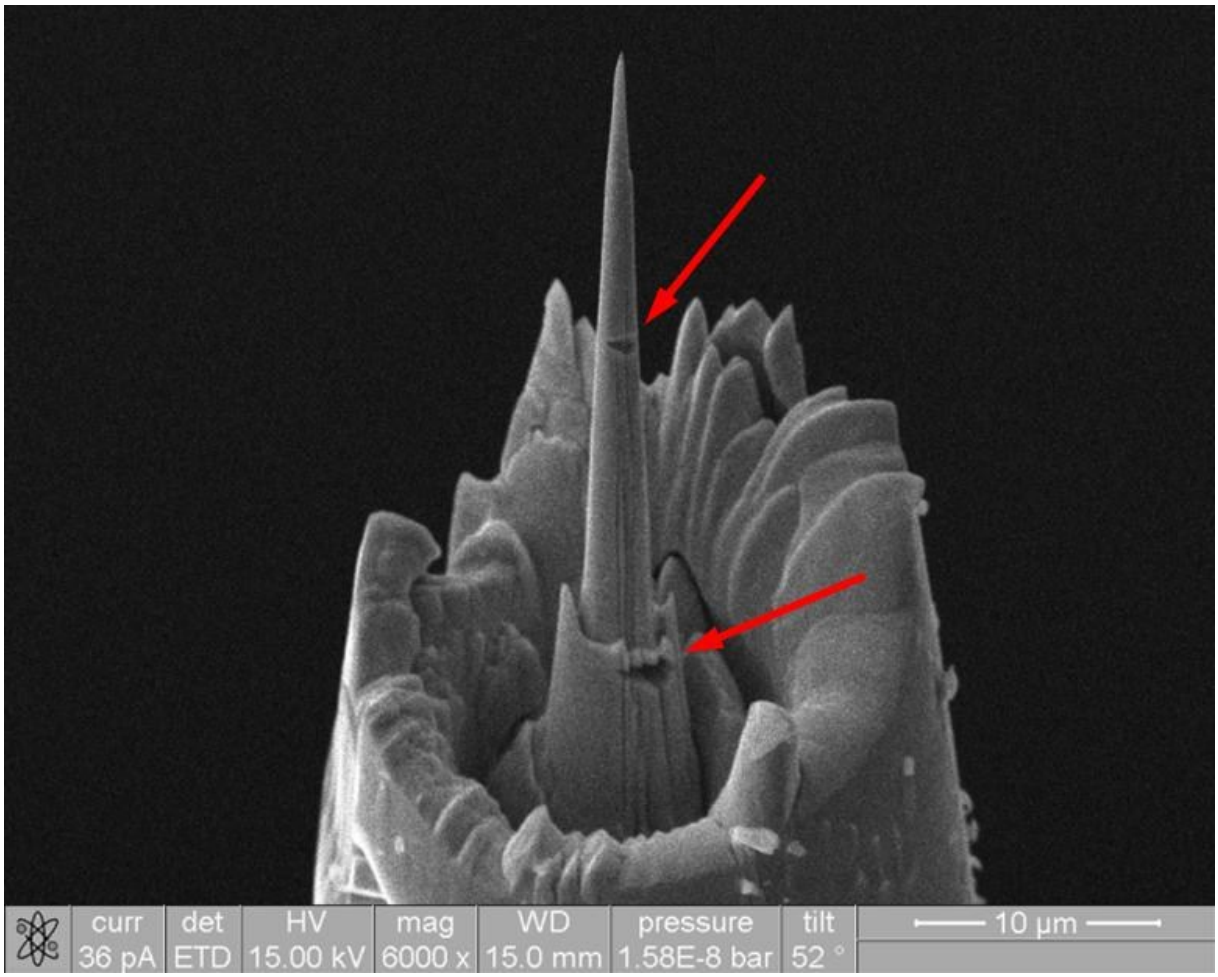

Figure 3.7: SEM image of an atom probe specimen from the as-sintered condition (SC). Two exposed pores in short distance of each other are marked by red arrows.

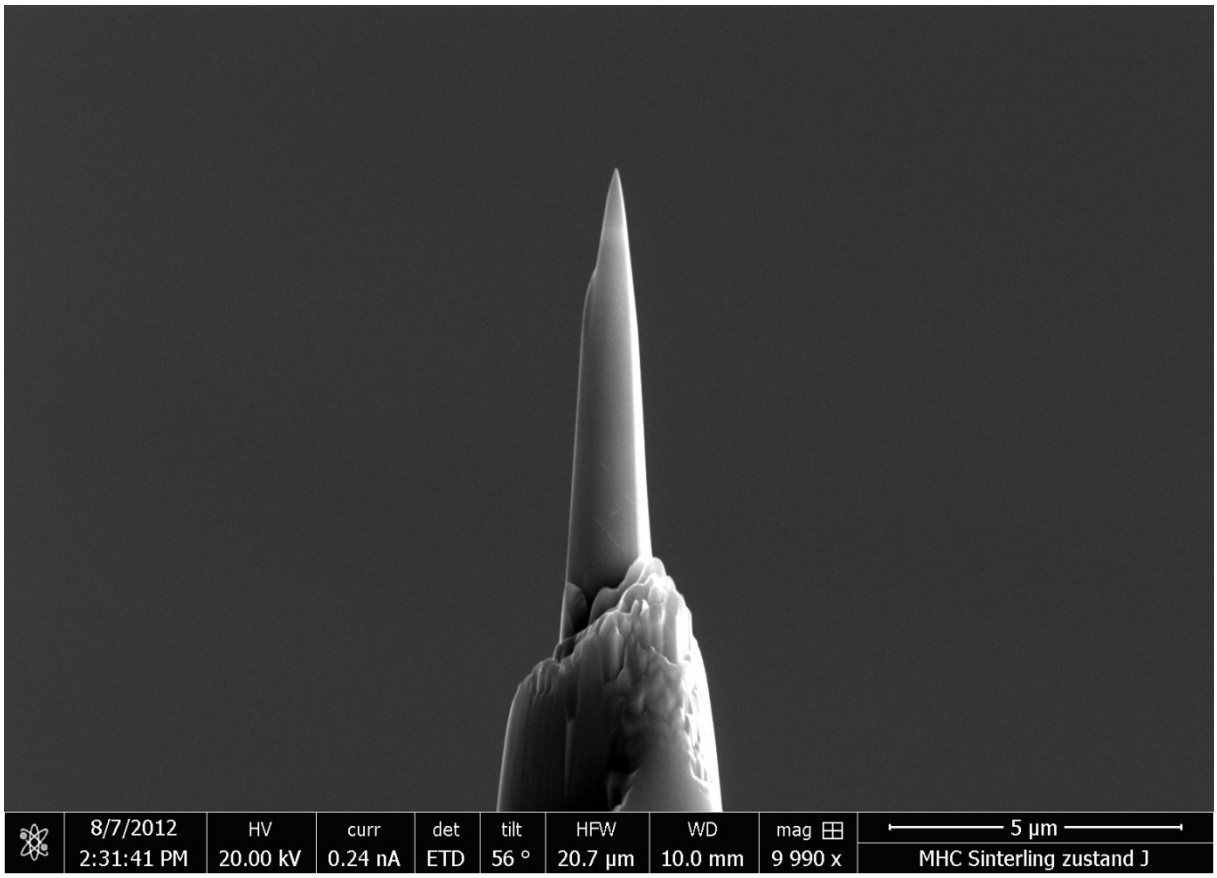

Figure 3.8: SEM image of a well prepared sample of the sintered condition at point j (SCj).

The reconstruction as well as the analysis of the measured specimens were done with the software IVAS^{TM} 3.6.0 from CAMECA [32].

In order to decide if there was a cluster formation of elements given in the reconstructed tips frequency distribution analysis were applied to the APT data sets. This is a grid based technique where the 3D data are partitioned into a number, *N*, of discrete rectangular blocks. Each block contains an equal number of atoms, n_b. In this thesis a bin size n_b of 100 atoms (ions) was chosen. The number of solute ions occurring in each block is counted. The frequency, at which the solute ions occur, can then be compared to the corresponding binomial distribution, i.e., the theoretical distribution of solute ions expected, assuming they occur randomly throughout the data set. A shift in the solute distribution away from the binomial is indicative for present microstructural phenomena in the sample. The magnitude of this deviation from randomness in solute atom distribution can be quantified by applying a χ^2 measure to the analysis which is shown by Equation 3.1, where *f(n)* is the binomial distribution and *e(n)* is the number of blocks containing *n* solute atoms [33].

$$\chi^2 = \sum_{n=0}^{n_b} \frac{(e(n)-f(n))^2}{f(n)} \qquad 3.1$$

Significance is often applied to the measurement by comparing χ^2 to the corresponding theoretical chi-square distribution. The most serious limitation of the χ^2 test for significance is a dependence on sample size. The value of χ^2 will increase with an increasing number N of blocks sampled. With an increasing sample size, significance testing is increasingly likely to reject the null hypothesis. It would not be appropriate to apply χ^2 statistics on varying data set sizes for a direct comparison of solute segregation. Therefore the Pearson coefficient μ, which can be seen in Equation 3.2, was introduced to effectively normalize the N dependence of χ^2 [33].

$$\mu = \sqrt{\frac{\chi^2}{N+\chi^2}} \qquad 3.2$$

This results in a value μ which is independent of the sample size and it is between 0 and 1, where 0 indicates a random distribution and 1 indicates a complete association in the occurrence of the solute atoms [33]. In this thesis it was considered as a relevant clustering when the μ value of the sample was in a percentage range.

Clusters can be separated manually from the bulk with the method Isosurface of IVAS^{TM}. Isosurfaces are surfaces drawn into the 3D display at a threshold value set by the user for the specified ions. They are the first step in creating interfaces and volume rendering. The included volume can then be examined separately [32].

The selection of solute-rich regions was performed via cluster search by connecting solute atoms which lie within a fixed distance (d_s), and counting them as clusters above a certain minimum number of solute atoms (N_{min}). Other atoms within some distance L greater than d_s are taken to belong to the cluster. However, this results in the inclusion of a shell of matrix atoms, which must be removed through an erosion step, to define the final cluster. Data filtered in this way can be used for subsequent quantification of parameters such as size, shape, composition, number density and volume fraction with better accuracy than by manual selection [34].

The visualization of the chemical compositions was done with a 1D or 2D concentration plot. In the 1D concentration plot an average element concentration is plotted along the axis of a certain volume element. The 2D concentration plot projects the average concentration of elements in a volume along an area. Red areas indicate higher concentrations of the chosen elements. In both plots a step size of 1.5 nm along the volume axis as well as a distance between the sample planes of 1.5 nm was chosen for this thesis [32].

3.7 X-Ray diffraction (XRD)

X-Ray diffraction experiments were conducted with a Brucker D8 Advance in a Bragg-Brentano configuration ($\theta/2\theta$-mode) from 25° to 80°. The step size was 0.02° using Cu-K_α radiation with λ_{Cu}=1.54056 Å. The samples were prepared like the specimens for SEM microstructural investigations, which is described in section 3.4. For the interpretation of the XRD patterns, values from databases and literature were used [19,35–38].

3.8 Chemical analysis

In order to define the C content of the as-sintered condition, a combustion analysis (CA) with a LECO CS-230 was done at Plansee SE. Oxygen, nitrogen and hydrogen contents were analyzed by carrier gas hot extraction (CGHE) with a LECO TCH 600. The contents of metals like tungsten, zirconium and most important Hf were measured by inductively coupled plasma optical emission spectroscopy (ICP-OS) with a Thermo iCAP 6500 DUO.

4 THERMO-MECHANICAL PROCESS AND SAMPLING PLAN

4.1 Thermo-mechanically processing of MHC samples

Figure 4.1 illustrates the temperature- time sequence for the thermo-mechanical treatment of the MHC alloy. This process is divided into two main parts. In the first part the samples are heated up to temperature T_B, deformed at point d with a true strain of φ=-0.27 and a temperature T_d. Afterwards, the samples were held at temperature T_E. In the second part a heat treatment was carried out at T_G in order to recrystallize the samples and relief stresses from deformation. The points f', g' and h' label the conditions where the specimens for further investigations were quenched with nitrogen from the points f, g and h to room temperature (T_R).

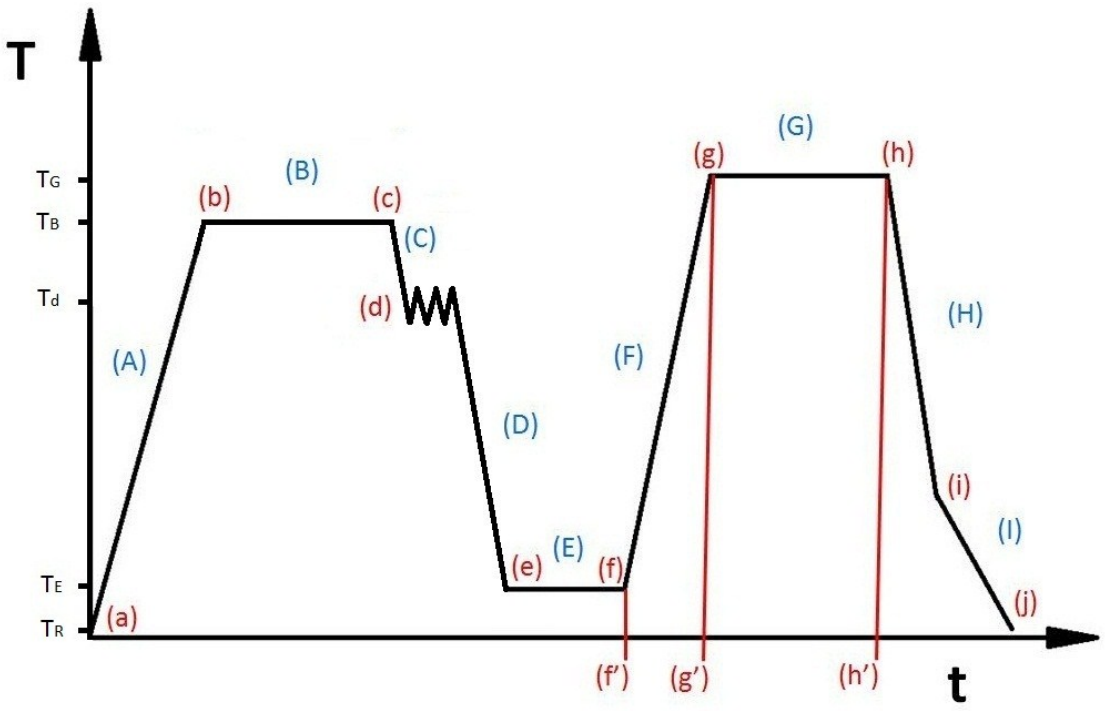

Figure 4.1: Thermo-mechanically processing of MHC samples.

4.2 Sampling plan

At the beginning of this investigation the sintered MHC was characterized regarding to its microstructure and composition. Next the final condition j was investigated with and without deformation with emphasis on TEM studies and APT measurements. Derived from the gained knowledge condition f' was investigated with focus on the development of the microstructure after deformation. Finally, the conditions g' and h' were examined regarding the formation of secondary precipitates. Additionally, a long term heat treatment experiment was carried out. The sintered samples were heated up in 10 min to 1600°C and held at this temperature for 10 h (SC10h1600C). Then they were quenched with nitrogen to T_R. The aim of this experiment was to investigate microstructural and compositional differences compared to the SC. Table 4.1 illustrates the labeling of the samples as well as the conducted investigation methods for the mentioned samples. This is consistent with the labeling in the thermo-mechanical process from Figure 4.1.

Table 4.1: Labeling of samples and conducted investigation methods.

Specimen name	Deformation φ	Quenched with N_2 to T_R	TEM	APT	OLM	SEM	XRD
SC = as-sintered condition	-	-	X	X 60 K	X	-	-
Cj = condition at point j	0.27	-	X	X 60 K	X	-	X
SCj = sintered condition at point j without deformation at point d	-	-	X	X 60 K	X	-	X
Cf' = condition at point f'	0.27	from T_E	X	X 90 K	X	-	X
Cg' = condition at point g'	0.27	from T_G	X	X 90 K	X	X	X
Ch' = condition at point h'	0.27	from T_G	X	-	X	-	X
SC10h1600C = long term experiment with sintered condition at 1600°C for 10 h	-	from 1600°C	X	X 60 K	X	-	X

5 RESULTS

5.1 Characterization of the as-sintered condition (SC)

The mixture of the MHC powder was uniaxial pressed and sintered at a maximum temperature of 2200°C in H_2 environment. The relative density of the sintered material was measured by buoyancy method with approximately 96 %. Samples were only taken from areas sufficiently away from surface regions, where chemistry and microstructure may differ. Table 5.1 exhibits the chemical composition of the SC for the most important elements which are encountered in MHC.

Table 5.1: Chemical composition of the SC in wt.% and at.%. The data was provided by Plansee SE.

Element	Testing procedure (see list of abbreviations)	Content	
		[wt.%]	[at.%]
C	CA	0.1068	0.8488
H	CGHE	0.0003	0.0284
N	CGHE	< 0.0005	-
O	CGHE	0.0576	0.3437
Hf	ICP-OS	1.2050	0.6445
Zr	ICP-OS	0.0024	0.0025
W	ICP-OS	0.0176	0.0091

The sample material displayed an overall C and Hf content of ~0.85 at.% and ~0.64 at.%, respectively. It can be seen that there was an enhanced oxygen content of ~0.34 at.% in the sample which is a result of the powder metallurgically processing. The most important accompanying element in MHC is tungsten with ~0.009 at.%. There were also traces of zirconium and hydrogen in the samples but no nitrogen was found.

Figure 5.1 shows an OLM micrograph of the SC which was etched with Hasson etchant [22]. Within the matrix primary Hf- rich carbides are distributed homogeneously. They appear black and have a size of ~1 µm. Hf- oxide particles are either inside the grain or at grain boundaries. They have a greyish appearance and occur usually in combination with Mo_2C, which is white and located mainly at grain boundaries. The average grain diameter was determined with the linear-intercept method as 99 µm. Residual pores are predominantly located within the grains and have a typical diameter of ~5 µm [17].

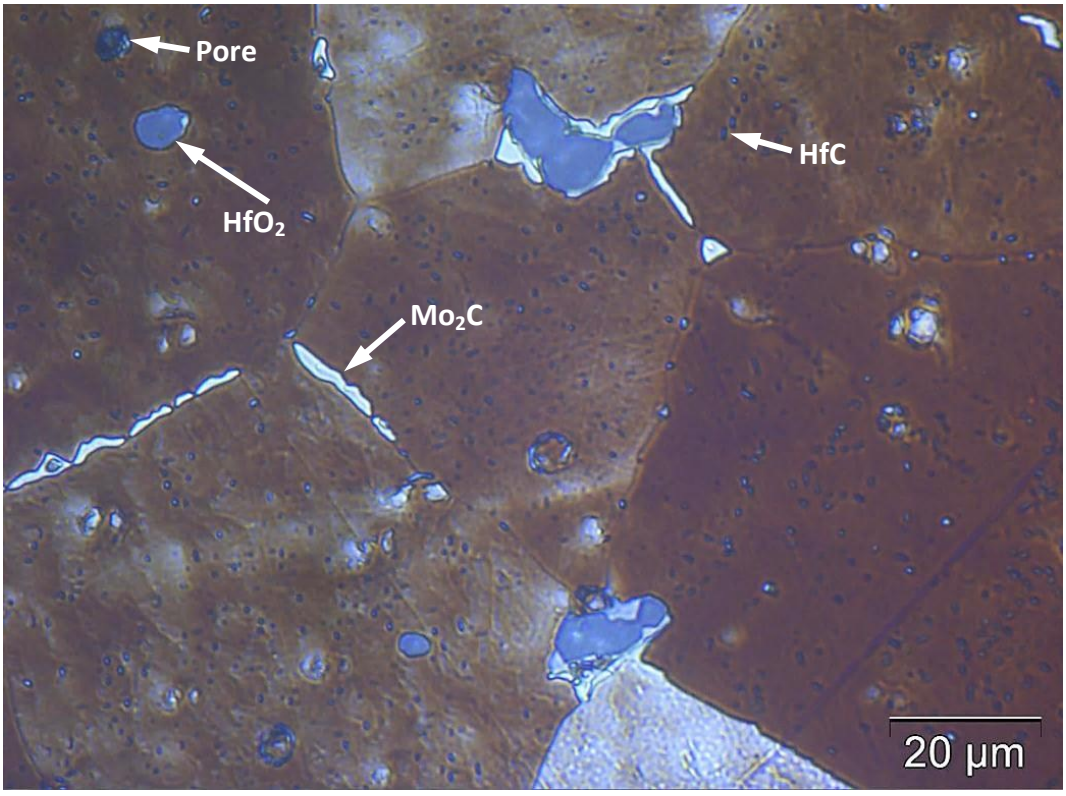

Figure 5.1: OLM micrograph of the SC. Etched with Hasson etchant [17,22].

5.1.1 TEM investigation of the SC

Figure 5.2 (a) and Figure 5.2 (b) show TEM micrographs of the SC. It was confirmed by EDS measurements that primary Hf- rich carbides are embedded within the matrix and it can be seen in the images that they have a typical length of ~1µm. It was observable by tilting of the samples that these primary carbides have a plate-like shape and are perpendicular orientated to each other [17]. Those primary particles are positioned face-on or edge-on in the matrix and were found in all conditions throughout the thermo-mechanical process.

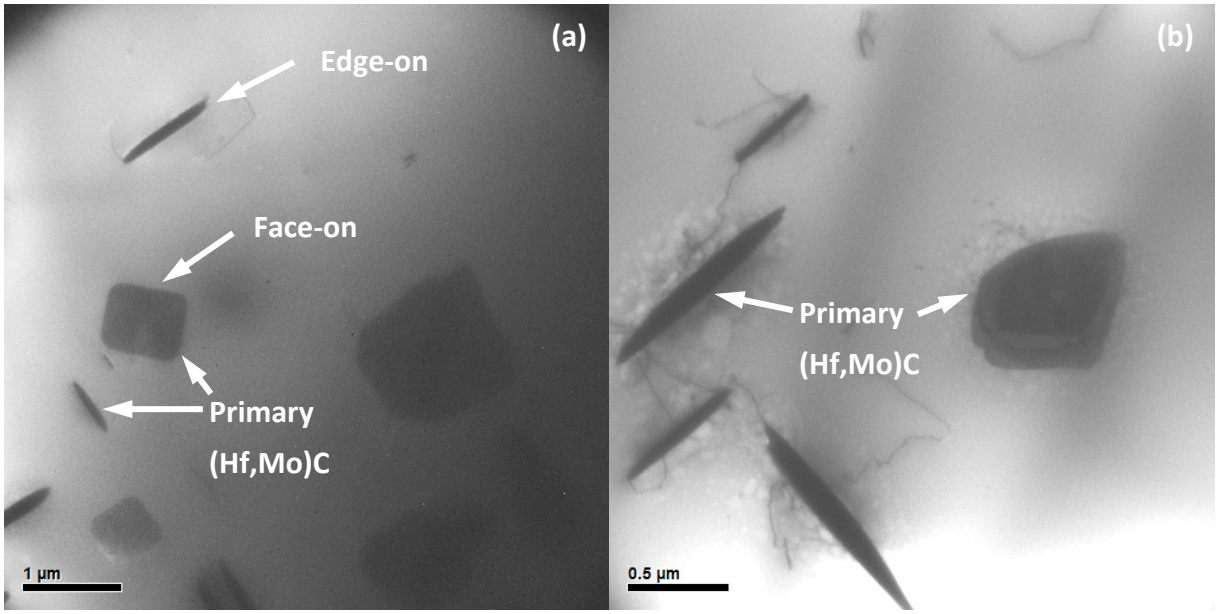

Figure 5.2: TEM micrographs of the SC. (a) Matrix with primary (Hf,Mo)C (edge-on and face-on). (b) Different spot with dislocations next to the primary Hf- rich carbides.

5.1.2 Atom probe tomography of the SC

Figure 5.3 (a) shows an example of a 3D elemental map of Hf (blue atoms) and C (red atoms) from the bulk of an atom probe specimen from the SC. The point size of the C atoms was increased from 1 to 1.5 for a better visualization of the C distribution. The visual inspection of the 3D elemental map leads to the assumption that Hf is homogeneously distributed within the bulk of the SC. This is confirmed by Figure 5.3 (b) which shows a 1D concentration profile along the z axis of the reconstructed tip volume and by low μ values which are illustrated in Table 5.2 (μ value see section 3.6). Table 5.2 also shows the average bulk composition of two measured specimens of the SC. The average Hf content in the matrix after sintering is ~0.12 at.% which is ~0.53 at.% lower than in the overall chemical analysis. The average tungsten content is about 0.0074 at.%. This is in good agreement with the ICP-OS data. An important aspect is that there is nearly no C in solid solution in the matrix (compare to overall chemical analysis in section 5.1). The low gallium content reflects the quality of the FIB preparation.

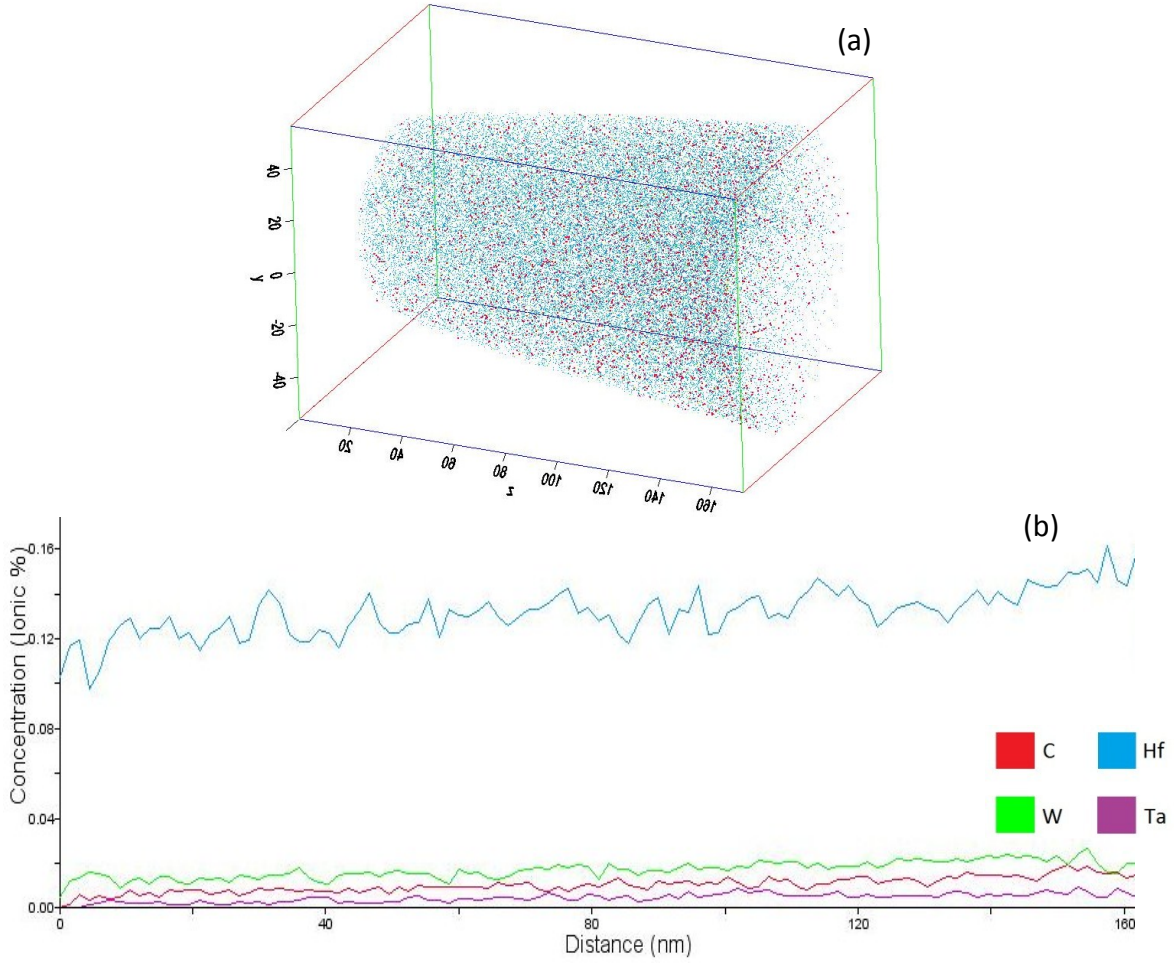

Figure 5.3: (a) Example of a 3D elemental map of Hf and C in a specimen of the SC. (b) 1D concentration plot along the z axis of the tip volume in (a).

Table 5.2: Average bulk composition of two measured atom probe tips of the SC.

Element	Content [at.%]	Content [wt.%]	μ [-]	Element	Content [at.%]	Content [wt.%]	μ [-]
Mo	balance	balance	-	**Hf**	0.1240	0.2304	0.0052
C	0.0017	0.0002	0.0035	**W**	0.0074	0.0142	0.0007
O	0.0034	0.0005	0.0029	**Ga**	0.0080	0.0058	0.0013
Ta	0.0027	0.0051	0.0001				

5.2 Microstructure after deformation- condition f' (Cf')

The samples were heated up, held at temperature T_B, cooled to temperature T_d and deformed at this temperature with a deformation degree of φ=0.27. Then, they were slowly cooled and held at temperature T_E. When point f of the thermo-mechanical process was reached the samples were quenched to point f' (see sections 4.1 and 4.2). Afterwards TEM and APT investigations were conducted in order to reveal the microstructural and compositional effects within the samples.

5.2.1 TEM investigations of Cf'

The microstructure of Cf', which can be seen in Figure 5.4 (a) and Figure 5.4 (b), shows a subgrain structure with a subgrain size of ~1 µm. This subgrain structure formed during or after the deformation due to recovery processes. Most of the dislocations are located in the subgrain boundaries but a few still remain inside the subgrains. There are no obvious secondary precipitates visible. Figure 5.5 (a) and Figure 5.5 (b) show such subgrains in detail and Figure 5.5 (c) and Figure 5.5 (d) display indications of precipitates in the early stages of precipitation. They are marked by a red arrow. However, it was not possible to clearly identify those spots due to limitations in resolution of the used TEM.

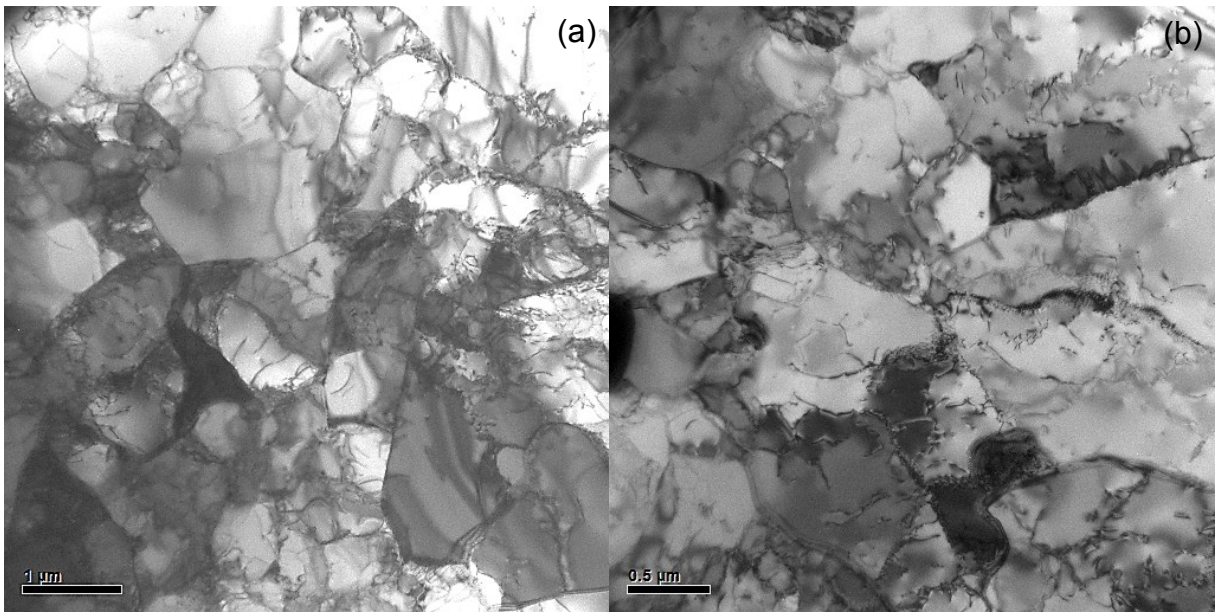

Figure 5.4: TEM micrographs of the subgrain structure from Cf' at different magnifications. (a) 15000x. (b) 25000x.

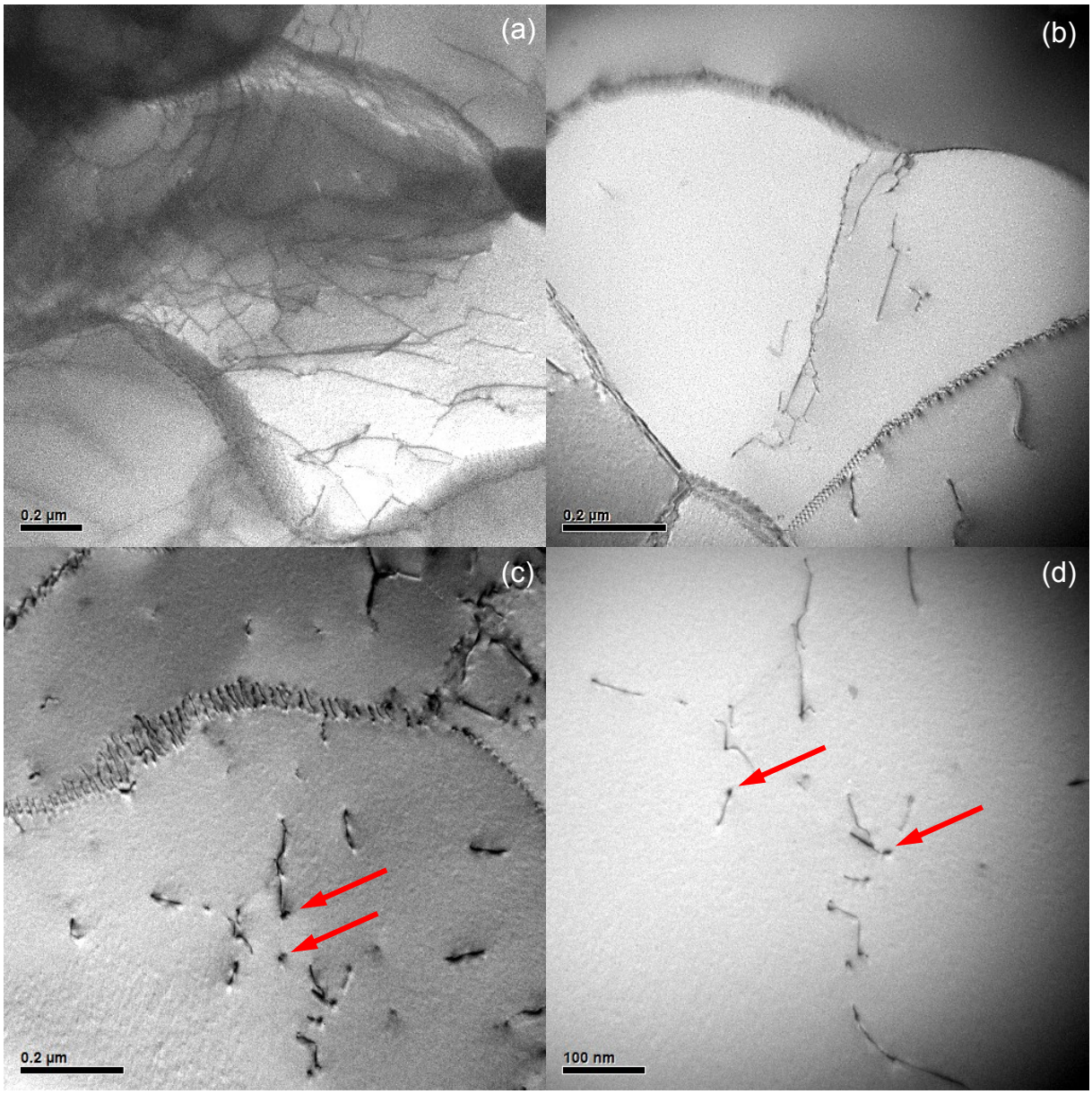

Figure 5.5: TEM micrographs of the subgrain structure from Cf' at different magnifications. Subgrain in detail with a few dislocations and no secondary precipitates in it at a magnification of (a) 53000x and (b) 88000x. Possible secondary precipitates at early stages of precipitation at a magnification of (c) 88000x and (d) 140000x.

5.2.2 Atom probe tomography of Cf'

Figure 5.6 (a) shows a 3D elemental map of Hf (blue atoms) and C (red atoms) in a specimen from Cf'. It can be seen that there are clusters of these elements within the bulk of the tip. The Hf and C distributions are shown separately in Figure 5.6 (b) and Figure 5.6 (c) and it can be seen that the position of the Hf and C clusters are overlapping. Table 5.3 illustrates the chemical composition of the bulk of the measured specimen as well as the μ values which display the distribution of these elements (μ value see section 3.6). It can be seen that there is a high deviation from 0 of the μ values for Hf and C which confirm a cluster formation of these elements. All the other elements are in the typical ranges as for the SC.

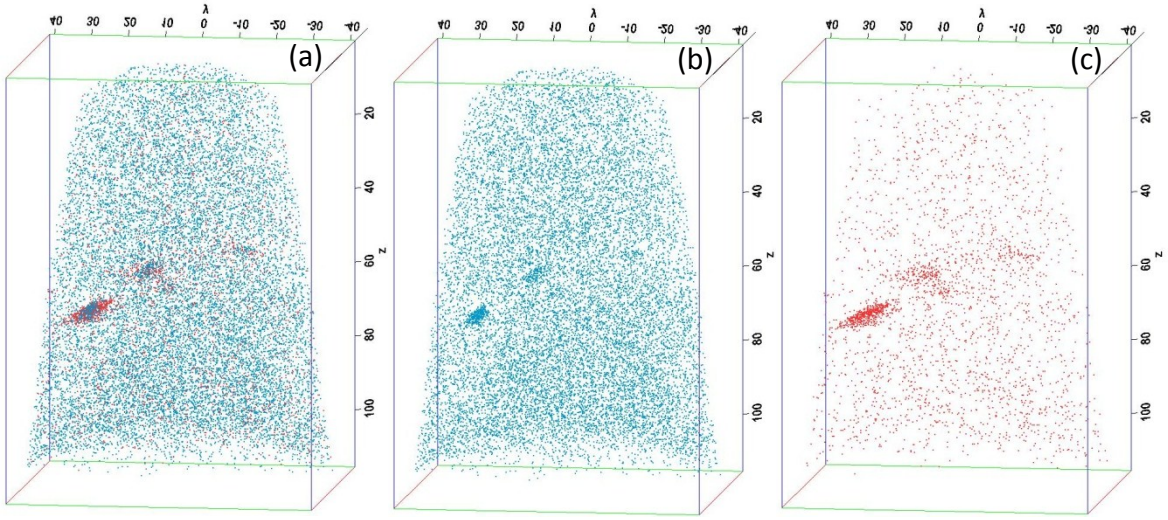

Figure 5.6: 3D elemental map of a specimen from Cf'. (a) Hf and C distribution. (b) Hf distribution. (c) C distribution.

Table 5.3: Bulk composition of the specimen from Figure 5.6. The elevated μ values indicate a clustering of Hf and C.

Element	Content		μ [-]
	[at.%]	[wt.%]	
Mo	balance	balance	-
Hf	0.1196	0.2223	0.0238
C	0.0078	0.0010	0.0856
O	0.0025	0.0004	0.0001
W	0.0039	0.0075	0.0010
Ta	0.0003	0.0006	0.0001
Ga	0.0088	0.0064	0.0001

In order to get an impression of the Hf and C content in these clusters, a region of interest (ROI) was positioned through one cluster. This is shown in Figure 5.7 (a) and Figure 5.7 (b). Figure 5.7 (c) displays a 1D concentration profile along the z axis of this ROI. It can be seen that the Hf and C content increases when the ROI penetrates the cluster and that there is nearly no C in the bulk of Cf'.

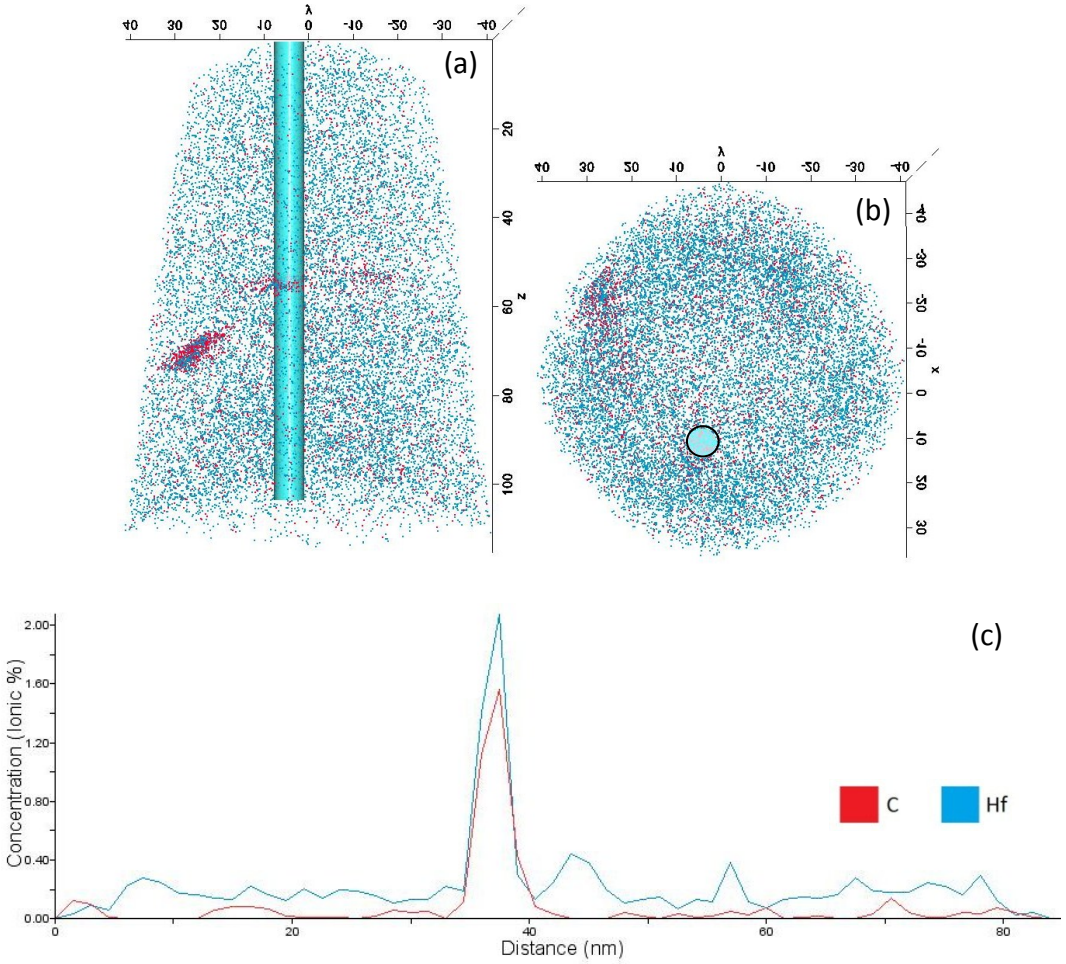

Figure 5.7: (a) Elevation of the 3D elemental map of a specimen from Cf' with a ROI positioned through a cluster. (b) ROI position in the top view of this specimen. (c) 1D concentration plot along the z axis of this ROI.

For a detailed analysis of the cluster, a cluster search for Hf and C was conducted (cluster search algorithm is defined in section 3.6). The used parameters for the cluster search were a fixed distance d_s= 1.40 nm, a minimum number of atoms in the cluster N_{min}= 14 and a distance parameter L= 1.40 nm. As shown in the 3D elemental map in Figure 5.8, four clusters were found within the bulk of the measured tip from Cf' and separated. Table 5.4 shows the Hf and C contents of these four clusters. The number of atoms in each cluster was

corrected by the detector efficiency of 37% [28]. It can be seen that the values for Hf and C are nearly equal in each cluster. The highest values, but simultaneously the lowest amount of atoms, were found in cluster 3 with 8.42 at.% Hf and 8.40 at.% C. The cluster search and the 1D concentration plot reveal that these clusters have no stoichiometric composition.

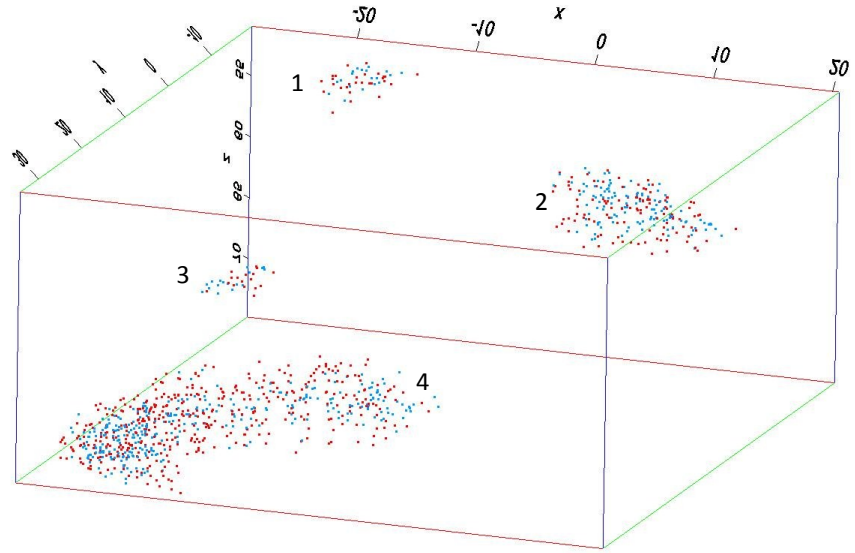

Figure 5.8: 3D elemental map of Hf and C of the four clusters of the specimen from Cf' found by the cluster search algorithm.

Table 5.4: Hf and C contents of the clusters in specimen from Cf'.

Cluster No.	Atoms in cluster [-]	Hf [at.%]	C [at.%]
1	130	4.73	6.08
2	629	5.59	6.65
3	92	8.42	8.40
4	1981	4.41	5.99

5.3 Microstructure after deformation and heat treatment

After deformation and different heat treatments, the conditions g' (Cg'), h' (Ch') and j (Cj) of the thermo-mechanical process (see sections 4.1 and 4.2) were investigated with SEM, TEM and APT in order to study the development of secondary precipitates and compositional effects.

5.3.1 SEM investigation of Cg'

Figure 5.9 shows a SEM micrograph (backscatter image with a high current) of Cg' with a distinct subgrain structure. The typical subgrain size is approximately 1 µm. Due to TEM investigations it is known that the primary Hf- rich carbides have a plate-like shape [17]. They can be seen as white phases in the SEM image and the ones which are orientated perpendicular to each other appear to be edge-on [15]. A grain boundary is visible in the center of the image. The different orientations of the two grains can be observed indirectly through the different orientations of the primary (Hf,Mo)C in the two grains (shown with black crosses). Due to restrictions in resolution, it was not possible to detect secondary precipitates with SEM. Therefore this investigation method was not conducted for any other condition of the TMP.

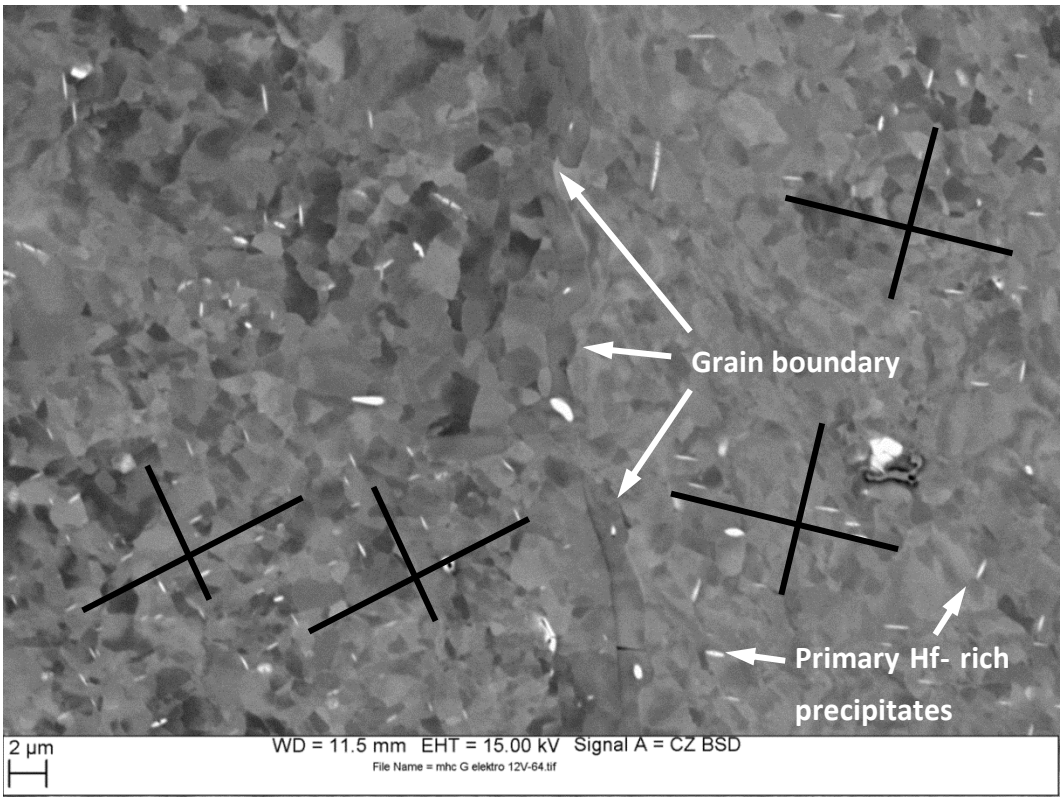

Figure 5.9: SEM image of the subgrain structure of Cg'.

5.3.2 TEM investigations

5.3.2.1 Condition g' (Cg')

Figure 5.10 (a) shows a TEM micrograph of Cg' with a distinct subgrain structure like in Cf'. There are already small secondary precipitates with a size of ~ 5– 25 nm existing, which can be seen in Figure 5.10 (b) as well as in Figure 5.11 (a) and Figure 5.11 (b) in detail. These small particles are preferentially located at dislocations and dislocation networks. Due to the small size of the secondary precipitates at this stage of the thermo-mechanical process, it was not possible to determine the exact shape of these particles. However, TEM investigations of Cg' indicate that the beginning of the precipitation reaction is in the heating period of section F shortly before point g at already elevated temperatures.

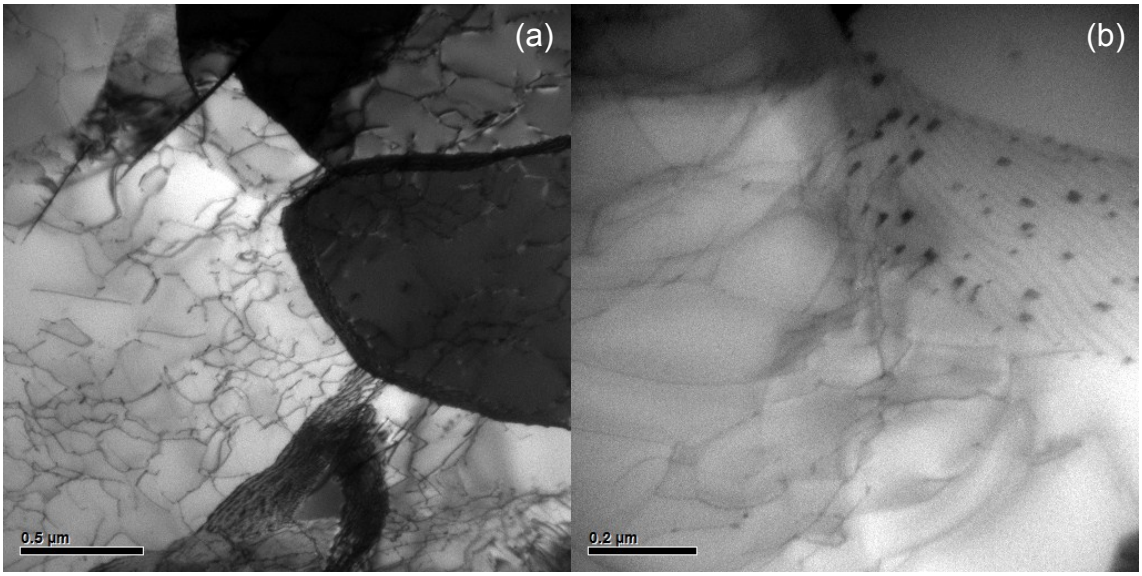

Figure 5.10: TEM micrographs of Cg'. (a) Subgrain structure. (b) Detail of a dislocation network with secondary precipitates in it.

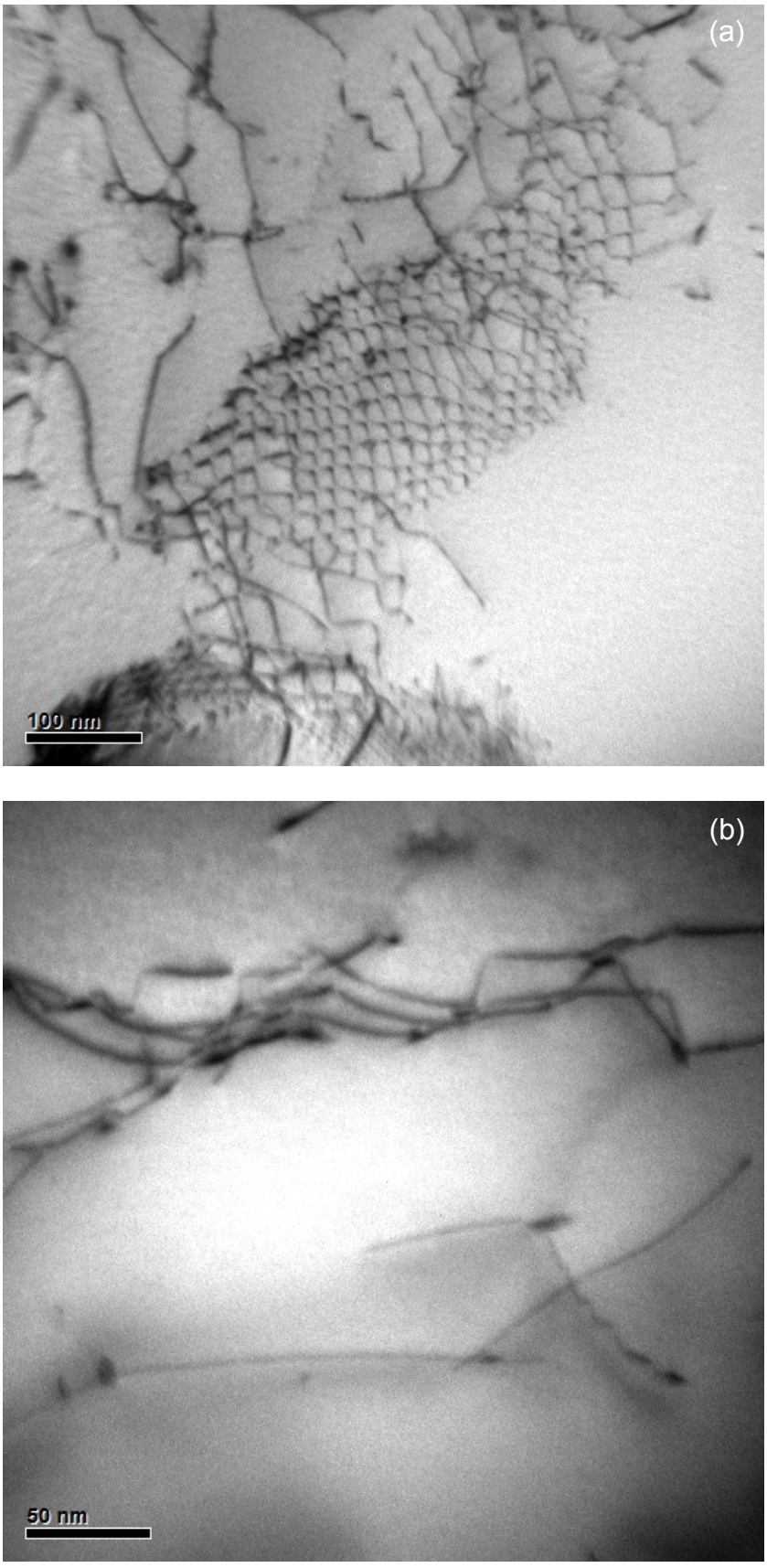

Figure 5.11: TEM Micrographs of Cg'. Secondary precipitates on dislocations at a magnification of (a) 140000x and (b) 300000x.

5.3.2.2 Condition h' (Ch')

Figure 5.12 shows a TEM micrograph of a partially recrystallized microstructure with secondary precipitates. These precipitates appear in the subgrain structure as well as in the recrystallized areas and possess a typical length of ~ 25- 50 nm and a thickness of ~ 5 nm. As for Cg' they are preferentially located at dislocations and dislocation networks. Figure 5.13 (a) shows in comparison to Figure 5.13 (b) that there are areas in the subgrain structure where no secondary precipitates are embedded in the matrix. This points out that their distribution is not uniform. Due to tilting it was observable that the secondary precipitates have like the primary Hf- rich carbides a plate-like shape [17].

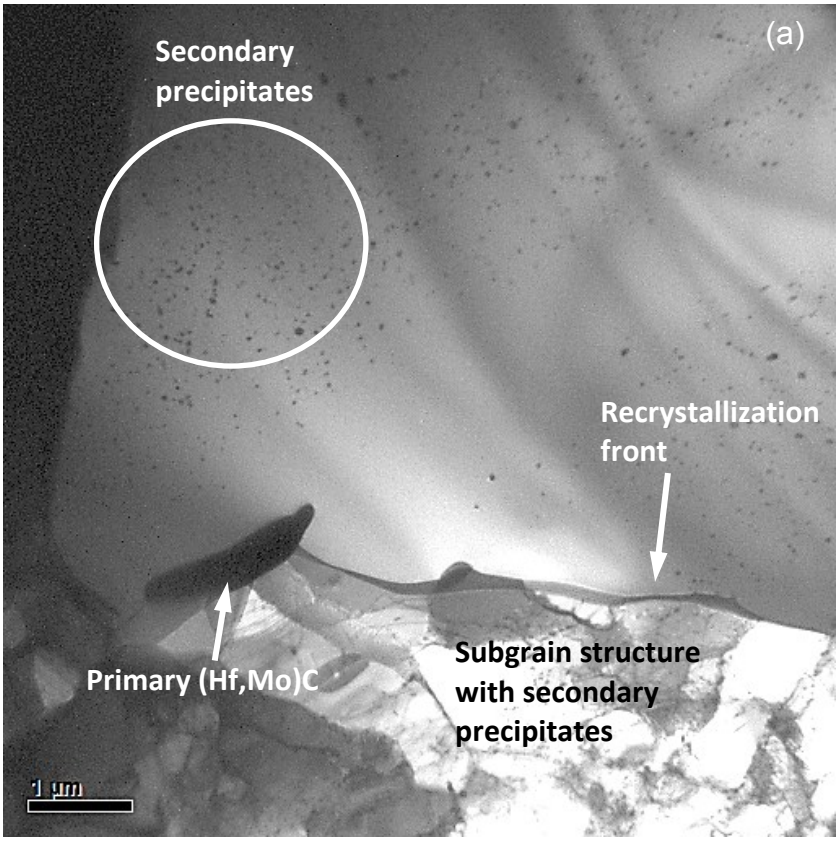

Figure 5.12: TEM micrograph of Ch'. Partially recrystallized microstructure with secondary precipitates in recrystallized areas and in subgrain structure.

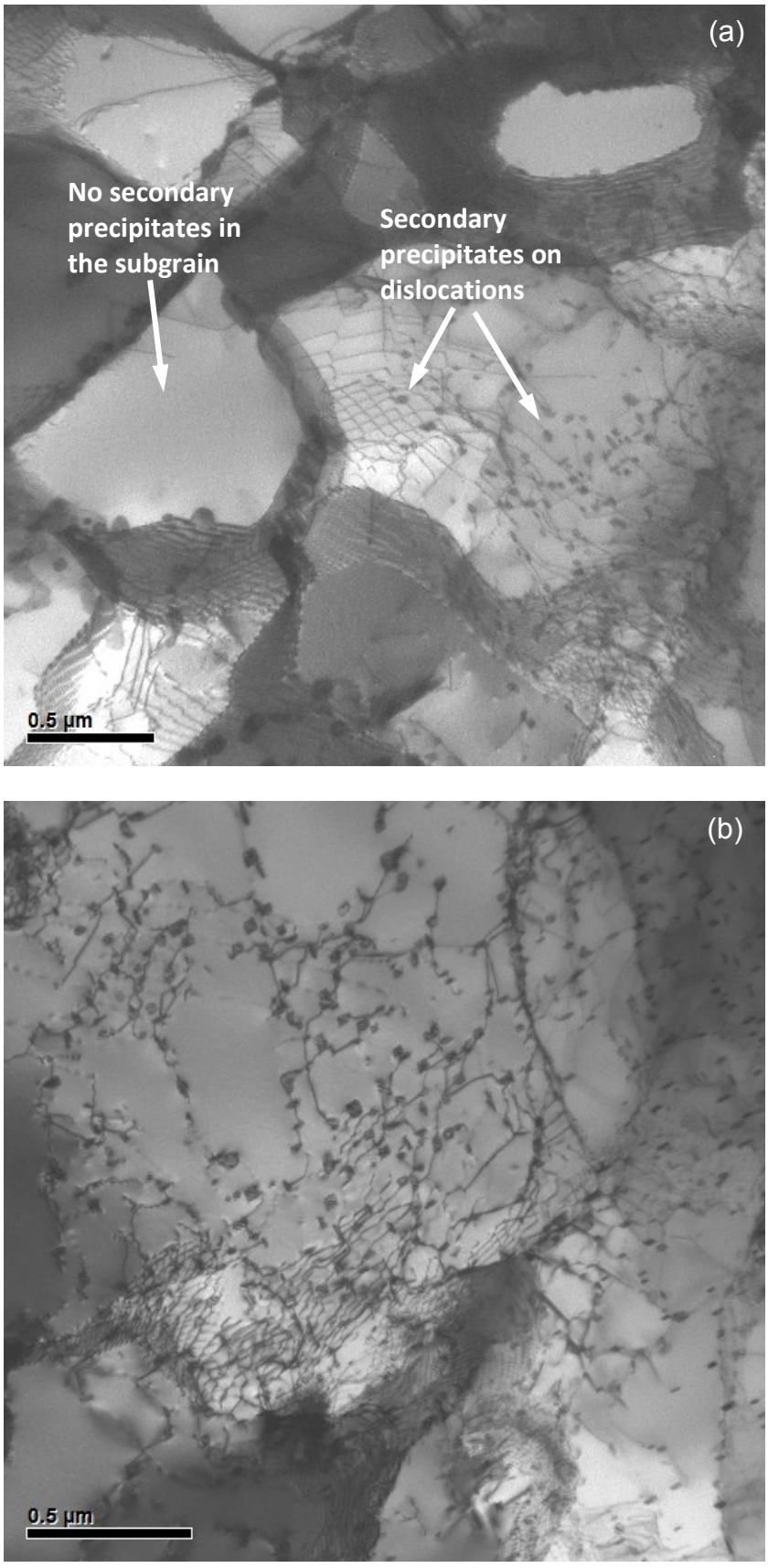

Figure 5.13: TEM micrographs of Ch'. (a) Area with subgrain structure with and without secondary precipitates. (b) Area with uniform distributed secondary precipitates.

Additionally, the orientation relationship between matrix and secondary precipitates as well as the interface of the matrix to the secondary precipitates was investigated with a high resolution TEM FEI TECNAI F20. For this all TEM micrographs were taken in [001] zone axis of the matrix. Maps of Kikuchi lines were used for the orientation during the diffraction experiments in order to find the [001] zone axis. Afterwards, the adjustment was verified with a standard diffraction pattern for the [001] direction in a bcc crystal [39].

A red circle in Figure 5.14 (a) marks the matrix where selected area diffraction (SAD) was recorded, shown in Figure 5.14 (b). As described in the standard diffraction pattern for the [001] direction in a bcc crystal, the [001] zone axis of the matrix is successfully adjusted and the ratio *L/M* is ~1.41 which is the case in Figure 5.14 (b) [39]. The lattice parameter *a* of the matrix was calculated from this diffraction pattern and is 3.160 Å. This is in good agreement with the literature value of Mo containing 0.3 at.% Hf which is 3.1488 Å [40].

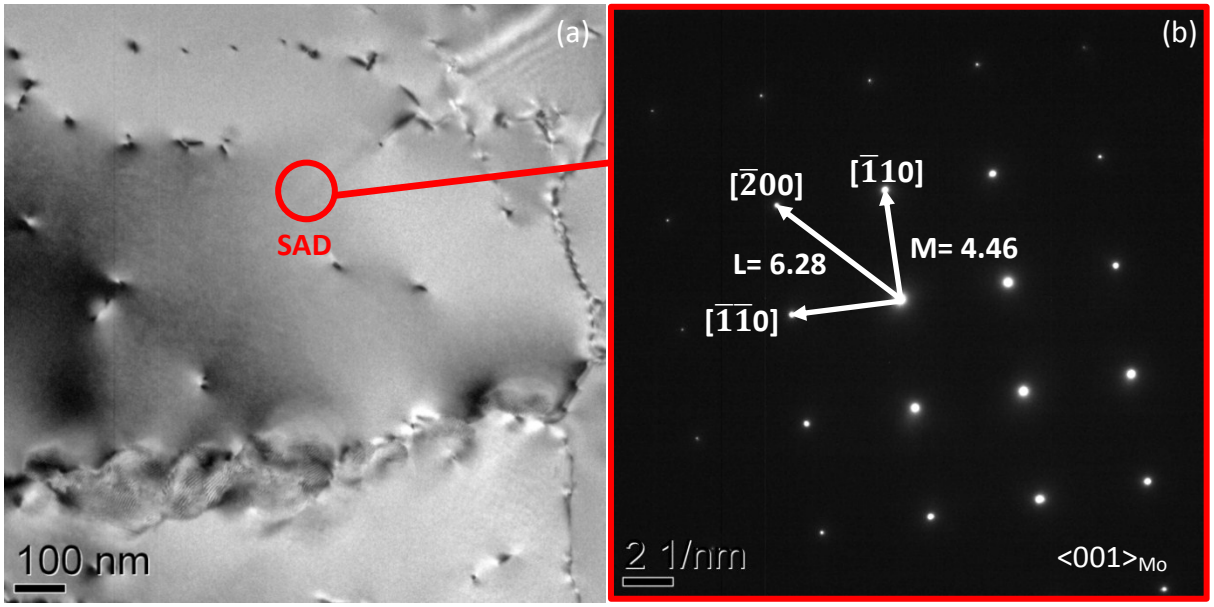

Figure 5.14: TEM micrographs of Cj. (a) Matrix. The red circle marks the area of SAD. (b) SAD pattern of the bcc matrix.

With the matrix adjusted in [001] zone axis, shown in Figure 5.14 (a) and Figure 5.14 (b), SAD was recorded at an area with secondary precipitates embedded in the matrix as shown in Figure 5.15 (a). The diffraction pattern in Figure 5.15 (b) shows, as expected, the typical reflections for the bcc matrix like in Figure 5.14 (b), plus the reflections of the secondary precipitates, which are not very intensive in this case. The reflections of the precipitates indicate a fcc crystal structure. This is confirmed by a standard diffraction pattern for a fcc

crystal and it can be observed that the precipitate is orientated in [110] direction. For this, the ratio of *L/M* should be 1.155 [39] which is in this case 1.157. The calculated lattice parameter of the secondary precipitate is determined to be 4.601 Å which is in good agreement with the lattice parameter a = 4.6376 Å from literature [35].

Overall, this experiment confirms the orientation relationship between the matrix and the secondary precipitates as reported in literature by Ryan [15]:

$$\{100\}_{Mo} \,//\, \{100\}_{ppt}$$

$$<100>_{Mo} \,//\, <110>_{ppt}$$

$$<110>_{Mo} \,//\, <100>_{ppt}$$

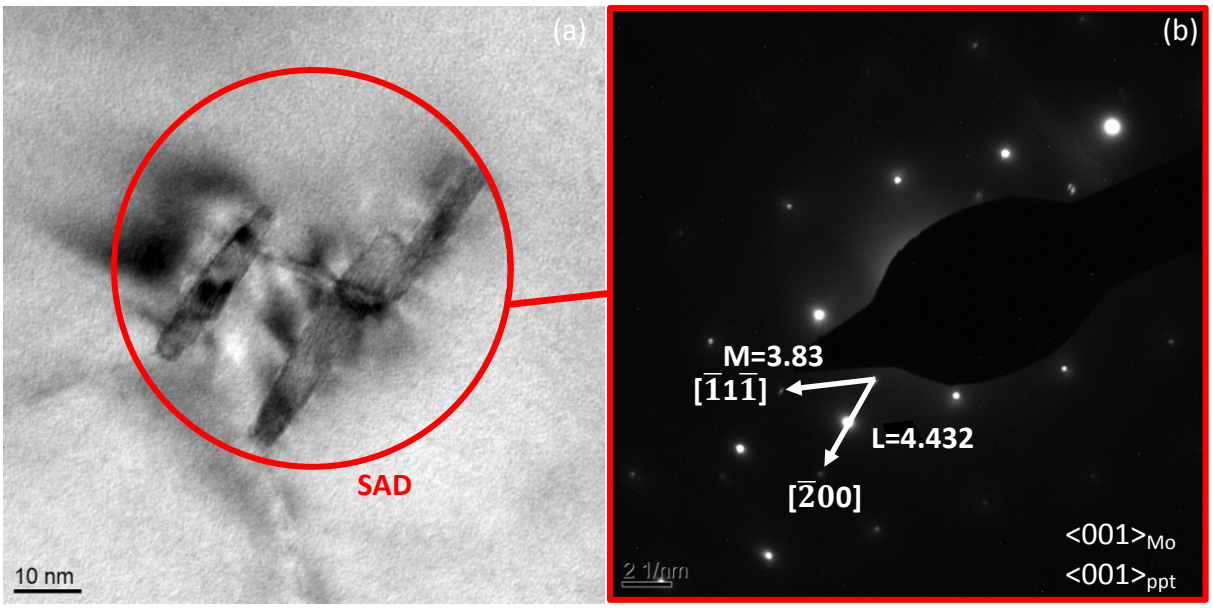

Figure 5.15: TEM micrographs of Ch'. (a) Matrix in [001] zone axis with secondary edge-on precipitates. The red circle marks the spot where the selected area diffraction was recorded. (b) Diffraction pattern with reflections of the matrix and the precipitates. The arrows mark the reflections for the secondary precipitates.

The interface between the matrix and the secondary precipitates was studied in Ch' in an area without recrystallization. The matrix was adjusted in [001] zone axis. Figure 5.16 (a) and Figure 5.16 (b) show that the area at the edge of the plate-like precipitate, marked by a white ellipse, is strongly disturbed. This indicates an incoherent interface to the matrix along the lateral area of the plate-like secondary precipitate. The green line shows the <110> direction of the matrix and the red line the <110> direction of the precipitate. These two

lines always include a 45° angle which also can be seen in the lattice model from Ryan in Figure 5.18 (b) [15]. With the help of an additional small lattice model in Figure 5.17 (b), where the green dots symbolize the matrix atoms and the red dots the atoms of the precipitate, it can be observed that the <110> direction of the matrix is parallel to <100> directions of the precipitate.

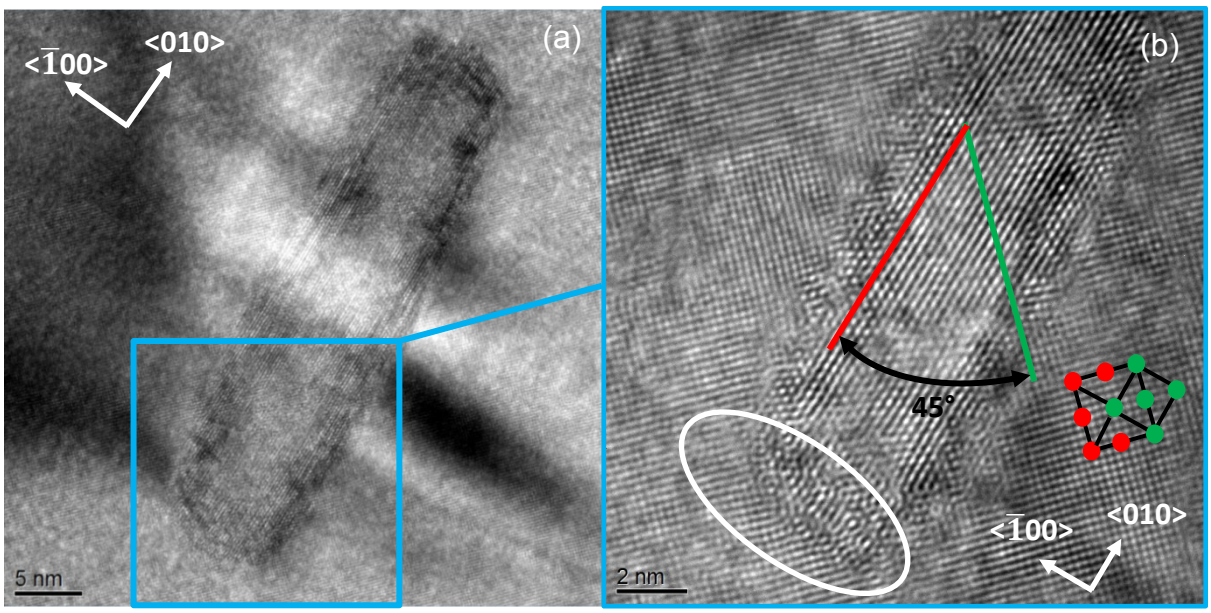

Figure 5.16: TEM micrographs of Ch'. (a) Interface matrix (green) to edge-on precipitate (red). (b) Detail of a. There are clearly visible disturbed areas (white ellipse) in the lateral area of the plate-like precipitate. The $<110>_{Mo}$ and the $<110>_{ppt}$ include a 45°angle.

In contrast to the edge-on particles, there is a smooth transition visible from the lattice of the matrix to the lattice of the face-on precipitate as shown in Figure 5.17 (a) and Figure 5.17 (b). No disturbance at the interface of the two lattices can be observed. This indicates that in this case the interface is (semi-)coherent. In the image of the face-on particle can be observed that the <100> direction of the matrix is parallel to the <110> direction of the precipitate. Again this can be seen with the help of the lattice model in the image. The green line symbolizes the <110> direction of the matrix and the red line the <110> direction of the precipitate which form again a 45° angle.

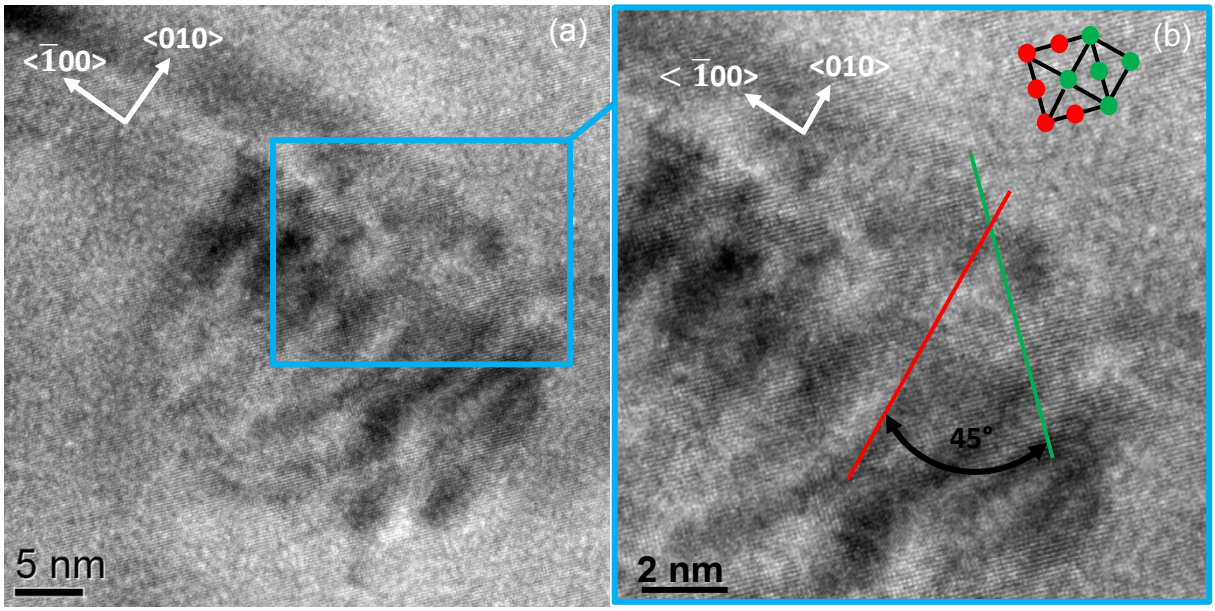

Figure 5.17: TEM micrographs of Ch'. (a) HRTEM image of a face-on precipitate embedded in the matrix. (b) Detail of (a). There is a smooth transition from the matrix (green dots) into the lattice of the precipitate (red dots). The face-on interface is (semi-)coherent.

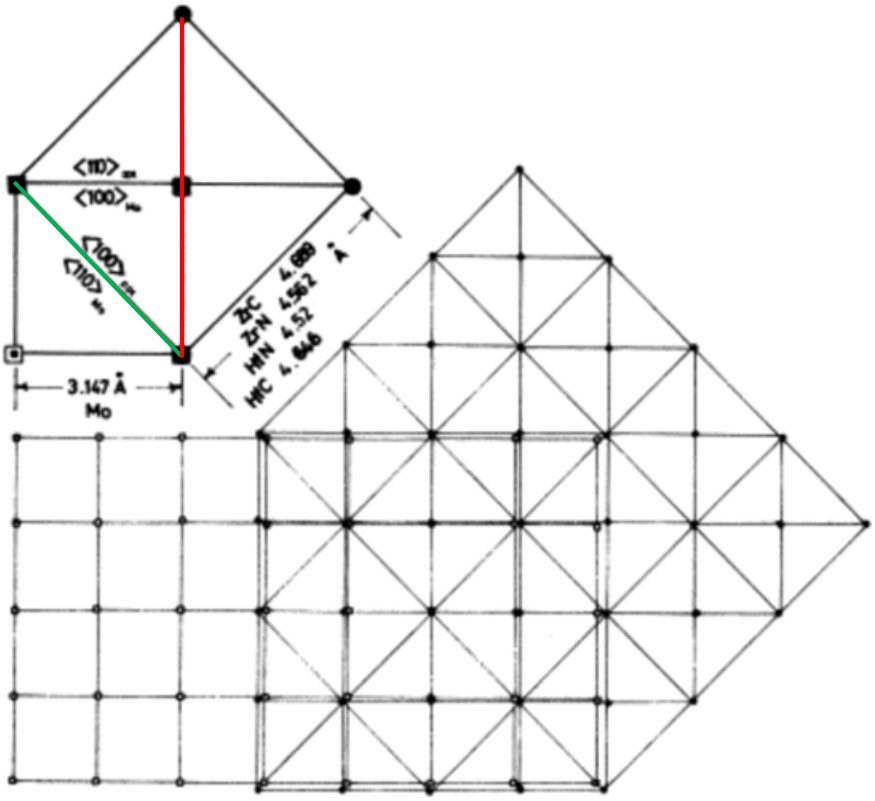

Figure 5.18: Lattice model from Ryan for the orientation relationship between matrix and HfC carbides embedded in the matrix [15].

5.3.2.3 Condition j (Cj)

Figure 5.19 (a) shows the partially recrystallized microstructure of Cj with primary and secondary precipitates embedded in recrystallized areas as well as in the subgrain structure of the matrix. These secondary precipitates can be easily observed in recrystallized areas which is shown e.g. in Figure 5.19 (b). Figure 5.19 (c) reveals that there are nearly no secondary precipitates in the vicinity of big primary Hf- rich carbides. As shown in Figure 5.19 (d), the distribution of the secondary precipitates is not uniform and like in Ch', there are large areas of subgrain structure which contain almost no secondary precipitates.

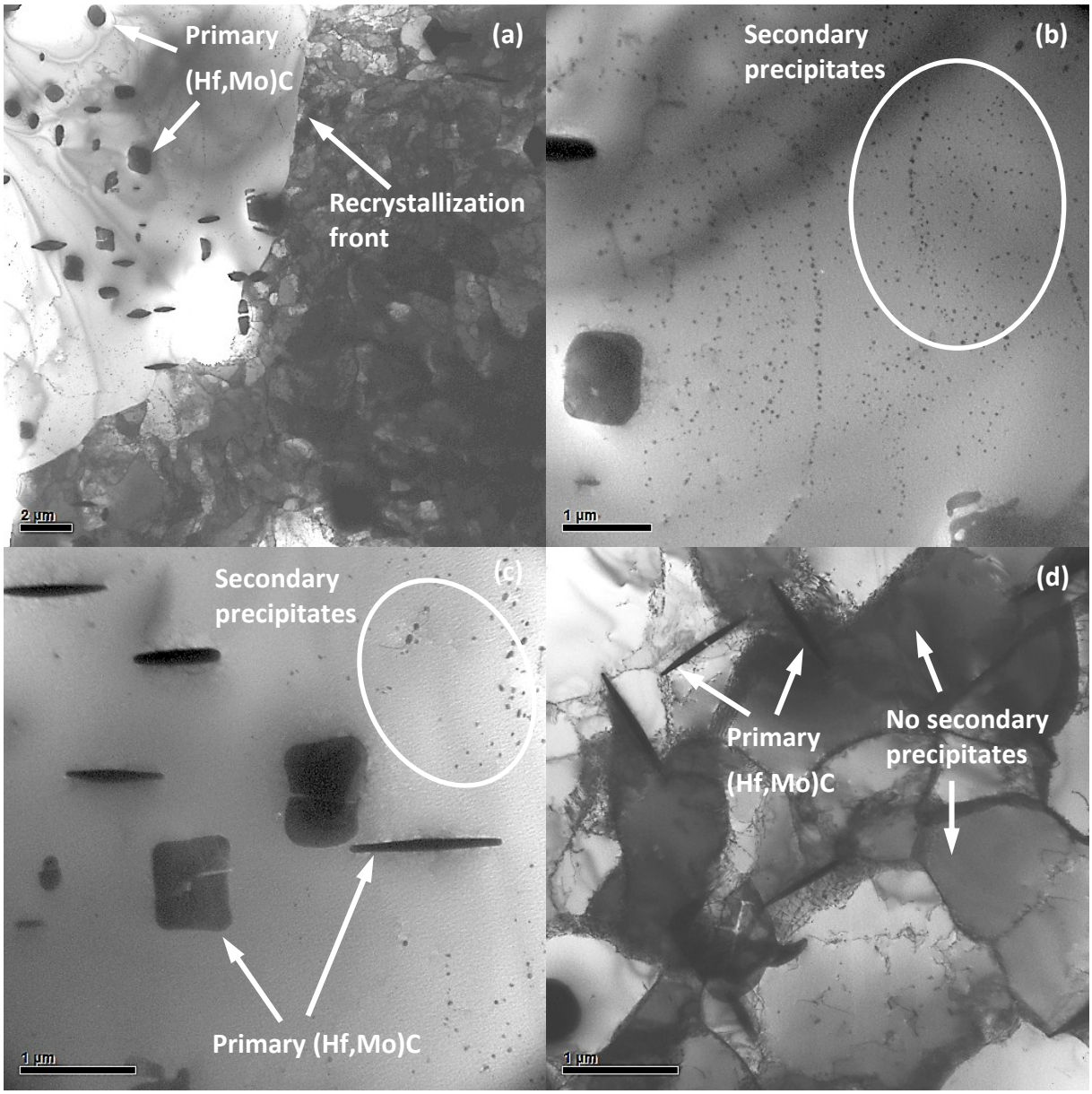

Figure 5.19: TEM micrographs of Cj. (a) Partially recrystallized area. (b) Recrystallized area with many secondary precipitates. (c) No secondary precipitates next to primary (Hf,Mo)C. (d) Subgrain structure with almost no secondary precipitates.

Figure 5.20 (a) and Figure 5.20 (b) illustrate that secondary precipitates are also in this condition preferentially located at dislocations and dislocation networks. The size of these secondary particles in Cj is less than 100 nm and they have a different appearance in recrystallized areas compared to the ones embedded in the subgrain structure. This is shown in Figure 5.20 (c) and Figure 5.20 (d) where the matrix of both images is in [001] zone axis.

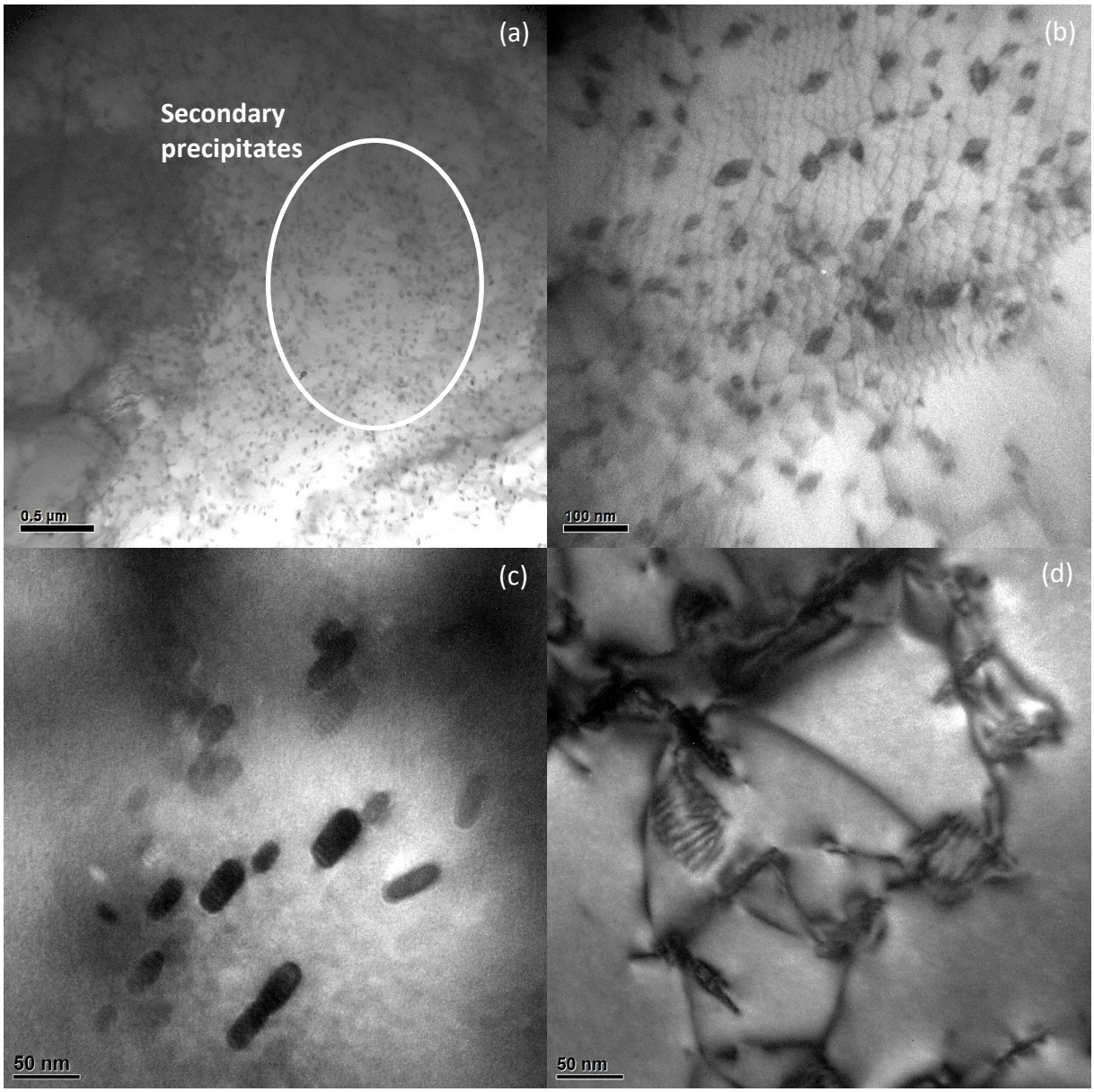

Figure 5.20: TEM micrographs of Cj. (a) Many small precipitates preferentially at dislocations. (b) Detail of (a). Precipitates in [001] zone axis of the Mo matrix in (c) a recrystallized area and (d) in a non-recrystallized area.

Figure 5.21 (a) shows a high resolution TEM micrograph of a precipitate where the recrystallized grain is in [001] zone axis. If the foil is thin enough in this area a quite useful inverse image of it can be recalculated using Fast Fourier Transformation (FFT). It can be seen in Figure 5.21 (b) that the reflections for the precipitate do not have the specific form and ratio which is needed for the orientation relationship as described in the previous section 5.3.2.2. The white dots in the diffraction pattern were added to the image for a better contrast of the matrix reflections. The black dots are reflections from the precipitate. This shows that the orientation relationship secondary precipitate/matrix is not given any more in recrystallized areas and thus the appearance is different as shown in the comparison of Figure 5.20 (c) and Figure 5.20 (d).

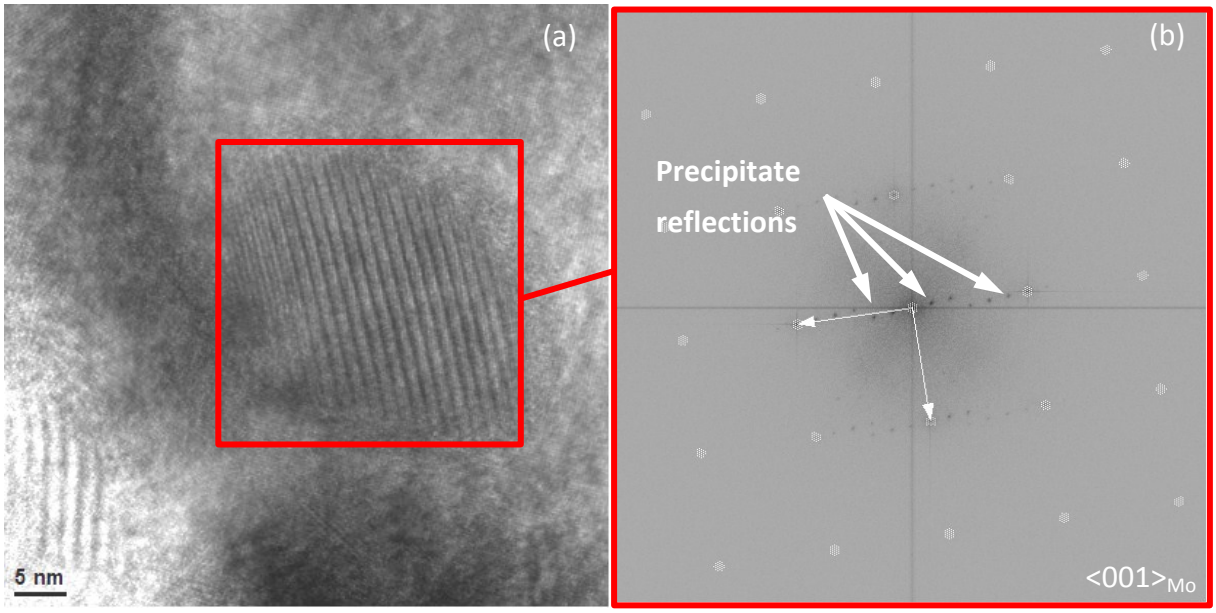

Figure 5.21: TEM micrographs of Cj. (a) Secondary precipitate in a recrystallized area. (b) Reduced FFT form the area framed with a red square in (a).

Figure 5.22 (a) shows a secondary precipitate which stands out of the matrix due to the polishing procedure for thin film foil samples. An EDS measurement was conducted at this particle. In the corresponding EDS pattern in Figure 5.22 (b) Mo and Hf peaks are clearly observable. This leads to two possible explanations where either a part of the bulk material was measured with the particle, or that the particle itself contains molybdenum. In the second case, the secondary precipitates would also be Hf- rich carbides like the primary (Hf,Mo)C [17].

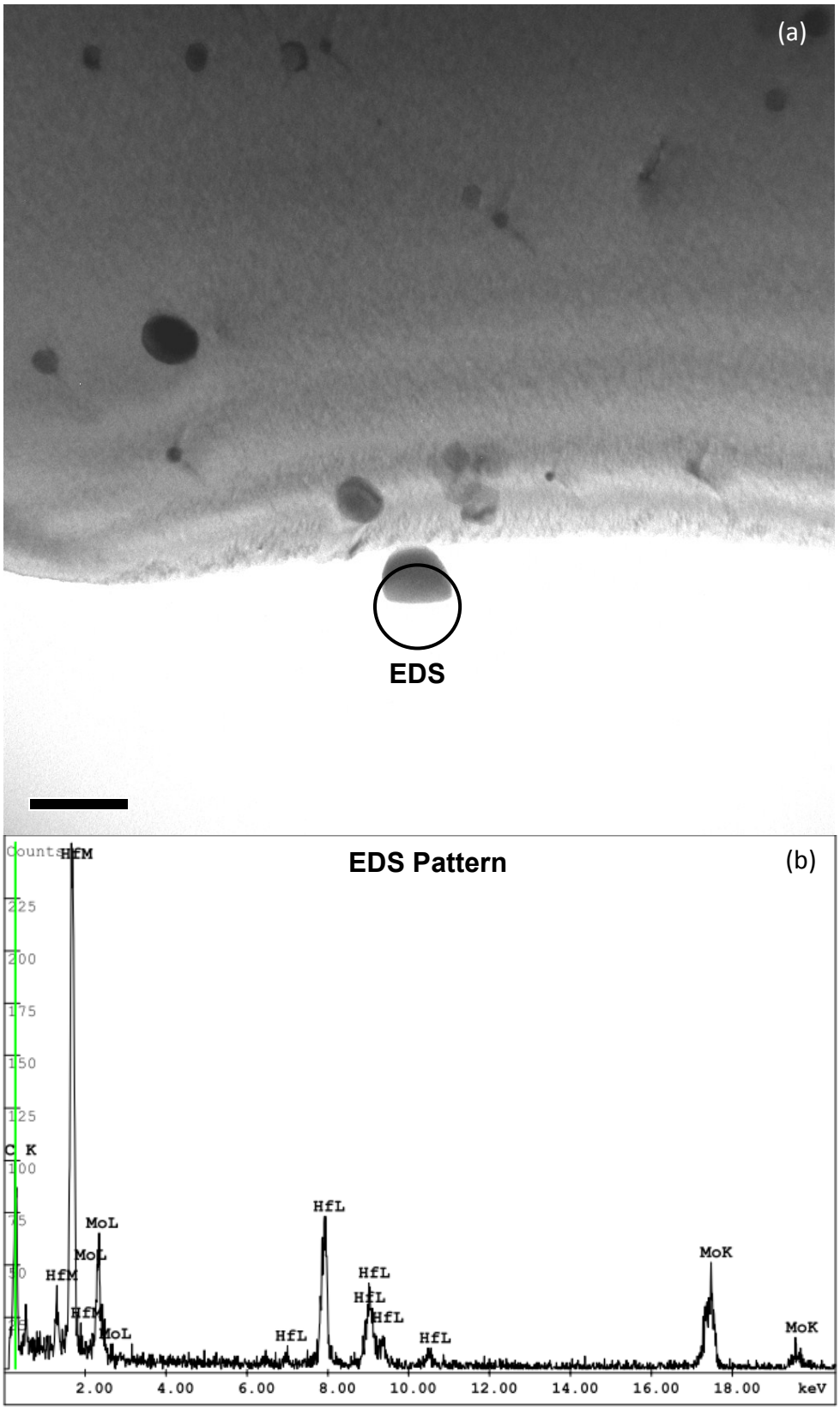

Figure 5.22: EDS measurement of a secondary precipitate in Cj. (a) TEM micrograph of a secondary precipitate which stands out of the matrix. The area for the EDS measurement is marked by a black circle. (b) EDS pattern of the particle shown in (a).

5.3.1 Geometry and size distribution of secondary precipitates in Ch' and Cj

All the images for the particle size measurements of secondary precipitates in Ch' and Cj were taken in [001] direction of the matrix at a magnification of 43000x which is shown for example in Figure 5.23 (a) and Figure 5.23 (b). Figure 5.24 (a) and Figure 5.24 (b) show an image of a secondary precipitate of Ch' which lies face-on and edge-on. The axis *a*, *b* and *c* which were measured are marked by white arrows.

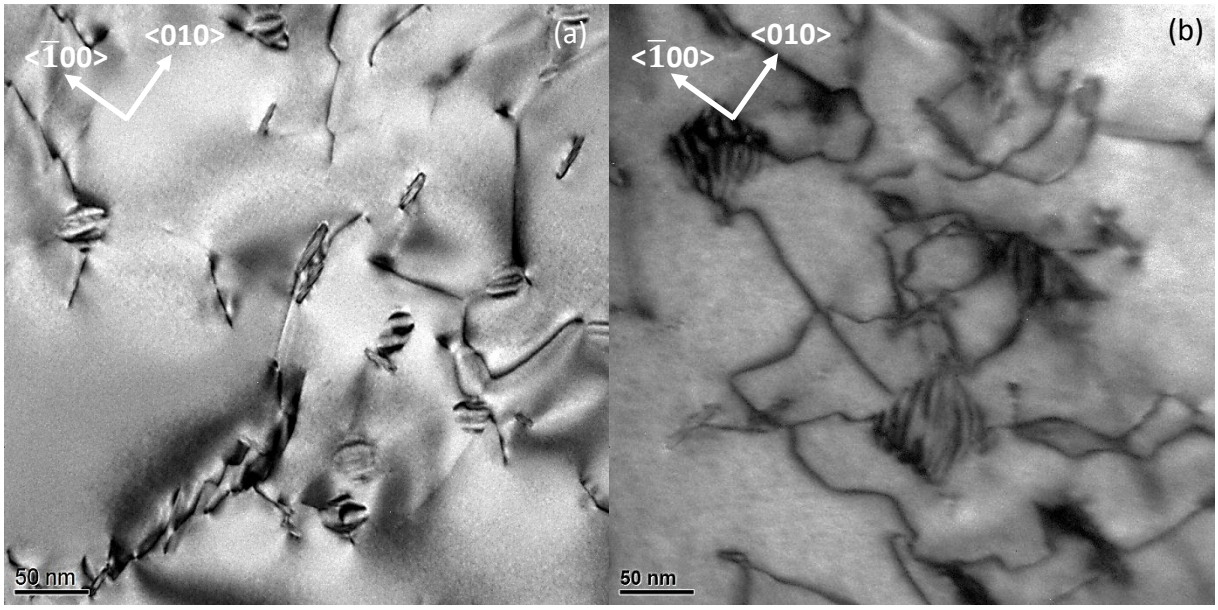

Figure 5.23: TEM micrographs at a magnification of 43000x of (a) Ch' and (b) Cj.

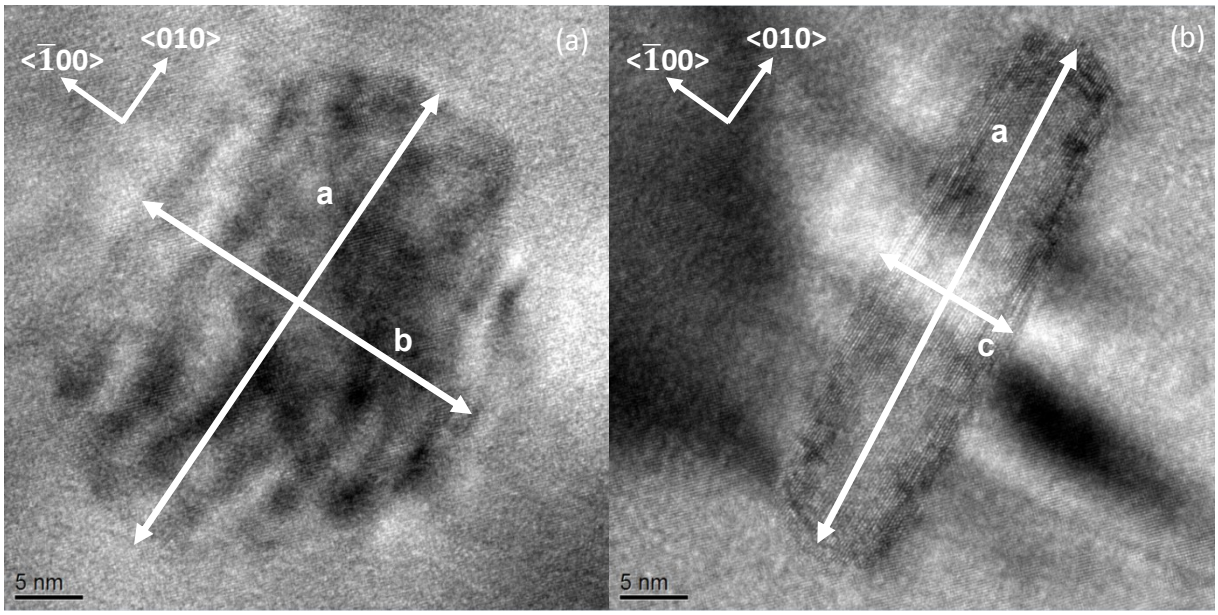

Figure 5.24: TEM micrographs of secondary precipitates from Ch'. (a) Face-on with axis *a* and *b*. (b) Edge-on with axis *a* and *c*.

As illustrated in Table 5.5, size measurements of secondary precipitates were conducted at Ch' and Cj in recrystallized and non-recrystallized areas. The number of edge-on and face-on secondary precipitates of which the axis *a*, *b* and *c* were measured can be seen for each area as well as in total. The best statistic is given for the non-recrystallized area of Cj.

Table 5.5: Number of measured particles in Ch' and Cj in [001] direction of the matrix at a magnification of 43000x.

	Number of measured particles		
Area	**„Edge-on“**	**„Face-on“**	**Total**
Ch' (non- recrystallized)	39	22	61
Cj (non- recrystallized)	131	125	256
Cj (recrystallized)	74	123	197
Total	244	270	**514**

Table 5.6 lists the average sizes of the secondary precipitates from the measured particles mentioned in Table 5.5. It can be seen that the precipitates in the non- recrystallized areas of Cj were approximately twice the size from the ones in Ch'. That means that the secondary precipitates still grew from point h to point j. The average aspect ratio *a/b* is ~1.3 and *a/c* is ~4- 6 for non- recrystallized areas. This *a/c* ratio does not apply for particles in the recrystallized areas (marked red in Table 5.6). As described before, the particles in the recrystallized areas have a different appearance as can be seen in Figure 5.20 (a) and Figure 5.20 (b), where images of the same sample of Cj from an area with and without recrystallization are compared. HRTEM investigations, which are illustrated in detail in Figure 5.21 (a) and Figure 5.21 (b), showed that the particle matrix relationship gets lost when the matrix recrystallizes. That means, that it would not be accurate to measure axis values of secondary precipitates in [001] zone axis of the recrystallized matrix and compare them to the precipitates measured in the subgrain structure.

Table 5.6: Average sizes of axis *a*, *b* and *c* as well as aspect ratios a/b and a/c of secondary precipitates in Ch'and Cj (red values mark inaccurate measurement).

	Axis			Axis ratio	
Area	**a [nm]**	**b [nm]**	**c [nm]**	**a/b face-on**	**a/c edge-on**
Ch' (non- recrystallized)	29.9 ± 8.1	25.0 ± 5.6	5.9 ± 1.5	1.27 ± 0.18	4.82 ± 1.05
Cj (non- recrystallized.)	58.4 ± 15.7	45.1 ± 12.4	10.0 ± 2.7	1.31 ± 0.20	5.99 ± 1.58
Cj (recrystallized)	43.7 ± 15.9	31.1 ± 12.7	16.2 ± 3.8	1.34 ± 0.23	2.90 ± 0.78

Figure 5.25 (a) to (e) show the corresponding particle size distribution for the measured features mentioned in Table 5.6 for the non- recrystallized area of Cj. The particle size distribution for the recrystallized area of Cj was not considered in this thesis due to the loss of the particle/matrix orientation relationship and the one for Ch' due to a low number of particles measured.

Figure 5.25 (a) shows the size distribution for the axis *a* of the total number of edge-on and face-on secondary precipitates. It can be seen that there is a distinct bell-shaped curve with maxima at 60- 70 nm. This is similar for the axis *b* and *c* shown in Figure 5.25 (b) and Figure 5.25 (c) with maxima at 40- 50 nm and 8- 10 nm respectively. The aspect ratio *a/b*, shown in Figure 5.25 (d) has a broader distribution where a less distinct maximum is observable. On the contrary the aspect ratio *a/c* in Figure 5.25 (e) shows again a bell curve with a maximum of 5- 6.

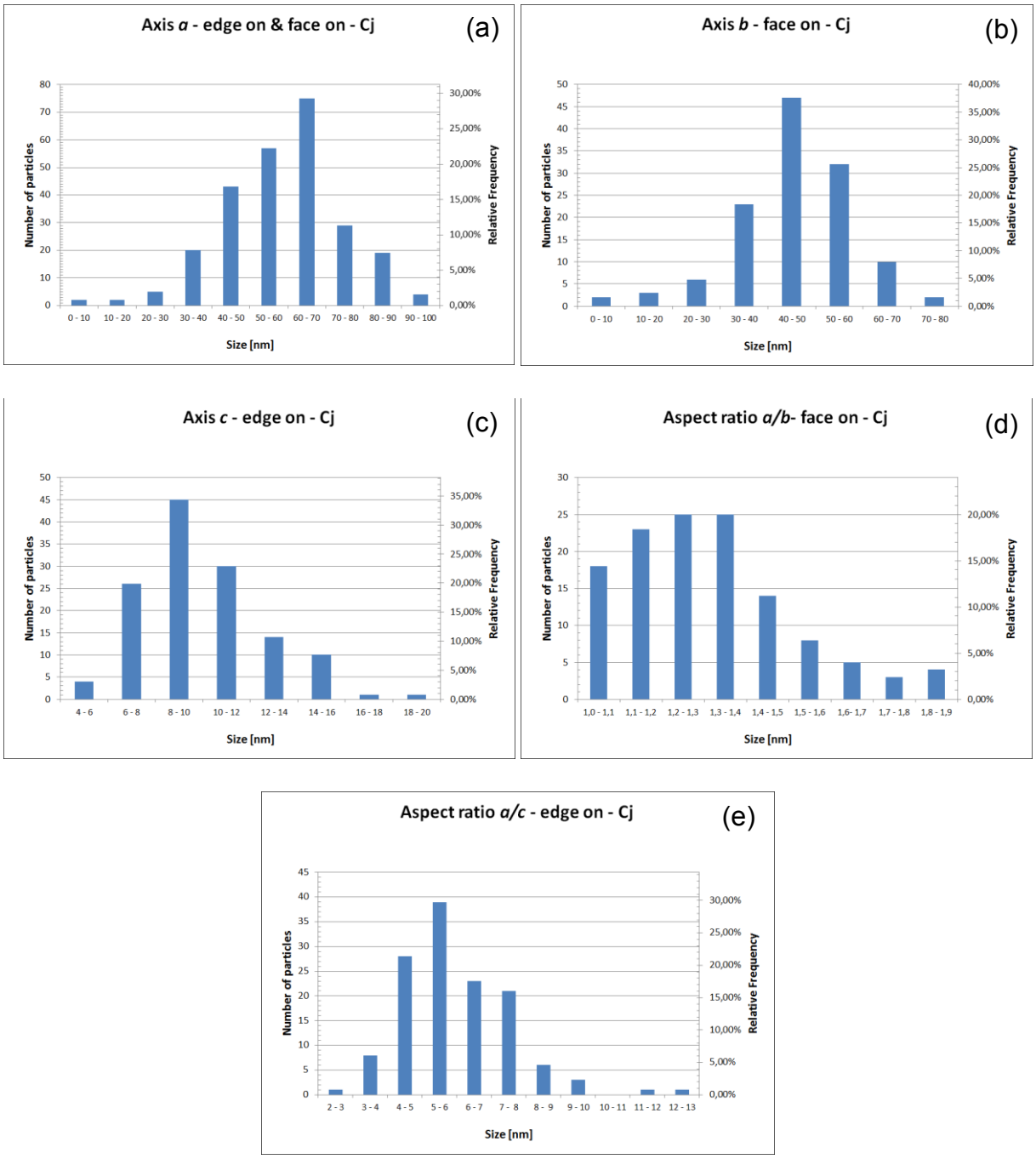

Figure 5.25: Particle size distribution for non- recrystallized areas of Cj. (a) Axis *a* for edge-on and face-on precipitates. (b) Axis *b* (face-on). (c) Axis *c* (edge-on). (d) Aspect ratio *a/b* (face-on). (e) Aspect ratio *a/c* (edge-on).

5.3.2 Atom probe tomography

5.3.2.1 Condition g' (Cg')

Figure 5.26 (a) shows a 3D elemental map of the Hf (blue dots) and C (red dots) distribution of Cg' with a clearly visible cluster in the reconstructed tip volume. Figure 5.26 (b) and Figure 5.26 (c) picture this mapping separately for Hf and C and it can be seen that the Hf and C clustering is overlapping. Table 5.7 lists the bulk composition of this specimen. Compared to the SC there is a higher Hf and C content and it can be seen that there is a high deviation from 0 of the μ values. This confirms a clustering of these elements (μ value see section 3.6). All the other elements in the bulk are distributed homogeneously and have the same contents like in the SC.

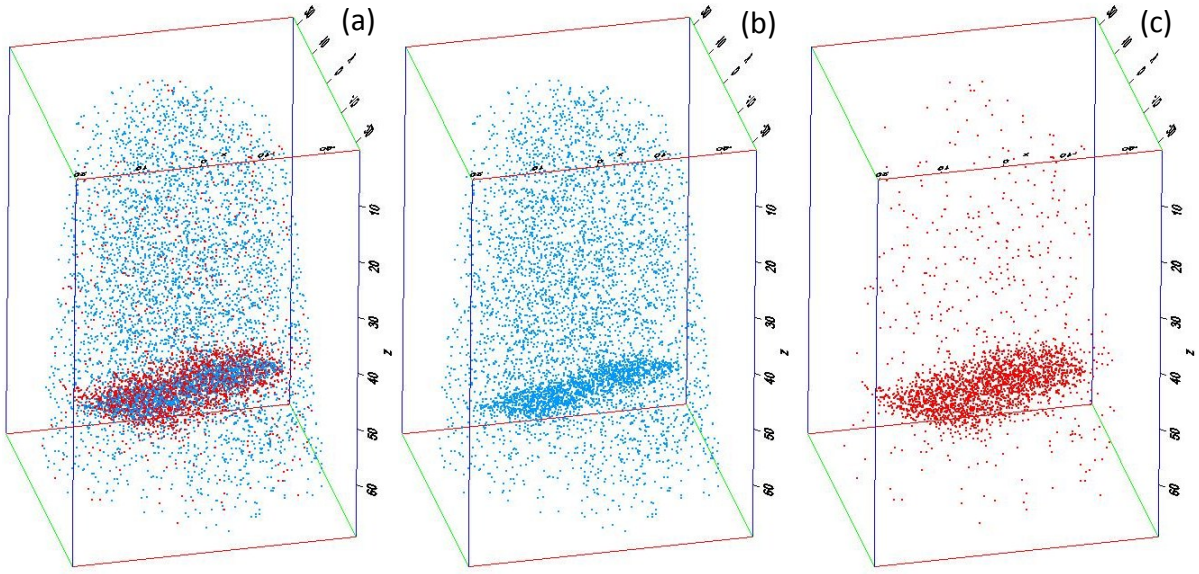

Figure 5.26: 3D elemental map of a specimen from Cg'. (a) Hf and C distribution. (b) Hf distribution. (c) C distribution.

Table 5.7: Bulk composition of the specimen from Figure 5.26. The elevated μ values indicate a clustering of Hf and C.

Element	Content		μ [-]
	[at.%]	[wt.%]	
Mo	balance	balance	-
Hf	0.2687	0.4992	0.1442
C	0.0913	0.0114	0.2947
O	0.0041	0.0007	0.0006
W	0.0096	0.0184	0.0001
Ta	0.0057	0.0107	0.0010
Ga	0.0676	0.0491	0.0112

To get an impression of the Hf and C contents in this cluster, a region of interest (ROI) was positioned through it. This can be seen in Figure 5.27 (a) and Figure 5.27 (b). Figure 5.28 illustrates the 1D concentration plot along the z axis of this ROI. Elevated C and Hf contents can be observed where the ROI penetrates the cluster. It can be seen that there is nearly no C outside the cluster and that the Hf content in this region is in good agreement with that of the SC (~ 0.125 at.%).

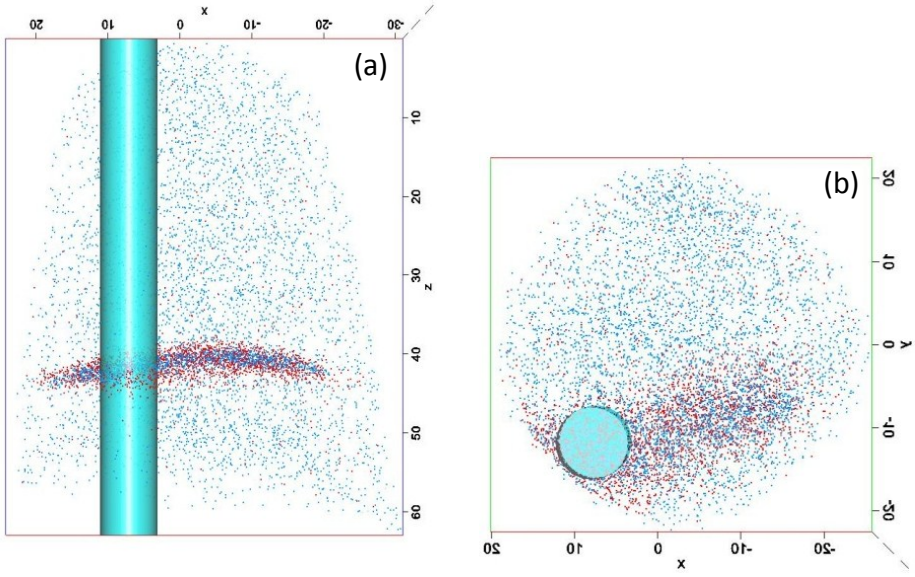

Figure 5.27: 3D elemental map of the specimen from Cg' with a ROI positioned through the cluster in (a) the elevation and (b) the top view.

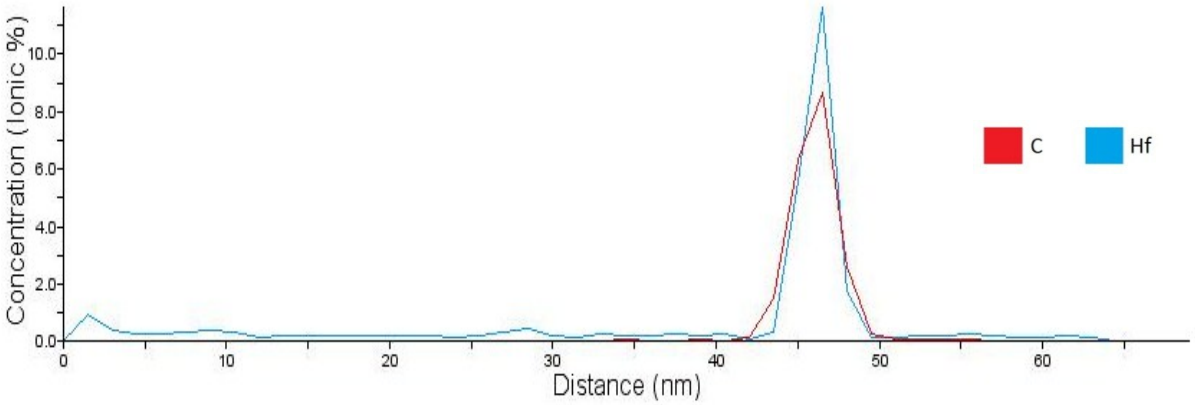

Figure 5.28: 1D concentration profile along the z axis of the ROI from Figure 5.27 of the specimen from Cg'.

For a detailed analysis of the cluster a cluster search for Hf and C was conducted (cluster search algorithm is defined in section 3.6). The used parameters for the cluster search were a fixed distance d_s= 1.42 nm, a minimum number of atoms in the cluster N_{min}= 10 and a distance parameter L= 1.35 nm. As shown in the 3D elemental map of Hf and C in Figure 5.29 only one cluster was found within the bulk of the measured tip from Cg'. Table 5.8 shows the Hf and C contents of this cluster. The cluster and the 1D concentration plot reveal that the cluster has no stoichiometric composition. The value for the solute atoms in the cluster was corrected with the detector efficiency of 37% [28].

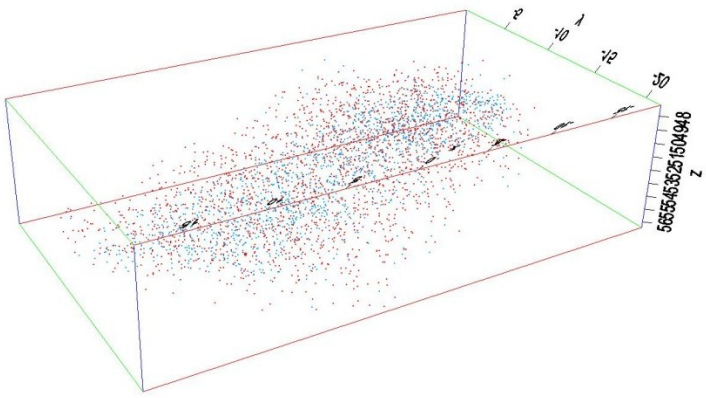

Figure 5.29: 3D elemental map of Hf and C of the cluster in the specimen from Cg'.

Table 5.8: Hf and C content in the cluster of the specimen from Cg'.

Cluster No.	Solute atoms in cluster [-]	Hf [at.%]	C [at.%]
1	9384	5.79	7.59

5.3.2.2 Condition j (Cj)

Figure 5.30 shows the 3D elemental map of Hf of one specimen from Cj. A visual inspection shows that Hf is homogeneously distributed which is confirmed by a low μ value in Table 5.9 (μ value see section 3.6). No C was detected within the matrix. The average bulk composition of three APT specimens from Cj can be seen in Table 5.9. It can be observed that the Hf content in solid solution decreases from the originally ~ 0,125 at.% in the SC to ~ 0.04 at.% in Cj. This result was expected after TEM investigations of Cj where many secondary precipitates were observed. All the other elements are in the same range as for the SC. No secondary precipitate was measured with APT.

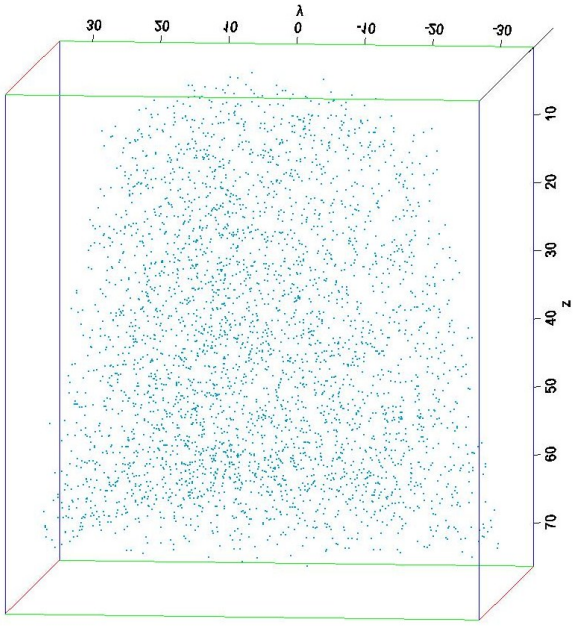

Figure 5.30: 3D elemental map of Hf of a specimen from Cj.

Table 5.9: Average bulk composition of three APT specimens of Cj.

Element	Content [at.%]	Content [wt.%]	μ [-]	Element	Content [at.%]	Content [wt.%]	μ [-]
Mo	balance	balance	-	**Hf**	0.0395	0.0735	0.0097
C	-	-	-	**W**	0.0119	0.0228	0.0022
O	0.0085	0.0014	0.0007	**Ga**	0.0366	0.0266	0.0001
Ta	0.0045	0.0085	0.0002				

5.4 Microstructure after heat treatment without deformation

In order to compare the microstructural and compositional differences of deformed and undeformed samples, specimens of the as-sintered condition were processed to point j (SCj) of the TMP without any deformation (see section 4.1 and 4.2). Additionally, a long term heat treatment experiment was carried out. In this case, the sintered samples were heated up in 10 min to 1600°C and held at this temperature for 10 h (SC10h1600C). Then they were quenched with nitrogen to RT (see section 4.2) and investigated with OLM, TEM and APT.

5.4.1 OLM microstructure of SC10h1600C

Compared to the OLM micrograph of the SC in section 5.1, Figure 5.31 shows that the intergranular Mo_2C is vanished after the long term heat treatment at 1600°C. Like in the TEM investigations of SC10h1600C in the following section it can be seen that primary Hf- rich carbides are still present (black phase). This means that Mo_2C is thermodynamically not as stable as (Hf,Mo)C in MHC at 1600°C. HfO_2 has a grey appearance and is preferentially located at grain boundaries but it is also visible inside the grains. The average grain size is ~ 100 µm.

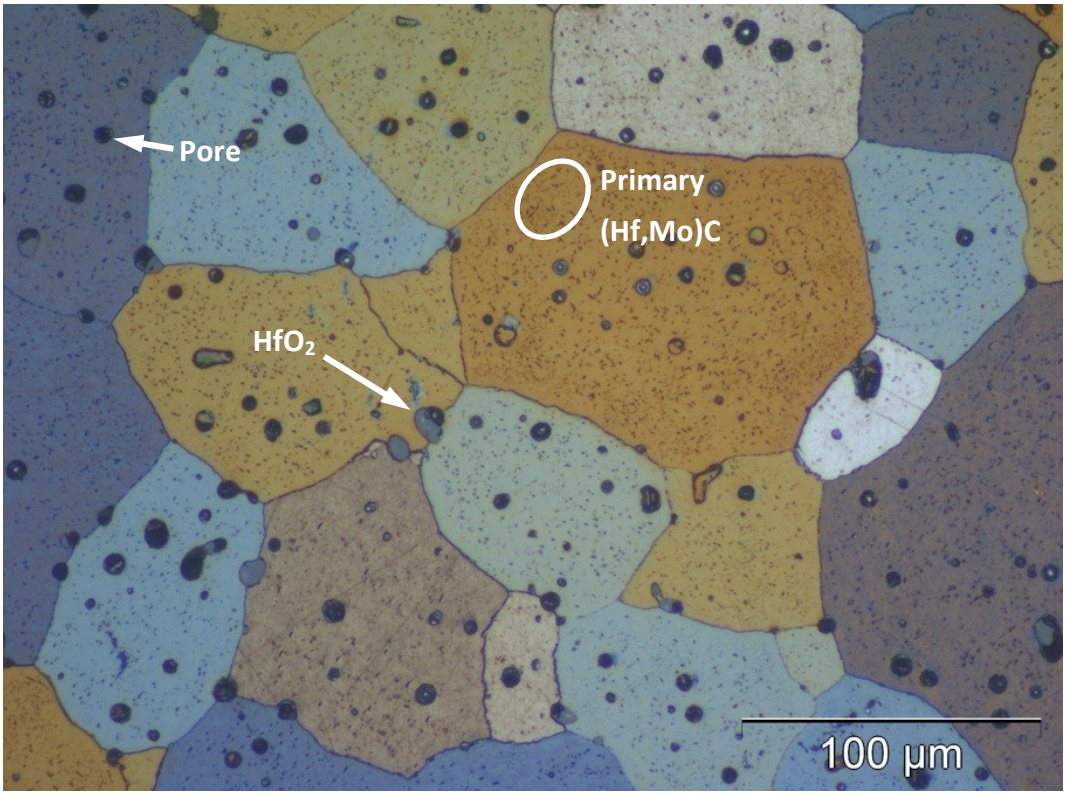

Figure 5.31: OLM micrograph of the SC10h1600C. Intergranular Mo_2C dissolved during the long term heat treatment. Etched with Hasson etchant [17,22].

5.4.2 TEM investigations of the SCj and SC10h1600C

Figure 5.32 (a) and Figure 5.32 (b) show typical TEM micrographs of the SCj. Since the sample was not deformed, there is no subgrain structure visible. Within the matrix primary Hf- rich carbides and a few, small isolated secondary precipitates on dislocations are embedded.

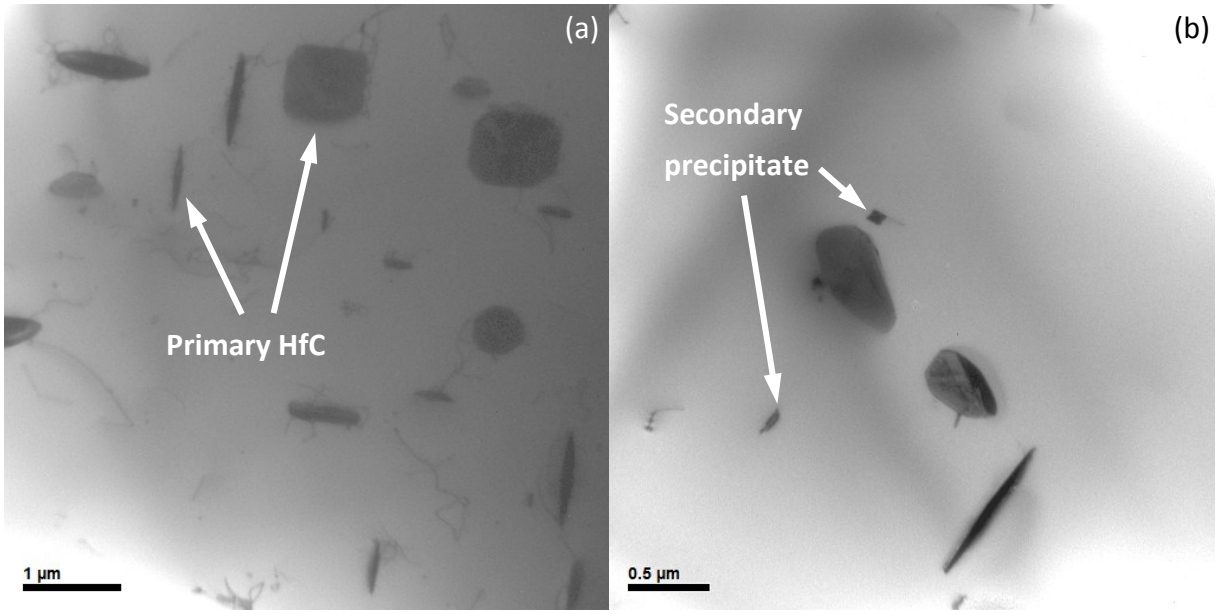

Figure 5.32: TEM micrographs of the SCj. (a) The microstructure of the SCj with primary (Hf,Mo)C carbides and a few isolated secondary precipitates on dislocations. (b) Detail of (a).

The samples of SC10h1600C basically show after 10h of tempering at 1600°C the same microstructure as SCj, but there are more and larger isolated secondary precipitates embedded in the matrix. Like for all the other investigated conditions these secondary precipitates are located on dislocations. This is illustrated in Figure 5.33 (a) and Figure 5.33 (b).

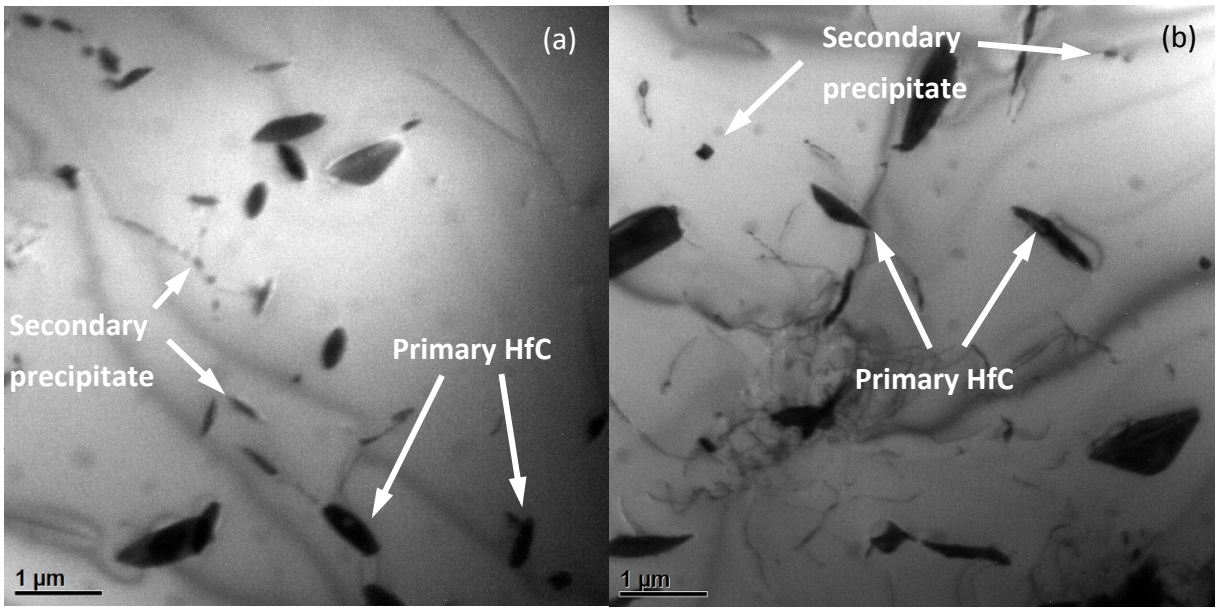

Figure 5.33: TEM micrographs of the SC10h1600C. (a) Microstructure with a few isolated secondary precipitates. (b) Like (a) but different area.

5.4.3 Atom probe tomography

5.4.3.1 Sintered condition j (SCj)

The Hf and C distribution of one specimen from the SCj is illustrated in a 3D elemental map in Figure 5.34. The point size of the C atoms was increased from 1 to 1.5 for a better visualization of the C content. It can be seen that Hf and C is homogeneously distributed which is confirmed by low μ values (μ value see section 3.6). Table 5.10 shows the average bulk composition of four APT specimens from SCj. The contents for all the elements are basically the same as for the SC. There is nearly no C in solid solution after the heat treatment of the samples. As expected from the TEM investigations of the SCj (previous section) where only a few isolated secondary precipitates are visible, there is still the same amount of Hf left in solid solution as for the SC.

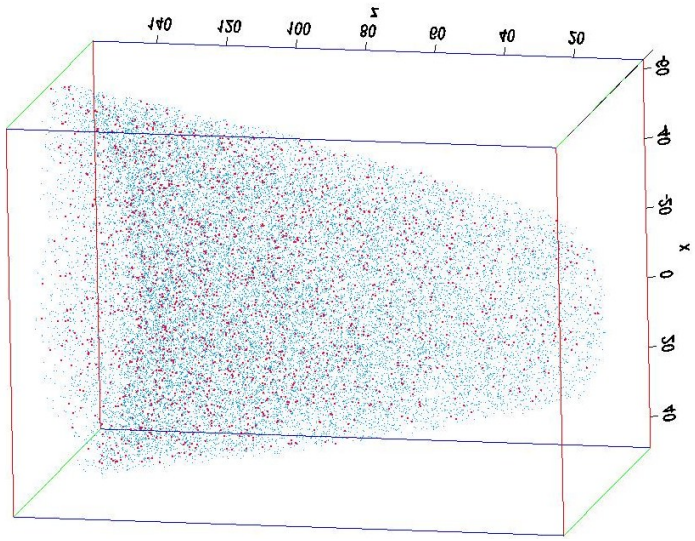

Figure 5.34: 3D elemental map of Hf (blue) and C (red) of a specimen from the SCj.

Table 5.10: Average bulk composition of four measured specimens of SCj.

Element	Content		μ [-]	Element	Content		μ [-]
	[at.%]	[wt.%]			[at.%]	[wt.%]	
Mo	balance	balance	-	**Hf**	0.1221	0.2269	0.0028
C	0.0031	0.0004	0.0005	**W**	0.0077	0.0147	0.0035
O	0.0032	0.0005	0.0002	**Ga**	0.0076	0.0055	0.0001
Ta	0.0011	0.0021	0.0001				

5.4.3.2 Sintered condition tempered 10h at 1600°C (SC10h1600C)

Figure 5.35 illustrates a 3D elemental map of Hf and C. It can be seen that these elements are homogeneously distributed within the reconstructed tip volume. This is confirmed by low μ values (μ value see section 3.6). There is an elevated µ value for Ga observable in Table 5.11. This indicates that only one polishing step with 5 kV during FIB preparation of the specimens was not sufficient in order to remove most of the Ga ion imprint at surface near regions. Table 5.11 illustrates the average bulk composition of three measured specimens from SC10h1600C. It can be seen that the Hf content is slightly higher than for the SC. Unlike as expected from the fact that Mo_2C dissolves with increasing tempering time, there is no additional C in solid solution. Due to this discrepancy, additional combustion analysis of Cj, SCj and SC10h1600C were conducted at Plansee SE in order to find possible explanations for the missing C content. This will be discussed in detail in section 6.

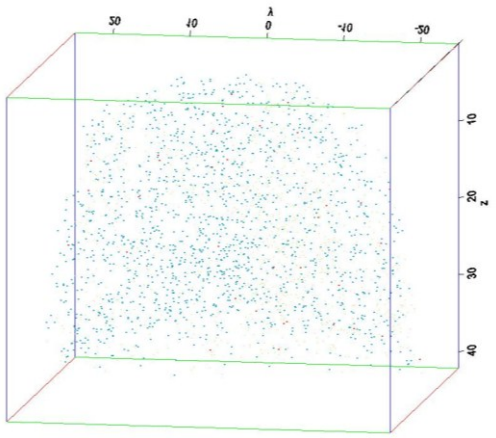

Figure 5.35: 3D elemental map of Hf (blue) and C (red) of a specimen from the SC10h1600C.

Table 5.11: Average bulk composition of three APT specimens from the SC10h1600C.

Element	Content		μ [-]	Element	Content		μ [-]
	[at.%]	[wt.%]			[at.%]	[wt.%]	
Mo	balance	balance	-	**Hf**	0.1422	0.2643	0.0011
C	0.0014	-	0.0001	**W**	0.0045	0.0086	0.0003
O	0.0122	0.0020	0.0017	**Ga**	0.0259	0.0188	0.0263
Ta	0.0039	0.0073	0.0004				

5.5 X-ray diffraction (XRD) patterns of all investigated conditions

The XRD patterns in Figure 5.36 (a) to (e) are ordered chronologically according to the thermo-mechanical process where Figure 5.36 (f) is the pattern for the long term heat treatment SC10h1600C.

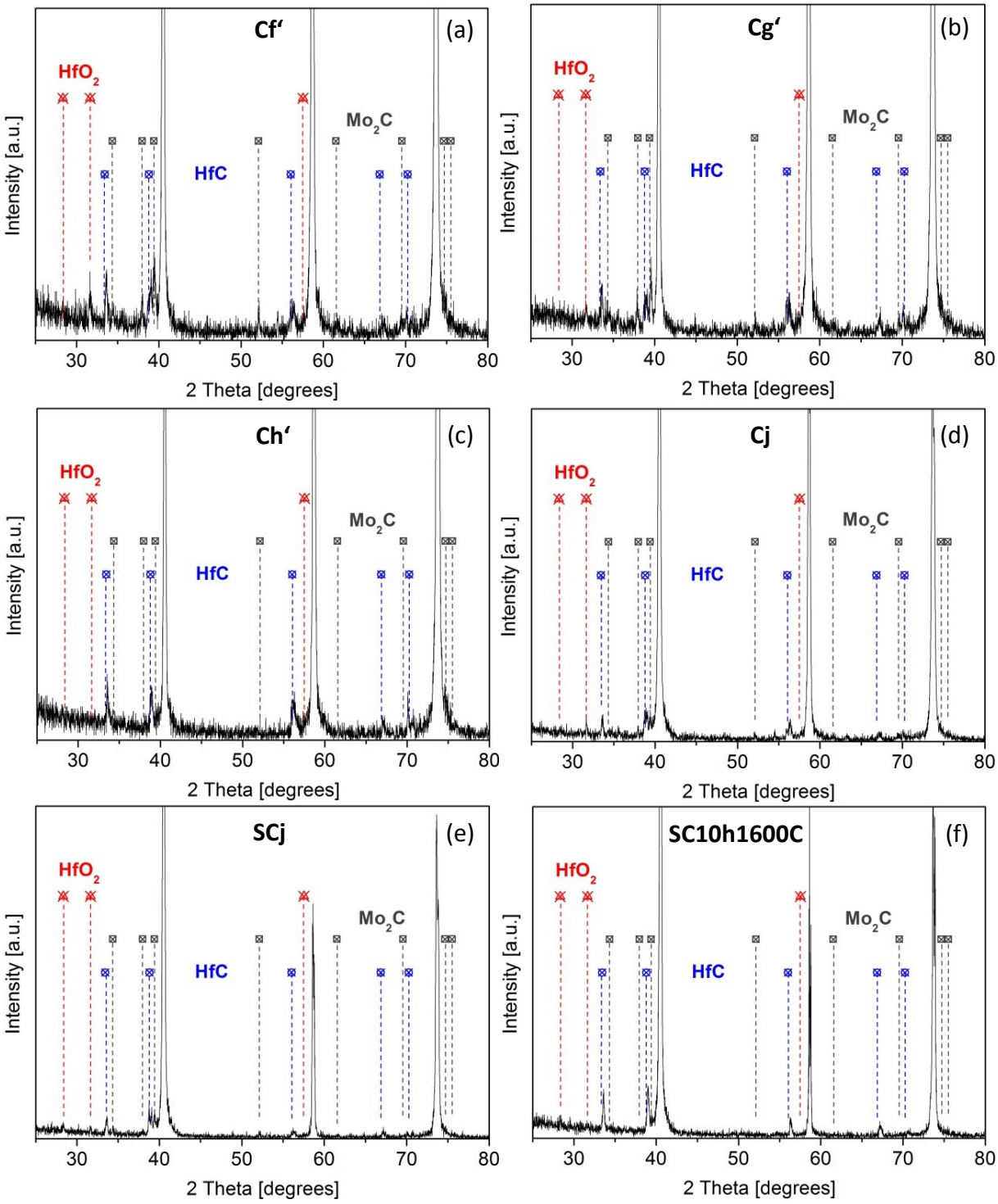

Figure 5.36: XRD patterns for (a) Cf', (b) Cg', (c) Ch', (d) Cj, (e) SCj and (f) SC10h1600C.

The 2θ angles for the Mo_2C peaks are marked by black dotted lines in the XRD pattern, the ones for HfO_2 with red lines and the ones for HfC with blue lines.

The peaks for the Mo matrix are the most distinctive. They appear at a 2θ angle of 40.5°, 58.6° and 73.6° [36].

When comparing the XRD patterns for Cf' to SCj it can be seen that the peaks for Mo_2C, especially the one at a 2θ angle of 39.393°, are decreasing constantly with tempering time of the TMP and vanish for the long term experiment SC10h1600C.This confirms the OLM investigation in section 5.4.1.

Furthermore, it can be seen that the peaks for Hf- carbide have a shift to higher angles compared to literature values. This means that the lattice parameter gets smaller [35], which indicates that the secondary carbides must also contain molybdenum and thus they are as well mixed carbides like described for primary (Hf,Mo)C [17]. However, this assumption is not clearly verified for secondary precipitates at this point of investigation.

The peaks for HfO_2 are visible in every condition and a noticeable change was not observed.

5.6 Microhardness testing HV0.1

The microhardness was only determined for estimation purposes of the strength development during the thermo-mechanical processing of MHC. These values are without any exception only of qualitative nature. Figure 5.37 shows an OLM mirograph of a microhardness imprint in Cf'. The measurements were only conducted within the grain of the matrix in order to avoid influences of oxides, pores or the intergranular Mo_2C. Table 5.12 lists the average microhardness of all specimens. It can be seen that the highest hardness value is given for Cf' and Cg'. In Cf' the microstructure consists exclusively of a subgrain structure and in Cg' there are only a few small secondary precipitates existing. The hardness decreases with increasing tempering time as can be seen for Ch' and Cj. The SC, SCj and SC10h1600C have nearly the same values since there was no deformation introduced as well as no proper amount of secondary precipitations were formed.

Table 5.12: Microhardness HV0.1 for the different conditions of the TMP. Each value represents an average value of 5 measurements.

Specimen	SC	Cj	SCj	Cf'	Cg'	Ch'	SC10h1600C
HV0.1	214	251	217	298	302	295	201
Standard deviation	4	13	9	7	6	8	9

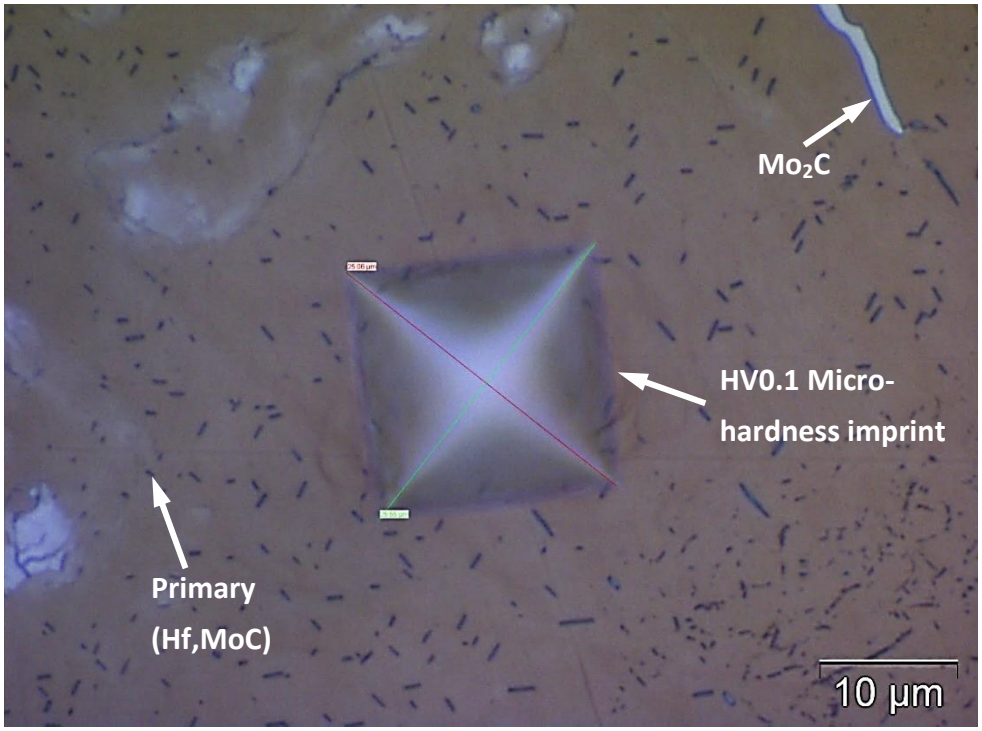

Figure 5.37: OLM micrograph of Cf' with a microhardness imprint in the matrix. The sample was etched with Hasson etchant [22].

6 DISCUSSION

In order to reveal the precipitation mechanism of secondary precipitates in the MHC alloy, the as-sintered condition of the sample material as well as the conditions f', g', h' and j of the thermo-mechanical process (see section 4.1 and 4.2) were investigated with OLM, SEM, XRD, TEM and APT. The microstructural and compositional differences of deformed and undeformed samples were compared. Therefore specimens of the as-sintered condition were processed to point j (SCj) of the TMP without any deformation (see section 4.1 and 4.2) and compared to Cj. Additionally, a long term heat treatment experiment was carried out with the aim to study compositional effects. In this case, the sintered samples were heated up in 10 min to 1600°C and held at this temperature for 10 h (SC10h1600C). Then they were quenched with nitrogen to RT (see section 4.2).

The overall chemical analysis of the SC displayed a C content of ~0.85 at.% and a Hf content of ~0.64 at.%. The OLM micrographs of the sintered material showed primary (Hf,Mo)C and Mo_2C, which formed during slow cooling in the furnace from the sinter temperature of about 2200°C in H_2 environment. The primary Hf- rich carbides had a length of ~1 µm and were uniformly distributed within the matrix. Hf- oxide was located in the grains or in combination with molybdenum carbide which is predominantly located at grain boundaries. The relative density of the material was 96% and the average grain size was ~100 µm.

XRD measurements of the SC showed a peak shift for HfC to a higher 2θ angle which indicates that the lattice parameter is smaller than for HfC. This can be explained by the replacement of Hf atoms with smaller Mo atoms in the lattice of the primary precipitates. Additionally, EDS measurements with TEM pointed out that the primary Hf- carbides are mixed carbides. TEM micrographs of the SC revealed primary precipitates and a matrix with a low dislocation density. As reported in literature for the as-sintered condition of MHC it was observed that the primary (Hf,Mo)C were plate-like shaped [17].

Raffo and Ryan used for their investigations arc melted Mo- Hf- C alloys which were all solution annealed at high temperatures and extensively quenched prior to heat treatment. In comparison to the powder metallurgically processed MHC all the Hf and C was in solid solution, which means there were no primary Hf- carbide precipitations as well as no Hf-oxide particles embedded in the matrix due to non-existent O sources in the process route. That means that unlike for MHC all the Hf and C was available to form precipitates in a following aging step [3-4,14-15]. There are no reports in the literature of arc melted alloys that these precipitated Hf- carbides are mixed carbides.

Atom probe measurements of the as-sintered condition revealed a Hf content of ~0.12 at.%, but no C in solid solution. This leads to the conclusion that ~0.5 at.% Hf from the overall Hf content was stored in primary Hf- rich carbides and Hf- oxides. This means that the main part of Hf was not available for the formation of secondary precipitates. The C which was not consumed by the formation of primary Hf- rich carbides and Hf- oxides formed intergranular molybdenum carbide.

For a direct comparison of the beginning (SC) and the end of the thermo-mechanical process Cj was investigated with emphasis on its microstructure and composition. APT investigations revealed that there was also no C in solid solution and that the Hf content in the bulk decreased from the originally ~0.12 at.% from the SC to ~0.04 at.% in Cj. TEM micrographs of Cj showed a partially recrystallized matrix with primary (Hf,Mo)C embedded in it. This indicated that a deformation degree of φ=0.27 was not enough for the applied heat treatment in order to receive a fully recrystallized matrix. Additionally, many secondary precipitates were found in recrystallized areas as well as in areas with subgrain structure. They were preferentially located on dislocations and dislocation networks. It is not known at this point of investigation how much the secondary and primary precipitates influence recovery and recrystallization processes in MHC. The formation of secondary precipitates explained the decrease of the Hf content in the bulk to ~ 0.04 at.%. It was shown that the distribution of these carbides was not homogenous. There were subgrains without any secondary precipitates and there were no secondary precipitates in the vicinity of primary Hf- rich carbides. This might have been caused by a difference in local deformation behavior of differently orientated grains. It was shown in the microstructural evolution of pure molybdenum during hot deformation that two main fibers develop when dynamic recrystallization occurs. Firstly, there is the <111> fiber which is known as the hard fiber. It has a high Taylor factor and needs many glide systems for deformation. Secondly, there is the soft <001> fiber which needs only a few glide systems and thus the input of dislocations might have been different [42]. The investigations of Cj led to the question where the C for the formation of secondary precipitates came from.

Therefore the microstructure after deformation without a following aging step (Cf') was investigated. TEM micrographs of Cf' revealed a distinct subgrain structure containing primary Hf- rich carbides. No secondary precipitates were found in this condition. Due to recovery processes there were areas where no dislocations were located within some of these subgrains. Different than for the SC, APT investigations of Cf' showed a clustering of Hf and C. The bulk composition outside these clusters was the same as for the SC. The first clustering of these elements happens immediately after the deformation during the slow cooling period in section D in the TMP where still elevated temperatures are existing. This indicates that there were high diffusivity paths (pipe diffusion) along dislocations, dislocation networks and subgrain boundaries which were introduced by strain [7,12]. Such a behavior was reported in literature for strain induced NbC precipitates in ferrite. Like HfC has NbC a sodium chloride structure and these precipitates develop the same plate-like morphology in

ferrite (bcc) as HfC in Mo (bcc) [16,43]. The kinetics of Nb(C,N) precipitation was studied in both undeformed and deformed austenite. Supersaturation determines the “driving force” i.e. the free enthalpy change to start of the precipitation. However, the introduction of strain provided sites for nucleation as well as enhanced diffusion rates by pipe diffusion. Therefore precipitation was observed at a lower supersaturation. Diffusion of Carbon and Nitrogen is 5-7 orders faster than diffusion of niobium, thus diffusion of niobium is expected to be the rate controlling element which was also the case for Hf for the formation of secondary precipitates in MHC [44]. A cluster search revealed that the found clusters had no stoichiometric composition. Additionally, APT showed that the Hf and C content outside the clusters was the same as the bulk composition in the SC.

The XRD pattern for Cf’ illustrated like for the SC, the typical peaks for the matrix, HfO_2, primary (Hf,Mo)C and Mo_2C, especially the one at a 2θ angle of 39.393° [17]. This was different for Cj. The Mo_2C peaks were clearly reduced compared to the ones for Cf’. This indicates that Mo_2C dissolved successive by increasing time of heat treatment.

APT investigations showed that, there was no C in solid solution, neither in the SC nor in any other condition of the thermo-mechanical process. The conclusion of this and the findings of the XRD investigations from Cf’ compared to Cj is that the C for the precipitation reaction of secondary precipitates in the MHC alloy was delivered by the dissolution of intergranular molybdenum carbide. Simultaneously the introduction of strain was necessary in order to provide heterogeneous nucleation sites and pipe diffusion to produce a significant number of secondary precipitates at a lower degree of supersaturation. Literature reports different mechanisms for the formation of precipitates in arc melted molybdenum based Hf- C and TI-Zr- C alloys. These alloys had been solution annealed and rapidly cooled in order to get a supersaturation of group IVa elements and C. For Mo- Hf- C alloys all the Hf and C was in solid solution and after aging precipitation occurred homogeneously within the matrix [3-4,14-15]. This was not the case for powder metallurgically processed MHC. The mechanism found in this thesis is not equal but very similar to the precipitation behavior of Mo-TZC, Mo-Ti- C and Mo- Nb- TZM alloys. After quenching of the solution annealed alloys it was noted that a considerable amount of molybdenum carbide was present in the microstructure. This carbide was distributed within the grains in form of large needles or thin Widmannstätten plates. Additionally, there was a high dislocations density associated with the formation of these large carbide needles. It was assumed that these dislocations formed as a result of rapid growth of the molybdenum carbide as well as from differential thermal contraction during cooling. Examinations after aging of these alloys reported the dissolution of molybdenum carbide accompanied by the precipitation of Zr and Ti carbide phases on dislocations [14]. In the case of MHC the molybdenum carbide was present as an intergranular phase and there was no supersaturation of Hf given. Most of the alloying elements were stored in primary carbides or oxides which had been a result of the powder metallurgical process route. The precipitation behavior of NbC in ferrite is also strain

induced. The difference to the precipitation mechanism of secondary precipitates in MHC is that in the case for the low alloyed steel both, the C and Nb are in solid solution [45].

In order to investigate the influence of deformation on the formation of secondary precipitates specimens of the as-sintered condition were processed to point j of the TMP without any deformation (SCj). TEM investigation of these samples showed that without the introduction of strain (dislocations) prior to heat treatment only a few isolated secondary precipitates were formed throughout the whole microstructure of the MHC alloy. Like for Cj these precipitates were located preferentially on dislocations and dislocation networks. This consequently means that powder metallurgically processed MHC needs the introduction of strain prior to heat treatment to produce a significant number of secondary precipitates. Or, in other words, dislocations are needed for heterogeneous nucleation sites [7-8]. As mentioned before for Cf' there were subgrains without any dislocations inside and there were subgrains in Cj without any secondary precipitates. These facts indicate that recovery processes prior to an aging step assist a non-uniformly distribution of secondary precipitates in MHC. APT measurements of samples from SCj showed, as expected, that the same amount of Hf as for the SC was in solid solution but there was no carbon present in the bulk.

After revealing the secondary precipitation mechanism the investigations were focused on the evolution of these particles with samples from Cg', Ch' and Cj. TEM investigations of Cg' revealed a subgrain structure like in Cf' but in comparison to Cf' there were already some small secondary precipitates existing next to the primary Hf- rich carbides. As for all the other conditions they were located preferentially at dislocations and dislocation networks. This indicates that the beginning of the precipitation reaction is in the heating period of section F shortly before point g at elevated temperatures. The TEM micrographs of Ch' showed like Cj a partially recrystallized matrix and many small precipitates embedded in the recrystallized areas as well as in the subgrain structure. It can be seen that the secondary precipitates are not uniformly distributed. TEM samples of Ch' were tilted and the secondary precipitates of the powder metallurgically processed MHC showed a plate-like shape. This was mentioned in literature for arc melted Mo- based alloys as well as for the primary (Hf,Mo)C in the as-sintered condition of the MHC alloy [3-4,15,17].

It was confirmed that the plate-like secondary precipitates and the matrix have an orientation relationship with each other, where the <100> direction of the matrix is parallel to the <110> direction of the precipitates. The same orientation relationship and morphology was reported by Ryan for arc melted Mo- Hf- C and Mo- Ti- Zr- C alloys [15]. Furthermore, he investigated the mismatch between the matrix and the precipitates theoretically in many directions. His research showed that the lowest mismatch of 4.3 % is in the direction of the mentioned orientation relationship and thus it is energetically favorable for secondary precipitates to develop the $\{100\}_{Mo}//\{100\}_{ppt}$ habit planes in molybdenum

[7,15]. TEM studies of NbC in ferrite showed that the plate-like NbC precipitates have the same orientation relationship as reported by Ryan for arc melted Mo- Hf- C alloys. In the case of NbC in ferrite this relationship is called Baker-Nutting relationship [41,43].

HRTEM investigations also confirmed that the lateral areas of the secondary precipitates in MHC were incoherent and that the face-on interfaces were (semi-)coherent. The incoherent interface has a high interfacial energy but simultaneously a low misfit energy and therefore it is growing fast. It is the other way for (semi-)coherent interfaces which grow by a slow ledge mechanism. These two different growth mechanisms caused by interfacial and misfit energies explain the plate-like shape of the secondary precipitates [7].

Additionally, TEM investigations of Cj revealed that secondary precipitates have a different appearance in recrystallized areas compared to precipitates in subgrain structure. Diffraction experiments showed that the reason for this was the loss of the orientation relationship between matrix and secondary precipitates due to recrystallization. A similar behavior was reported for NbC precipitates in low alloyed steel. Slow cooling after deformation resulted in interphase precipitation during the α/γ phase transformation and subsequent precipitation occurred also in ferrite [46]. All the Niobium particles that precipitated in austenite became incoherent upon the austenite-ferrite transformation. Basically, this phase transformation is like recrystallization a rearrangement of the lattice and thus the loss of coherency of NbC in ferrite is comparable to the one of secondary precipitates in MHC [47].

Particle measurements were carried out with TEM in [001] zone axis of the matrix at a magnification of 43000x. The size distributions of Cj illustrated that the average particle size measured was approximately twice the size than in Ch' which means that the secondary precipitates still grew from point h to j. However, the size measurements of Cj pointed out that the average aspect ratio for *a/b* was ~1.3 and *a/c* was ~5- 6 in areas without recrystallization. This relation was not given any more for the measured precipitates in the recrystallized areas. It is unknown at this point of investigation if or how the recrystallization front changes the morphology of secondary precipitates in MHC.

It was reported that primary carbides are Hf- rich carbides where Mo replaced Hf in the lattice of the precipitates. This was recognized due to a peak shift of the HfC peaks from literature to higher 2θ angles [17,38]. Considering that primary (Hf,Mo)C have a higher volume fraction than the secondary precipitates mainly primary carbides were measured with XRD. An EDS measurement was conducted at a secondary precipitate of Cj which stood out of the matrix due to the electrolytically polishing process of the thin film foil samples. The corresponding EDS pattern revealed Hf and Mo peaks for the secondary particle. Thus it

is assumed that the secondary precipitates have similar composition than the primary carbides and that they are also mixed carbides. Final proof for this could be given by APT measurements of secondary precipitates. With Mo in the secondary carbides the theoretically calculated misfit for HfC with 4.3% would decrease further and thus it would be more favorable for secondary (Hf,Mo)C to develop $\{100\}_{Mo}//\{100\}_{ppt}$ habit planes [15,35].

XRD measurements of the SCj revealed that the Mo_2C peaks were decreased in comparison to Cf'. Additionally, there was no C in solid solution. This leads to the question what happened to the carbon of the dissolved Mo_2C when only a few isolated secondary precipitates were formed. Therefore a long term experiment SC10h1600C was conducted in order to investigate compositional effects. TEM investigations of SC10h1600C showed like for the SCj a matrix with primary Hf- rich carbides and more isolated secondary precipitates but much less than e.g. in Cj. OLM investigations revealed that the intergranular Mo_2C vanished fully which was confirmed by XRD measurements were no peaks for this carbide were visible anymore. APT investigations showed against all expectations that there was still no C in solid solution. Due to the discrepancy of missing carbon combustion analysis (CA) were conducted in order to analyze the overall C and O contents in the SC, Cj, SCj and SC10h1600C. CA analysis revealed that part of the O and C was missing which is listed in Table 6.1. There is a tendency that the overall C and O content is decreasing with increasing time of heat treatment (marked by red arrows in Table 6.1) but no proper statistic for this is available at this point of investigation. C loss was also reported by Ryan and Raffo [3-4,14-15] and according to Ryan primary Hf- rich carbides are stable at temperatures of 1600°C [48]. A possible scenario of the decarburization is that the residual oxygen in the vacuum environment of the sample chambers from the dilatometers formed C monoxide with the available C from the dissolving Mo_2C which was finally outgassing from the sample. No possible explanation regarding the oxygen loss was found at this point of examination. To understand this discrepancy more detailed investigations including a proper statistic have to be executed.

Table 6.1: Comparison of the overall C and oxygen contents of the SC, Cj, SCj and SC10h1600C.

Sample	C content in [wt.%]	Oxygen content in [wt.%]	Secondary HfC precipitates
SC	0.1068	0.0576	no
Cj	0.0862	0.0479	yes
SCj	0.0776	0.0434	no
SC10h1600C	0.0436	-	no

7 CONCLUSIONS AND OUTLOOK

The first step for the optimization of the thermo-mechanical process of the powder metallurgical alloy MHC had been taken successfully by revealing the mechanism of the formation of secondary precipitates.

To form secondary Hf- carbides strain has to be introduced prior to aging heat treatment. Experiments showed that without deformation only a few isolated secondary carbides will develop at dislocations throughout the microstructure. The precipitates form preferentially on dislocations or dislocation networks. Therefore the nucleation process of secondary precipitates is of heterogeneous nature. According to atom probe tomography investigations it is assumed that the kinetic of the formation is enhanced by the effect of pipe diffusion. Preparation of APT specimens with FIB from subgrain boundaries in the early stages of precipitation process could be the key for a successful proof of this assumption.

It was shown that most of the Hf (~0.50 at.%) was consumed by primary Hf- carbides and oxides in the as-sintered condition and that no C was in solid solution in the matrix, neither at the beginning in the as-sintered condition nor at the end of the TMP at condition j. All the other C was available as intergranular molybdenum carbide. It was pointed out by XRD and OLM investigations that the C for the precipitation reaction of secondary precipitates is delivered by molybdenum carbide which dissolved successive throughout the thermo mechanical process. Due to peak shifts of the HfC peaks in the XRD pattern combined with EDS measurements it is supposed that the secondary carbides are like the primary (Hf,Mo)C also mixed carbides [17].

The secondary precipitates have, like the primary Hf- rich carbides, a plate-like shape and they possess an orientation relationship with the matrix where <001> direction of the matrix is parallel to the <110> of the precipitate [15]. This orientation relationship was directly observable in TEM but it gets lost when the matrix recrystallizes. TEM experiments also showed that the lateral area of the plate-like carbides is incoherent and the face-on interfaces are (semi-)coherent.

CA analysis showed that the samples decarburize in the vacuum environment of the sample chambers of the dilatometers. To understand this discrepancy more detailed investigations have to be executed with and without protective environment during heat treatment.

The MHC alloy has potential for further improvement of the high temperature strength and the recrystallization behavior through modifying the amount and distribution of secondary precipitates. For this it would be necessary to have more Hf in solid solution which would be case if it is possible to modify the ratio between primary (Hf,Mo)C/Mo_2C in favor to Mo_2C in the sinter process.

In order to develop the best possible sequence for the thermo-mechanically processing of the MHC alloy, it is necessary to gather a detailed understanding of how secondary precipitates are influenced by deformation and heat treatment. Knowledge of the textural and microstructural evolution regarding recovery and recrystallization processes during hot deformation of pure molybdenum could give a lead for a uniform distribution of secondary precipitates throughout the whole microstructure. An important aspect would be to study the recrystallization and recovery processes in MHC and to identify how primary and secondary precipitates influence this behavior.

List of Figures

Figure 2.1: Development of yield strength with increasing particle radius *r* for spherical coherent particles [6]. 3
Figure 2.2: Successive stages of the Orowan mechanism of a dislocation to bypass a particle [6]. 4
Figure 2.3: Cutting process of a (semi-)coherent precipitate [6]. 5
Figure 2.4: Critical nucleus shape for nucleation on (a) a grain boundary, (b) a grain edge or (c) a grain corner [7]. 6
Figure 2.5: Effect of θ on the activation energy for grain boundary nucleation relative to homogeneous nucleation [7]**.** 7
Figure 2.6: Cahn theory of nucleation on dislocations [8-9]. 8
Figure 2.7: A section through a γ-plot for a precipitate showing one semi- or coherent interface, together with the equilibrium shape (a disk) [7]. 10
Figure 2.8: Influence of the lattice misfit on a fully coherent precipitate [7]. 11
Figure 2.9: The variation of misfit strain energy with ellipsoid shape, *f(c/a)* [7]. 12
Figure 2.10: Effect of interface type on the morphology of a growing precipitate: A, low mobility (semi-)coherent interfaces; B, high-mobility incoherent interfaces [7]. 13
Figure 2.11: (a) Edge of a plate-like precipitate. (b) Concentration profile along AA' in (a) [7]. 14
Figure 2.12: Thickening of plate-like precipitates by ledge mechanism [7]. 15
Figure 2.13: C-Curve. Percentage of transformation versus time for different transformation temperatures [7]. 16
Figure 2.14: Origin of particle coarsening. β with small radius of curvature (r_2) has a higher molar free energy than β with a large radius of curvature (r_1). The concentration of solute is therefore highest outside the smallest particles [7]. 17
Figure 2.15: Dislocations act as high conductivity path through the lattice [7]. 19
Figure 2.16: Ultimate tensile strength as a function of temperature for different wrought molybdenum alloys [3]. 20
Figure 2.17: Lattice model for the orientation relationship between a bcc molybdenum lattice (yellow) and the constrained structure of HfC (red). The C spheres are white [16]. 21
Figure 2.18: Interfacial matching of Mo bcc and precipitate fcc lattices (ZrC, ZrN, HfC & HfN) across $\{100\}_{Mo}$ // $\{100\}_{ppt}$ [15]. 23
Figure 2.19: Graphical representation of mismatch data along various nominated directions in Mo- ZrC, ZrN, HfC, HfN [15]. 23

Figure 2.20: Fcc sodium chloride structure of Hf- carbide, blue C atoms, grey Hf atoms [19]. 24
Figure 3.1: Deformation inhomogeneities in a deformed dilatometer sample. Number 1 marks the “dead” zone, number 2 the buckling area and number 3 the area with the most deformation [21]. 27
Figure 3.2: Cutting sequence (red and blue area) for OLM specimens from MHC samples. ..28
Figure 3.3: Cutting sequence for TEM thin foil preparation from deformed samples. 30
Figure 3.4: Cutting sequence for atom probe specimen preparation. 31
Figure 3.5: Electro-chemical preparation of atom probe specimens. (a) A typical two-stage electro-polishing process in order to gain atom probe tips. (b) Sharpening of a ruptured or blunt atom probe tips with a microloop [30]. 32
Figure 3.6: SEM images of electro-polished atom probe tips produced with modified stage 1 and micro loop. (a) Blunt tip with primary plate-like (Hf,Mo)C carbides and a massive pore. (b) Specimen with a (Hf,Mo)C carbide directly at the point of the tip and a hidden pore (marked with a red arrow). 32
Figure 3.7: SEM image of an atom probe specimen from the as-sintered condition (SC). Two exposed pores in short distance of each other are marked by red arrows. 33
Figure 3.8: SEM image of a well prepared sample of the sintered condition at point j (SCj)..34
Figure 4.1: Thermo-mechanically processing of MHC samples. 37
Figure 5.1: OLM micrograph of the SC. Etched with Hasson etchant [17,22]. 40
Figure 5.2: TEM micrographs of the SC. (a) Matrix with primary (Hf,Mo)C (edge-on and face-on). (b) Different spot with dislocations next to the primary Hf- rich carbides.....41
Figure 5.3: (a) Example of a 3D elemental map of Hf and C in a specimen of the SC. (b) 1D concentration plot along the z axis of the tip volume in (a). 42
Figure 5.4: TEM micrographs of the subgrain structure from Cf’ at different magnifications. (a) 15000x. (b) 25000x. 44
Figure 5.5: TEM micrographs of the subgrain structure from Cf’ at different magnifications. Subgrain in detail with a few dislocations and no secondary precipitates in it at a magnification of (a) 53000x and (b) 88000x. Possible secondary precipitates at early stages of precipitation at a magnification of (c) 88000x and (d) 140000x. 45
Figure 5.6: 3D elemental map of a specimen from Cf’. (a) Hf and C distribution. (b) Hf distribution. (c) C distribution. 46
Figure 5.7: (a) Elevation of the 3D elemental map of a specimen from Cf’ with a ROI positioned through a cluster. (b) ROI position in the top view of this specimen. (c) 1D concentration plot along the z axis of this ROI. 47
Figure 5.8: 3D elemental map of Hf and C of the four clusters of the specimen from Cf’ found by the cluster search algorithm. 48

Figure 5.9: SEM image of the subgrain structure of Cg' (back scattered electrons). 49
Figure 5.10: TEM micrographs of Cg'. (a) Subgrain structure. (b) Detail of a dislocation network with secondary precipitates in it.....50
Figure 5.11: TEM Micrographs of Cg'. Secondary precipitates on dislocations at a magnification of (a) 140000x and (b) 300000x. 51
Figure 5.12: TEM micrograph of Ch'. Partially recrystallized microstructure with secondary precipitates in recrystallized areas and in subgrain structure. 52
Figure 5.13: TEM micrographs of Ch'. (a) Area with subgrain structure with and without secondary precipitates. (b) Area with uniform distributed secondary precipitates.....53
Figure 5.14: TEM micrographs of Cj. (a) Matrix. The red circle marks the area of SAD. (b) SAD pattern of the bcc matrix.....54
Figure 5.15: TEM micrographs of Ch'. (a) Matrix in [001] zone axis with secondary edge-on precipitates. The red circle marks the spot where the selected area diffraction was recorded. (b) Diffraction pattern with reflections of the matrix and the precipitates. The arrows mark the reflections for the secondary precipitates. 55
Figure 5.16: TEM micrographs of Ch'. (a) Interface matrix (green) to edge-on precipitate (red). (b) Detail of a. There are clearly visible disturbed areas (white ellipse) in the lateral area of the plate-like precipitate. The $<110>_{Mo}$ and the $<110>_{ppt}$ include a 45°angle.....56
Figure 5.17: TEM micrographs of Ch'. (a) HRTEM image of a face-on precipitate embedded in the matrix. (b) Detail of (a). There is a smooth transition from the matrix (green dots) into the lattice of the precipitate (red dots). The face-on interface is (semi-)coherent.....57
Figure 5.18: Lattice model from Ryan for the orientation relationship between matrix and HfC carbides embedded in the matrix [15]. 57
Figure 5.19: TEM micrographs of Cj. (a) Partially recrystallized area. (b) Recrystallized area with many secondary precipitates. (c) No secondary precipitates next to primary (Hf,Mo)C. (d) Subgrain structure with almost no secondary precipitates.....58
Figure 5.20: TEM micrographs of Cj. (a) Many small precipitates preferentially at dislocations. (b) Detail of (a). Precipitates in [001] zone axis of the Mo matrix in (c) a recrystallized area and (d) in a non-recrystallized area. 59
Figure 5.21: TEM micrographs of Cj. (a) Secondary precipitate in a recrystallized area. (b) Reduced FFT form the area framed with a red square in (a). 60
Figure 5.22: EDS measurement of a secondary precipitate in Cj. (a) TEM micrograph of a secondary precipitate which stands out of the matrix. The area for the EDS measurement is marked by a black circle. (b) EDS pattern of the particle shown in (a). 61
Figure 5.23: TEM micrographs at a magnification of 43000x of (a) Ch' and (b) Cj. 62
Figure 5.24: TEM micrographs of secondary precipitates from Ch'. (a) Face-on with axis *a* and *b*. (b) Edge-on with axis *a* and *c*.....62

Figure 5.25: Particle size distribution for non- recrystallized areas of Cj. (a) Axis *a* for edge-on and face-on precipitates. (b) Axis *b* (face-on). (c) Axis *c* (edge-on). (d) Aspect ratio *a/b* (face-on). (e) Aspect ratio *a/c* (edge-on). 65
Figure 5.26: 3D elemental map of a specimen from Cg'. (a) Hf and C distribution. (b) Hf distribution. (c) C distribution. 66
Figure 5.27: 3D elemental map of the specimen from Cg' with a ROI positioned through the cluster in (a) the elevation and (b) the top view. 67
Figure 5.28: 1D concentration profile along the z axis of the ROI from Figure 5.27 of the specimen from Cg'. 68
Figure 5.29: 3D elemental map of Hf and C of the cluster in the specimen from Cg'. 68
Figure 5.30: 3D elemental map of Hf of a specimen from Cj. 69
Figure 5.31: OLM micrograph of the SC10h1600C. Intergranular Mo_2C dissolved during the long term heat treatment. Etched with Hasson etchant [17,22]. 70
Figure 5.32: TEM micrographs of the SCj. (a) The microstructure of the SCj with primary (Hf,Mo)C carbides and a few isolated secondary precipitates on dislocations. (b) Detail of (a). 71
Figure 5.33: TEM micrographs of the SC10h1600C. (a) Microstructure with a few isolated secondary precipitates. (b) Like (a) but different area. 72
Figure 5.34: 3D elemental map of Hf (blue) and C (red) of a specimen from the SCj. 73
Figure 5.35: 3D elemental map of Hf (blue) and C (red) of a specimen from the SC10h1600C. 74
Figure 5.36: XRD patterns for (a) Cf', (b) Cg', (c) Ch', (d) Cj, (e) SCj and (f) SC10h1600C. 75
Figure 5.37: OLM micrograph of Cf' with a microhardness imprint in the matrix. The sample was etched with Hasson etchant [22]. 77

List of Tables

Table 1.1: Used abbreviations.....VIII
Table 2.1: Misfit between HfC precipitate and matrix along nominated directions [15].....22
Table 2.2: Physical data of HfC [19-20].....25
Table 4.1: Labeling of samples and conducted investigation methods.....38
Table 5.1: Chemical composition of the SC in wt.% and at.%. The data was provided by Plansee SE.....39
Table 5.2: Average bulk composition of two measured atom probe tips of the SC.....43
Table 5.3: Bulk composition of the whole specimen from Figure 5.6. The elevated µ values indicate a clustering of Hf and C.....46
Table 5.4: Hf and C contents of the clusters in specimen from Cf'.....48
Table 5.5: Number of measured particles in Ch' and Cj in [001] direction of the matrix at a magnification of 43000x.....63
Table 5.6: Average sizes of axis *a*, *b* and *c* as well as aspect ratios a/b and a/c of secondary precipitates in Ch'and Cj (red values mark inaccurate measurement).....64
Table 5.7: Bulk composition of the whole specimen from Figure 5.26. The elevated µ values indicate a clustering of Hf and C.....67
Table 5.8: Hf and C content in the cluster of the specimen from Cg'.....68
Table 5.9: Average bulk composition of three APT specimens of Cj.....69
Table 5.10: Average bulk composition of four measured specimens of SCj.....73
Table 5.11: Average bulk composition of APT specimens from the SC10h1600C.....74
Table 5.12: Microhardness HV0.1 for the different conditions of the TMP. Each value represents an average value of 5 measurements.....77
Table 6.1: Comparison of the overall C and oxygen contents of the SC, Cj, SCj and SC10h1600C.....83

References

[1] W. D. Klopp, P. L. Raffo, and W. R. Witzke, “Strengthening of molybdenum and tungsten alloys with HfC”, *Journal of Metals*, pp. 27-38, 1971.

[2] W. R. Witzke, “Compositional effects on mechanical properties of HFC-strengthened molybdenum alloys”, *Metallurgical Transactions A*, vol. 7, no. 3, pp. 443-451, 1976.

[3] P. L. Raffo, “Thermomechanical processing of molybdenum- hafnium- carbon alloys- unpublished report from the Lewis research center”, 1970.

[4] P. L. Raffo, “Exploratory study of mechanical properties and heat treatment of molybdenum- hafnium- carbon alloys- unpublished report from the Lewis research center”, 1969.

[5] Plansee SE, “MHC (Molybdän-Hafnium-Kohlenstoff)”, http://www.plansee.com/de/Werkstoffe-Molybdaen-402.htm, September 2012.

[6] G. Gottstein, “*Physikalische Grundlagen der Metallkunde*”, 3rd ed, Aachen: Springer-Verlag Berlin Heidelberg, p. 502, 2007.

[7] D. Porter, K. Easterling, and M. Sherif, “*Phase transformations in metals and alloys*”, 3rd ed., Boca Raton: CRC Press Taylor & Francis Group, 2009.

[8] J. W. Martin, R. D. Doherty, and B. Cantor, “*Stability of microstructure in metallic systems*”, 2nd ed., Cambridge: Cambridge University Press, 1997.

[9] J. W. Cahn, “Nucleation on Dislocations”, *ACTA METALLURGICA*, vol. 5, no. 3, pp. 169-172, 1957.

[10] J.-H. Choy and J. K. Lee, “On the shape evolution of a two-dimensional coherent precipitate with a general misfit strain”, *Materials Science and Engineering: A*, vol. 285, no. 1–2, pp. 195-206, 2000.

[11] X. Li, K. Thornton, Q. Nie, P. W. Voorhees, and J. S. Lowengrub, “Two- and three-dimensional equilibrium morphology of a misfitting particle and the Gibbs–Thomson effect”, *Acta Materialia*, vol. 52, no. 20, pp. 5829-5843, 2004.

[12] T. Heumann and H. Mehrer, “*Diffusion in Metallen*“, Münster: Springer-Verlag Berlin Heidelberg, 1992.

[13] I. Malashenko, Y. A. Kashtalyan, N. Vashchilo, V. Y. Naumenko, and A. Vasil’ev, “Hardening of molybdenum by microadditions of hafnium and HfC carbide”, *Strength of Materials*, vol. 6, no. 7, pp. 850–855, 1974.

[14] N. Ryan and J. Martin, “Hardening of some molybdenum-based alloys by precipitation of nitride and carbide phases”, in *6th Plansee Seminar*, pp. 182-207, 1968.

[15] N. E. Ryan, W. A. Soffa, and R. C. Crawford, “Orientation and habit plane relationships for carbide and nitride precipitates in molybdenum”, *Materials Characterization*, vol. 39, no. 2–5, pp. 95-90, 1997.

[16] C. Hin, Y. Bréchet, P. Maugis, and F. Soisson, “Kinetics of heterogeneous dislocation precipitation of NbC in alpha-iron”, *Acta Materialia*, vol. 56, pp. 5535-5543, 2008.

[17] C. Pöhl, J. Schatte, and H. Leitner, “The metallographic characterization of the molybdenum based alloy MHC by a color etching technique”, *Materials Characterization - to be published*.

[18] “AMERICAN Elements”, http://www.americanelements.com/hf.html, September 2012.

[19] J. M. Zuo and J. C. Mabon, “Web-based electron microscopy application software: Web-EMAPS, Microsc Microanal 10(Suppl 2)”, http://emaps.mrl.uiuc.edu/, 2004.

[20] SpringerMaterials, “The Landolt-Börnstein database”, http://www.springermaterials.com, 2012.

[21] E. Doege and B.-A. Behrens, “*Handbuch Umformtechnik: Grundlagen, Technologien, Maschinen*”, Hannover: Springer-Verlag Berlin Heidelberg, 2010.

[22] G. Petzow, “*Metallographisches, keramographisches und plastographisches Ätzen*”, 6th ed., Stuttgard: Gebrüder Borntraeger, 1994.

[23] S. Primig, H. Leitner, A. Lorich, W. Knabl, H. Clemens, and R. Stickler, “SEM and TEM investigations of recovery and recrystallization in technically pure molybdenum”, in *Reports of the 13th international metallographic conference in Leoben*, pp. 289-294, 2010.

[24] H. A. Calderon and G. Kostorz, “Microstructure and plasticity of two molybdenum-base alloys (TZM)”, *Materials Science and Engineering: A*, vol. 160, pp. 189-199, 1993.

[25] F. Vurpillot, a Cerezo, D. Blavette, and D. J. Larson, “Modeling image distortions in 3DAP.”, *Microscopy and microanalysis : the official journal of Microscopy Society of America, Microbeam Analysis Society, Microscopical Society of Canada*, vol. 10, no. 3, pp. 384-90, 2004.

[26] M. K. Miller and R. G. Forbes, “Atom probe tomography”, *Materials Characterization*, vol. 60, no. 6, pp. 461-469, 2009.

[27] F. Danoix, G. Grancher, A. Bostel, and D. Blavette, “Standard deviations of composition measurements in atom probe analyses-part II: 3D atom probe”, *Ultramicroscopy*, vol. 107, no. 9, pp. 739-43, 2007.

[28] F. Danoix, G. Grancher, A. Bostel, and D. Blavette, “Standard deviations of compostion measurements in atom probe analyses. Part1 conventional 1D atom probe”, *Ultramicroscopy*, vol. 107, no. 9, pp. 734-738, 2007.

[29] M. Miller, “Three-dimensional atom probes”, *Journal of Microscopy*, vol. 186, no. November 1996, pp. 1-16, 1997.

[30] M. K. Miller, A. Cerezo, M. G. Hetherington, and G. D. W. Smith, “*Atom probe field ion microscopy*”, 2nd ed., New York: Oxford University Press Inc., 2006.

[31] K. Thompson, D. Lawrence, D. J. Larson, J. D. Olson, T. F. Kelly, and B. Gorman, “In situ site-specific specimen preparation for atom probe tomography”, *Ultramicroscopy*, vol. 107, no. 2–3, pp. 131-9, 2007.

[32] “IVASTM 3.6.0 user guide.” Cameca Instruments Inc., 2011.

[33] M. P. Moody, L. T. Stephenson, A. V. Ceguerra, and S. P. Ringer, “Quantitative binomial distribution analyses of nanoscale like-solute atom clustering and segregation in atom probe tomography data”, *Microscopy research and technique*, vol. 71, no. 7, pp. 542-50, 2008.

[34] D. Vaumousse, a Cerezo, and P. J. Warren, “A procedure for quantification of precipitate microstructures from three-dimensional atom probe data”, *Ultramicroscopy*, vol. 95, no. 1–4, pp. 215-21, 2003.

[35] *Powder Diffraction File 00-039-1491 for HfC, International Center for Diffraction Data, PDF-2/release 2007*.

[36] *Powder Diffraction File 00-042-1120 for Mo, International Center for Diffraction Data, PDF-2/release 2007*.

[37] *Powder Diffraction File 00-034-0104 for HfO2, International Center for Diffraction Data, PDF-2/release 2007*.

[38] *Powder Diffraction File 00-035-0787 for Mo2C, International Center for Diffraction Data, PDF-2/release 2007*.

[39] D. B. Williams and B. C. Carter, “*Transmission electron microscopy*”, 1st ed., New York: Springer Science+Buisness Media, 2009.

[40] C. Pöhl, J. Schatte, and H. Leitner, “Solid solution hardening of molybdenum-hafnium alloys: experiments and modeling”, *Materials Science and Engineering: A*, vol. 559, pp. 643-650, 2012.

[41] Z. G. Yang and M. Enomoto, “Discrete lattice plane analysis of Baker-Nutting related B1 compound/ferrite interfacial energy”, *Materials Science and Engineering: A2*, vol. 332, no. 1, pp. 184-192, 2002.

[42] S. Primig, H. Leitner, W. Knabl, A. Lorich, H. Clemens, and R. Stickler, “Textural evolution during dynamic recovery and static recrystallization of molybdenum”, *Metallurgical and Materials Transactions A*, 2012.

[43] F. Perrard, P. Donnadieu, a. Deschamps, and P. Barges, “TEM study of NbC heterogeneous precipitation in ferrite”, *Philosophical Magazine*, vol. 86, no. 27, pp. 4271-4284, 2006.

[44] B. Dutta and C. M. Sellars, “Effect of composition and process variables on Nb(C, N) precipitation in niobium microalloyed austenite”, *Materials Science and Technology*, vol. 3, pp. 197-206, 1987.

[45] B. Dutta, E. Valdes, and C. M. Sellars, “Mechanism and kinetics of strain induced precipitation of Nb(C, N) in austenite”, *Acta Metallurgica et Materialia*, vol. 40, no. 4, pp. 653-662, 1992.

[46] W. M. Rainforth et al., “Precipitation of NbC in a model austenitic steel”, *Acta Materialia*, vol. 50, pp. 735-747, 2002.

[47] E. V. Pereloma, B. R. Crawford, and P. D. Hodgson, “Strain-induced precipitation behaviour in hot rolled strip steel”, *Materials Science and Engineering: A*, vol. 299, no. 1–2, pp. 27-37, 2001.

[48] N. E. Ryan and J. W. Martin, “The formation and stability of group IVa carbides and nitrides in molybdenum”, *Journal of the Less Common Metals*, vol. 17, no. 4, pp. 363-376, 1969.